Cape Peninsula
University of Technology

Characterisation of mechanical properties of friction stir processed AA5083/AA6082 dissimilar joints reinforced with coal

by

KEEGAN JOHN ZASS

Thesis submitted in fulfilment of the requirements for the degree

Master of Engineering: Mechanical Engineering

in the Faculty of Engineering and the Built Environment at the Cape Peninsula University of Technology

Supervisor: Dr Velaphi Msomi

Co-supervisor: Dr Sipokazi Mabuwa

Bellville

August 2023

DECLARATION

I, Keegan Zass declare that the contents of this thesis represent my own unaided work and that the thesis has not previously been submitted for academic examination towards any qualification. Furthermore, it represents my own opinions and not necessarily those of the Cape Peninsula University of Technology.

09 October 2023

Signed   Date

ABSTRACT

The aerospace, automotive, and transportation industries have increasingly recognised the importance of lightweight planes and automobiles. The greater the mass of vehicles, the more power they require for motion and acceleration. Reducing their mass not only lowers fuel consumption but also curtails carbon emissions. Consequently, the adoption of lightweight materials like aluminium alloys has become paramount. Yet while aluminium exhibits certain excellent qualities, it falls short in applications where lightweight materials with great strength are required. To address this limitation, modifying the mechanical properties of aluminium, particularly its surface microstructure, can enhance its performance. One effective approach is to reinforce aluminium with particles, resulting in surface composites. The properties of these composites are influenced by various factors, including the method used to alter their mechanical properties.

Friction stir processing (FSP) is among the methods used to produce surface composites. FSP aims to modify the local microstructure of workpieces as opposed to welding them together. While reports on the friction stir processing of particle-reinforced composites abound in the literature, the use of coal as a reinforced composite remains unexplored. This study focused on characterising the influence of friction stir processing on dissimilar joints (AA5083/AA6082) when reinforced with coal powder. The dissimilar plates were first joined using the friction stir welding (FSW) technique. Subsequently, the friction stir welded (FSWed) joints were subjected to FSP with and without the addition of reinforcing coal. The impact of employing coal reinforcement on the dissimilar joints was assessed through various tests, including microstructural analysis, tensile tests, bending tests, micro-hardness and fractographic analysis. The following comparative analysis of the results was observed.

The test results of the microstructural analysis showed that the mean grain size obtained from friction stir welding (FSW) was measured at 19.7 μm. When friction stir processing (FSP) was employed, the average grain size for joints decreased dramatically to 9.63 μm. The FSP reinforced with Coal technique (FSP+Coal), which involved partial reinforcement with coal powder, achieved a remarkable grain refinement of 8.75 μm, surpassing the conventional FSP method. The results clearly indicate that FSP+Coal outperformed both FSW and conventional FSP joints in terms of grain refinement. Additionally, the microstructural analysis revealed that an increasing number of passes led to smaller grain sizes in the processed zone, resulting in a more uniform distribution of grains.

In flexural tests of face specimens, FSW face specimens failed at a maximum strain of 12.7% and a flexural stress of 535 MPa. In comparison, FSP face specimens displayed a lower maximum strain of 10.81% but higher flexural stress of 545.6 MPa. Conversely, the FSP+Coal face specimens produced a substantially lower performance, failing at a maximum strain of only 3% and a flexural stress of 222 MPa. These results indicate that the inclusion of coal in

the FSP process significantly affected the mechanical properties of the specimens, leading to lower maximum strain and flexural stress values than the standard FSW and FSP specimens. Some of the processed joints in the FSP+Coal group showed deflection and cracks, particularly in the AA6082 TMAZ (thermo-mechanically affected zone) side regions, while others remained free from cracks there but exhibited cracks at the AA5083 weld end TMAZ.

The tensile properties of the joints were then evaluated for FSW, FSP, and FSP+Coal. For FSWed joints, the maximum ultimate tensile strength (UTS) achieved was 145.9 MPa at a tensile strain rate of 9.43%, with the minimum UTS recorded at 93.43 MPa at a tensile strain rate of 7.02%. In the FSPed joints, the maximum UTS obtained was 170.9 MPa at a tensile strain rate of 9.13%, and the minimum UTS reached 126 MPa at a tensile strain rate of 7.38%. For the FSP+Coal joints, the maximum UTS was 142 MPa at a tensile strain rate of 9.28%, while the minimum UTS was 104.06 MPa at a tensile rate of 4.63%. It is evident that the introduction of coal particle reinforcement resulted in a reduction in UTS compared to FSWed and FSPed joints, indicating a trade-off between the presence of coal particles and tensile properties. Yet despite the reduction in UTS, the FSP+Coal method had positive effects on the properties of the AA6082-T651 material. Both FSWed and FSPed samples experienced fracture at the AA5083-H111 side, signifying different failure characteristics for the welding methods used.

Regarding average hardness, the FSP+Coal joints exhibited a hardness of 70.74 HV at the nugget zone. In comparison, FSP resulted in a hardness of 67.72 HV at the nugget zone, and FSW displayed a hardness of 64.64 HV at the nugget zone. The regions near the tool pin and tool shoulder positions on the AA6082-T651 side exhibited slightly lower hardness values than other positions. However, the nugget zone demonstrated a significant increase in hardness values along the entire length of the welded joint, surpassing the hardness of the AA6082-T651 HAZ (heat -affected zone) side.

It is important to consider that the AA6082 alloy is a precipitate-hardened alloy, and temperatures exceeding 200°C can significantly affect its particles, particularly on the HAZ side, compared to the AA6082-T651 base material. The data obtained from this research clearly demonstrates that reinforcement with coal powder particles in friction stir processing has a significant impact on the mechanical properties of the joints. This study has embraced the spirit of scientific exploration and innovation in advancing the understanding of dissimilar aluminium alloy joints. It paves the way for future developments in the field, including the promotion of a more sustainable and efficient approach to materials joining. Moreover, the findings have potential applications in the motor industry, including crumple zone and brake disc design.

LIST OF PAPERS

The thesis includes the following supplements:

Supplement 1

Zass, K.; Mabuwa, S.; Msomi, V. A review on reinforced particles used on the production of FSP composites, Materials Today: Proceedings, 56, (Part 4), 2022, Pages 2392-2397.

ACKNOWLEDGEMENTS

DEDICATION

To my parents John Zass and Ingrid Zass, who always wanted to see their children furthering their studies from a young age. This is for you, every time I looked at mom and dad, I knew I had to do this, not only for myself but for the family name.

Contents

Contents

LIST OF FIGURES

LIST OF TABLES

GLOSARY

Terms/Acronyms/Abbreviations	Definition/Explanation
CPUT	Cape Peninsula University of Technology
FSW	Friction Stir Welding
FSP	Friction Stir Processing
TWI	The Welding Institute
ASTM	American Society for Testing and Materials
TMAZ	Thermo-Mechanically Affected Zone
NZ	Nugget Zone
Cu	Copper
Al	Aluminium
Zn	Zinc
Mg	Magnesium
Si	Silicon
Li	Lithium
HAZ	The Heat Affected Zone
BM	Base Material
WM	Weld Metal
SEM	Scanning Electron Microscope
UTS	Ultimate Tensile Strength
UFS	Ultimate Flexural Strength
MFS	Maximum Flexural Strain

NOTATIONS

English Symbol

C   Celsius

Greek Symbols

°   Degree

μm   Micrometer

β   Mg-Si Precipitates

θ   Theta

Units

g   Gram

kN   Kilo Newton

ml   Millilitre

mm   Millimetre

min   Minute

MPa   Mega Pascal

RPM   Revolutions Per Minute

s   Seconds

V   Volt

A   Amps

cm³   Centimetre cubed

CHAPTER ONE

INTRODUCTION

1.1 Introduction to the study

Aluminium, a lightweight metal with a silvery-white appearance, possesses remarkable qualities that have established it as one of the primary engineering materials in modern times. Its versatility allows it to be seamlessly combined with various alloys, making it indispensable both in everyday life and industry. Among its distinguishing characteristics are its non-corrosive, non-magnetic, and non-sparking properties, alongside high heat and electrical conductivity, low density, and excellent fabricability [1].

Aluminium alloys can be broadly classified into two categories: cast compositions and wrought compositions. In the case of cast compositions, the alloy group number is denoted by the first digit in a four-digit numerical designation, which is given to foundry ingots and casting forms. These designations are presented in Table 1.1.1. Conversely, wrought aluminium alloys are labelled using a four-digit number system, where the first digit indicates the major alloying element(s), as shown in Table 1.1.2 [2].

Table 1.1.1: Cast aluminium alloy designation system.

Principal Alloy Element	Series
99.% minimum Aluminium	1xx.x
Copper	2xx.x
Silicon + Copper and/or Magnesium	3xx.x
Silicon	4xx.x
Magnesium	5xx.x
Unused Series	6xx.x
Zinc	7xx.x
Tin	8xx.x
Other Elements	9xx.x

Table 1.1.2: Wrought aluminium alloy designation system.

Principal Alloy Element	Series
99.% Minimum Aluminium	1xxx
Copper	2xxx
Manganese	3xxx
Silicon	4xxx
Magnesium	5xxx
Magnesium and Silicon	6xxx
Zinc	7xxx
Other Elements	8xxx

There are two types of wrought aluminium alloys, heat-treatable and non-heat-treatable. The wrought aluminium alloys in the 7xxx series, 6xxx series and 2xxx series undergo age-hardening to improve their levels of strength. This is possible because the alloys are heat treatable. The preliminary strength of the alloys is attained through the hardening effect of alloying components: magnesium (Mg), zinc (Zn), copper (Cu) and silicon (Si). The non-heat-treatable wrought aluminium alloys contain the 5xxx, 4xxx and 3xxx series, as well as the commercially pure aluminium 1xxx series. These alloys cannot be strengthened by precipitation hardening but are susceptible to hardening by cold working [3].

One of the aluminium alloys used in this study was the AA5083-H321 5xxx series, which comprises strain-hardened alloys with Mg as the key alloying element. The alloy had an ultimate tensile strength of 350 MPa. The AA5083 series has been developed for the manufacture of parts of petrol-driven vehicles, military vehicles, bridges, buildings, cryogenic pressure vessels, hulls of small boats, and superstructures in ships. The 5xxx series of alloys more generally have weldability, corrosion resistance and good toughness [4]. The second alloy that was used was the AA6082-T6. This alloy is frequently used for welding in manufacturing because of its good erosion resistance and average strength. The 6xxxx series, in which the major alloying elements are Si and Mg, is regarded as the structural alloy with the greatest strength. It is utilised in extruded forms, for example, as sheets in aircraft and automotive construction. It is also utilised in cranes, trusses, transport, bridges and other applications. The 6xxx alloys have superior machinability in the T651 and T6 temper [5]. The ultimate tensile strength of this series ranges between 245 MPa and 330 MPa. This corresponds to strain-hardenable, average-strength alloys with good weldability, heat treatability and superior resistance to stress corrosion cracking [4].

A combination of dissimilar alloys, specifically AA6082 and AA5083, was utilised. The combination was joined using the technique known as friction stir welding (FSW). FSW is most suitable for this job because traditional fusion welding methods are challenging when it comes

to joining metallic alloys to a high-strength aluminium alloy [9]. The FSW joint produced was then friction-stir processed with the addition of coal reinforcement to modify the stir zone properties.

1.1.1 Friction stir welding

Originally introduced in 1991 by The Welding Institute (TWI), friction stir welding (FSW) has been widely utilised in the welding of aluminium alloys [6]. It is a green technology that produces excellent evolving properties and generates no toxic fumes or smoke during or after the welding process. Friction stir welding has been recognised as a technique for ushering external reinforcement particles into the stir zone of bulk alloys [7].

Figure 1.1.1 below depicts the process of FSW, with Figure 1.1.1(a) showing the tool and the workpieces. Figure 1.1.1(b) shows the pin making contact with the workpieces, while a force presses downwards onto the workpieces, causing frictional heat to increase. In Figure 1.1.1(c), the shoulder also contacts the workpieces, causing friction to increase to a point at which the materials become plastically deformed. As shown in Figure 1.1.1(d), the tool traverses the plate mashing the two workpieces together [8]. Once the tool reaches the end of the workpiece, it is then released back to a stationary position marking the end of the process. The joint produced by the joining of the two materials is referred to as the welded zone. This zone comprises various microstructural zones, for example, the thermomechanical-affected zone (TMAZ), the nugget zone (NZ) and the heat-affected zone (HAZ). The microstructural arrangement of the stir zone determines the strength and ductility of the joint formed, while a fine and homogenous grain size confers better mechanical properties [9].
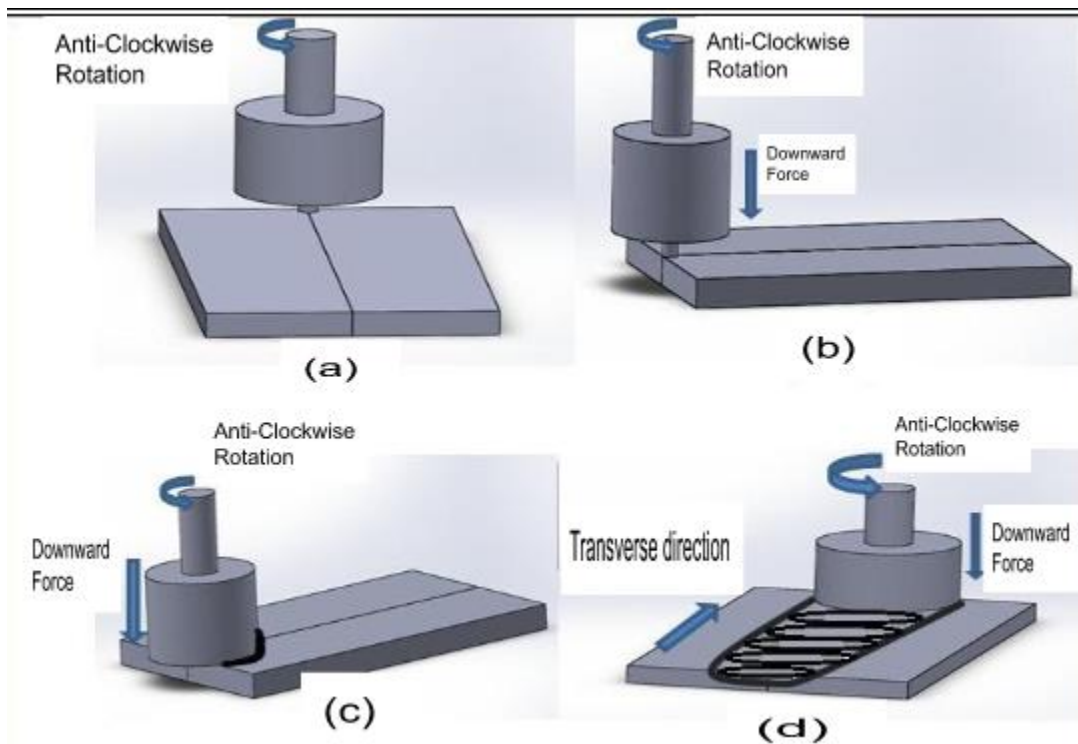
Figure 1.1.1: The process steps for friction stir welding.

1.1.2 Friction stir processing

Friction stir processing (FSP) is based on FSW technology. FSP and FSW contain a matching process principle. Figure 1.1.2 features a SolidWorks diagram of the FSP process. In friction stir processing, a rotating pin is inserted into workpiece material with a downward plunging force, pushing the pin into the welded joint of the workpiece at an appropriate tool tilt angle and then travelling along the welded line. The rotating tool will cause friction and heat build-up in the material around the pin, rising to a temperature below its melting point. The rotating tool "stirs" the material together and results in a mixture of the two materials. As the tool pin moves forward, molten plastic-like materials are formed around the pin. The material then flows to the rear of the pin, where it is extruded, forged, fused and cooled behind the tool under hydrostatic pressure conditions [10]. The most influential process parameters of FSP are the tool traverse speed, rotation speed, multi-pass and tool tilt angle. The magnitude of the tool also influences the material structure. The heat generated from a low traverse speed and high rotational speed constitutes the most important parameter [11-12]. When using FSP to fabricate composites, raising the rotational speed and/or lowering the travelling speed can create a higher temperature and cause more plastic deformation [13].

In reinforced particles, the parameter is beneficial to the mixture and the matrix structure of the workpiece. In the FSP processes, non-consumable tools are utilised,

4

comprising pin-less tools and tools with pins. Pin-less tools are used for surface modifications of the material whereas the tools with pins are used for both FSW and FSP applications [14].
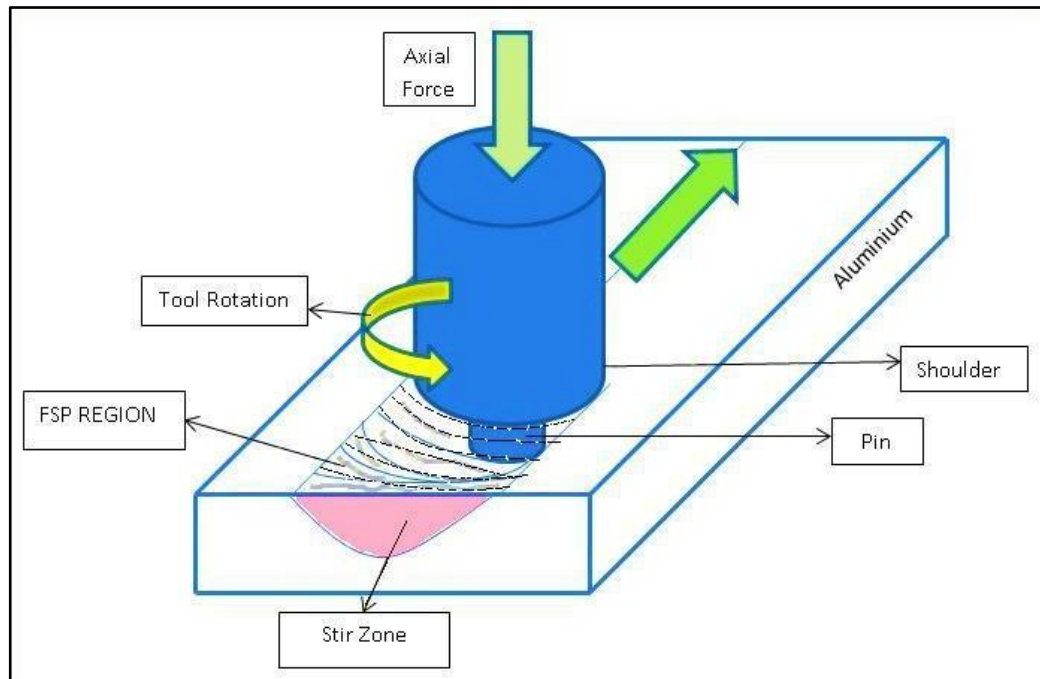
Figure 1.1.2: SolidWorks diagram of FSP setup and rotating tool.

1.1.3 FSP matrix composites

Aluminium Metal Matrix Composites (AMMCs) are composites characterised by the incorporation of reinforcement particles, either non-metallic or metallic, into the metal matrix [15,16]. The mechanical properties of AMMCs are influenced by several parameters, including the volume and size of the reinforcement particles and the characteristics of the matrix reinforcement. To manufacture particle-reinforced metal matrix composites, two main methods have been utilised: molten metal processing and powder metallurgy. However, to achieve a uniform distribution of fine reinforcement particles within the composite using conventional methods has proved challenging [17].

Researchers have explored the application of friction stir processing in the fabrication of aluminium matrix composites. FSP offers several advantages for producing AMMCs, such as using high temperatures to aid in-situ improvement of reinforcing particles and inducing plastic deformation to enhance the refinement and mixing of the particles within the material [18].

Various techniques have been attempted by researchers to incorporate reinforcement particles into the aluminium metal matrix during FSP. For instance, Mishra et al. [19] experimented with adding a small amount of methanol to silicon carbide powders. The powder-

methanol mixture was then applied to the surface of the base metal, resulting in a thin surface composite during FSP. Another method involves pre-fabricating channels on the surface of the workpieces and subsequently filling them with the reinforced particles.

Figure 1.1.3 illustrates the incorporation of reinforcement particles using the hole drilling method, which works in a similar way to the groove method. Grooves/holes are covered with a pin-less tool during FSP to prevent the particles from splattering. Then, a tool with a pin is used in a multi-pass or single FSP process, along with a prefabricated groove, ensuring even circulation of the reinforcement particles within the stir zone [20-22]. Additionally, surface composites with a uniform distribution of strengthening particles have been achieved by adding the reinforced particles after boring blind holes into the workpiece surface [22-24]. These innovative techniques facilitate better control over the dispersion of reinforcement particles in AMMCs during the FSP process, leading to improvement in the mechanical properties and overall performance of the composites.
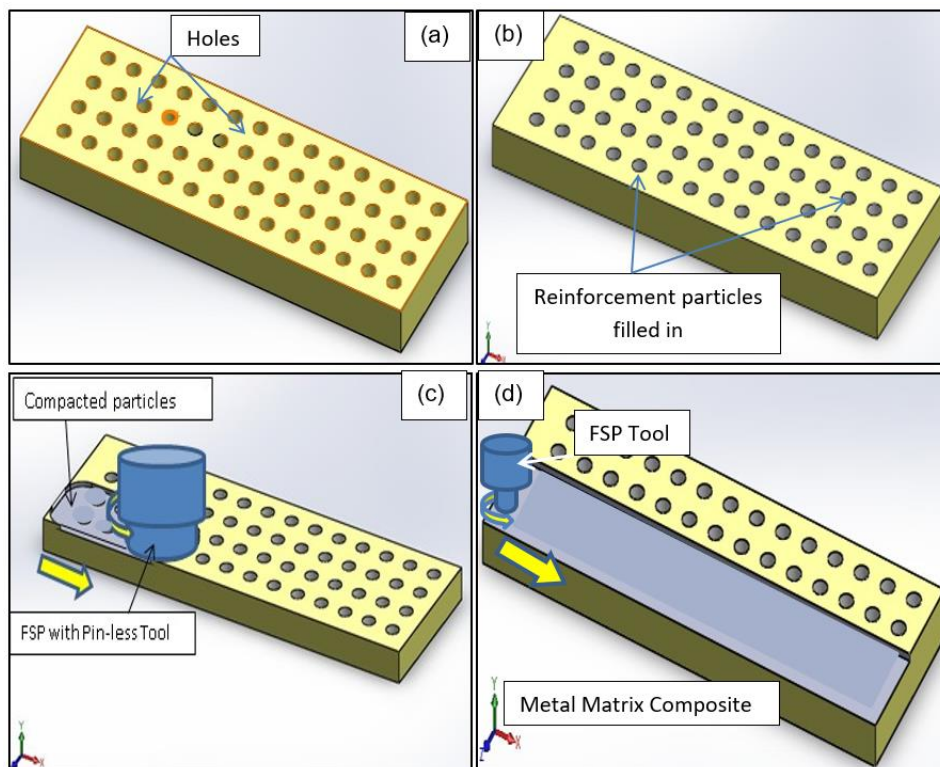
Figure 1.1.3: FSP composite: (a) Holes drilled, (b) Reinforcement filled in (c) FSP with Pin-less tool to compact and seal the particles within the holes; and (d) Friction stir processing.

1.2 Problem statement

The use of dissimilar aluminium alloy joints is a common practice in various engineering applications, where lightweight and corrosion-resistant materials are essential. However, achieving optimal mechanical properties in these joints remains a significant challenge due to the inherent differences in alloy compositions. Friction stir processing (FSP) has emerged as a promising technique to improve the mechanical properties of such joints. While prior research has explored the use of various reinforcement particles to enhance the properties of FSP-processed joints, there exists a significant knowledge gap regarding the utilization of coal particles as a novel reinforcement material in this context. Coal is an abundant and cost-effective resource, but its potential as a reinforcement agent for dissimilar aluminium alloy joints processed through FSP has not been thoroughly investigated. This study aims to address this critical knowledge gap by investigating and characterising the mechanical properties of friction stir processing AA5083/AA6082 with reinforced coal particles on dissimilar aluminium joints. The research will explore the feasibility of using coal as a reinforcement material, potentially providing an innovative and sustainable solution for enhancing the performance of dissimilar alloy joints in various engineering applications.

The novelty of this research lies in its unconventional approach to enhancing the mechanical properties of dissimilar aluminium alloy joints. While previous studies have primarily focused on conventional reinforcement materials such as ceramics or metallic particles, the utilization of coal particles introduces a unique perspective to the field of FSP. Investigating coal as a reinforcement material holds the potential to not only improve the mechanical properties of joints but also reduce the environmental impact by utilizing an abundant and low-cost resource. Moreover, the complex interactions between coal particles and aluminium alloys during FSP are relatively unexplored, making this research an exciting opportunity to expand the understanding of the process. Ultimately, the findings from this work may pave the way for innovative and sustainable solutions in the field of dissimilar aluminium alloy joining, with broad implications for industries requiring high-performance lightweight materials.

1.3 Research Background

In the automotive, aerospace and transportation industries, a central goal is to create lightweight machines. Lightweight metals like aluminium have become the transportation industry's most valuable material. In the manufacturing industry more generally, cast and steel forms remain components to be used for their strength, but in recent times the use of lightweight materials has become more widespread. FSW and FSP produce a better quality of joining process by promoting meshing by the material itself instead of using bolts, adhesives and rivets. Friction stir welding has developed into a new process that is replacing other fusion

welding techniques and mechanical fasteners. For joining aluminium alloys with other alloys FSW and FSP have become the most effective processes [25]. The mechanical properties of a workpiece or joint stand to benefit from FSP because of its techniques. The process is also a low energy utilisation method of introducing reinforcing particles into the metal matrix and forming bulk composites.

Abbasi et al. [26] studied aircraft material to determine the mechanical properties of corrosion resistance of an AZ31B/SiC welded joint. The results indicated that joints produced by FSP with SiC particles revealed better corrosion resistance and mechanical properties than joints without particles. Mehdi and Mishra [27] researched the FSP and TIG welding together of dissimilar AA6061 and AA7075 with reinforcement filler wire ER4043 and ER5356. Friction stir processing significantly modified the mechanical properties, with TIG + FSP developing fine grains of 3.5 μm. When the tool rotational speed was increased the grains got finer. The results also showed improvement of the weld joints of AA7075/ER4043 and AA7075/ER5356 as a result of the addition of filler wire.

Rana et al. [28] investigated the surface composite joint of AA7075 with B4C reinforcement. Various transverse speed and tool rotational speeds were compared. The best weld, with fine-grain microstructure and high wear resistance, was produced by a tool rotational speed of 545 rpm. The hardness of the AA7075/B4C workpiece using FSP was 1.3–1.6 times greater than the base workpiece. Kurt et al. [29] researched FSP joints of AA1050 with reinforcement particles of SiC to examine the mechanical properties. They found that the microhardness of the FSP SiC increased significantly with increasing tool rotational speed compared to the plain workpiece joint. The SiC particles were three times the hardness of the plain base workpiece, and bending strength was also enhanced.

Sharma et al. [30] conducted research on FSP in respect of AA6061, integrating SiC-Graphite particles for reinforcement. Various parameters were essayed, but a 25 mm/min transverse speed and a tool rotational speed of 2200 rpm got the best results. The tests showed that the strength of the reinforced weld was considerably greater than the normal FSP weld. Microstructural analysis confirmed a uniform distribution of the particles. It was concluded that the stirring speed performed a critical role in the resultant mechanical properties of the weld.

Palanivel et al. [31] investigated a way to successfully synthesize AA6082 / TiB2 + BN hybrid composite and compared it to AA6082 / BN and AA6082TiB2. The reinforcement particle powder was placed in a groove and then FSP was conducted. The results revealed that the TiB2 particles remained fragmented and that the BN particles were not destroyed in the welded workpiece. Successful interfacial binding between the aluminium matrix and the particles was confirmed, with massive grain refinement in the matrix. A robust weld was therefore formed by boron nitride particle powder via the FSP method, with reduced fragmentation and enhanced wear resistance.

Selvakumer et al. [32] focused their research on the use of molybdenum MO as a potential reinforcement medium to improve the ductility of AA6082 by FSP. The workpiece achieved a homogenous distribution of 18 vol % of MO, the particles being successfully retained in the aluminium matrix without any interfacial reaction. The testing showed that the fracture surface was characterised by deeply cultivated dimples, authenticating appreciable ductility and improved tensile strength. Additionally, a study was conducted on an AA6082 FSP joint reinforced with stainless steel, using 18 vol%. Dimpling developed on the fracture surface of the composites, confirming ductility. The workpiece showed equiaxed grains throughout the stir zone where the stainless-steel reinforcement particles were located. In comparison with the base metal, the workpiece tensile strength was enhanced without sacrificing ductility [33].

Da Silva et al. [34] investigated MIG butt weld joints of AA6082-T6 to establish the benefit of FSP welds. The focus was on enhancing fatigue behaviour. Four welds were observed: FS post-processed welds without and with and MIG welds without and with reinforcement. The results of this showed that friction stir processing only enhanced ductility and fatigue resistance. There was no change in mechanical strength and hardness compared to the MIG weld.

There are many reports on particle reinforced composite use in FSW and FSP, but nothing published on using coal as a reinforcing composite. A study in which coal fly ash (CFA) was used for reinforcement found that it produced a composite with excellent tensile strength, higher than the processed base metal (AA7075-T651-p). The research also showed that fly ash has good mechanical properties [16].

1.4 Research Objectives

This study aims to characterise the mechanical properties of friction stir processed AA5083/AA6082 dissimilar joints reinforced with coal. This aim will be achieved through the following objectives:

- Characterise coal powder as a bioprocessing agent and an alternative reinforcement material
- Optimise processing parameters (tool rotation, traverse speed)
- Join the dissimilar materials via FSW
- The FSWed joints will then be FSPed using the optimised processing parameters
- Different specimens for the tests to be performed will be extracted from the produced FSPed plates
- The FSPed joints without reinforced coal will be studied comparatively with the FSPed joints reinforced with coal. The test to be conducted will involve tensile tests, bending tests, microhardness tests and microstructural analysis.

1.5 Thesis outline

In this study, the characterisation of the mechanical properties of friction stir processed AA5083/AA6082 dissimilar joints reinforced with coal will be performed in five chapters, as summarised below.

Chapter One serves as the foundation of the study, introducing FSP and formulating the problem statement. The background of the research is described in such a way as to highlight the significance and relevance of the chosen topic. The research aim and objectives are stated to provide a clear roadmap of the study's direction. The chapter the closes with an outline of the dissertation.

Chapter Two offers an extensive account of the literature relevant to the study, focusing on FSW, FSP in respect of the aluminium grades concerned and previous experiments with reinforcement particles. The synthesis of existing knowledge contributes to a deeper understanding of the subject matter and provides valuable background for the experimental work that follows.

Chapter Three details the experimental setup employed in the study. It presents a comprehensive overview of the equipment and methodologies utilised to perform the study. The tests performed and ASTM standards are also detailed. The performances of various experimental parameters are systematically examined.

Chapter Four sets out the results obtained from the experimental investigations. These results are critically analysed and discussed in light of the research objectives and reviewed literature. The significance of the findings is highlighted, and any observed trends or variances are thoroughly explained.

In Chapter Five, a comprehensive conclusion is provided. The implications of the results are discussed in the context of the overall research objectives, shedding light on their practical significance. Recommendations are made for future studies regarding the use of coal as a reinforcement particle for both FSW and FSP joints.

CHAPTER TWO

LITERATURE REVIEW

2.1 Introduction

This chapter offers a comprehensive literature review of material relevant to the research. The main focus is the friction stir welding of AA6082 and AA5083 and the friction stir processing of AA6082/AA5083, although light will be shed on cognate issues such as welding parameters more generally.

2.2 Friction stir welding of AA6082

Friction stir welding (FSW) is controlled by a specific set of process parameters for each weld run. These parameters play a crucial role in determining the joint's reliability and the quality of post-weld features that cannot be undone once the welding is completed. For this reason, it is essential to carefully establish these parameters beforehand. This section will discuss the tilt angle, rotational speed, traversing speed, and dwell time as the key parameters.

One of the aluminium workpieces commonly used in welding fabrication is AA6082, which possesses good erosion resistance and is an average-strength aluminium alloy. Among the 6xxxx series of aluminium alloys, the 6xxx series is known for its superior strength due to the presence in its structural composition of silicon and magnesium. Thanks to its excellent machinability in the T651 and T6 temper, AA6082 is utilised in various forms, including extruded shapes and sheets, in applications such as automobiles, aircraft, cranes, trusses, transport, and bridges. This series of alloys is strain hardenable with good weldability, heat treatability, and resistance to stress corrosion cracking [4, 5].

Ramesh et al. [35] conducted research on AA6082, focusing on the influence of tool parameters and geometries on tool design and mechanical properties. They used a traverse pace of 40 mm/min and a tool pin rotational velocity of 900 rpm, employing threaded straight cylinder type pins, square type pins, and threaded tapered screw-type pins. The shape of the tool pin had a significant effect on joint efficiency, with the square pin achieving 85% joint efficiency compared to the original metal piece.

Valate et al. [36] investigated the effects of various traverse speeds, tool pin shapes, and tool rotational velocities on welded joints. The study was conducted on 6 mm thick AA6082-T6 alloy, using cylindrical screw and smooth tapered threaded tools with different dimensions. The results showed that the cylindrical smooth tapered tool pin achieved 48% tensile strength compared to the base metal at certain parameters, while the cylindrical threaded screw pin reached 60% tensile strength under different process conditions.

Srinivasulu et al. [37] conducted a study on the bending strength of 5 mm FSWed AA6082. They varied the tool speed between 1800 rpm and 2400 rpm, with similar traverse speeds of 50 and 30 mm/min. The shape of the tool was tapered cylindrical with a shoulder-to-pin ratio of 3 and a tool tilt angle of 0°. The bending test showed that all FSWed joints broke before reaching 90°, while the base metal achieved a 180° bend. The bending failure occurred at the Heat Affected Zone (HAZ) of the advancing side due to its lower hardness values. The parameter combination of 30 mm/min and 2400 rpm outperformed the others, and face bends were superior to root bends, which showed tunnel flaws. Joints with a rotational velocity of 1800 rpm and a traverse pace of 50 mm/min displayed more flaws.

Similarly, Krzystof et al. [38] researched the microstructure and mechanical properties of FSWed AA6082 using welding parameters of 710 mm/min and 710 rpm with a plate thickness of 6 mm. The tool pin had a threaded 8 mm diameter with a spiral grooved shoulder of 25 mm diameter and a tool tilt angle of 1.5°. After two weeks, defects were observed with the parameters of 710 mm/min and 710 rpm. The microstructure of the advancing side displayed varying harsh borders while the retreating side had a consistent microstructure. SEM analysis revealed a less bonded surface in the fractured workpiece, leading to a weaker joint area near the weld face due to microhardness variations.

2.3 Friction stir welding of AA5083

Friction stir welding (FSW) is governed by a set of process parameters that are set for a particular weld run. These parameters affect joint integrity and the quality of post-welding features that cannot be reversed. It is for this reason that these parameters must be properly determined beforehand. The parameters discussed in this section are tilt angle, rotational speed, traversing speed and dwell time.

One of the aluminium workpieces to be used in this study will be in the AA5083 series of strain-hardenable alloys with magnesium as the main alloying element. AA5083 is a non-heat-treatable alloy type with an ultimate tensile of 350 MPa. The type is widely used in the marine sector, parts of petrol-driven transportation vehicles, military vehicles, bridges and buildings, cryogenic pressure vessels, hulls of small boats, and superstructures in ships. These alloys have weldability, corrosion resistance and good toughness.

Devaraju et al. [39] used AA5083 to fabricate an FSW joint with the purpose of examining the relationship between mechanical properties and microstructure. The application of a range of FSW parameter conditions revealed that the microstructure zones had an equiaxed grain. Reduction of the heat flow influenced the grain of the stirring zone and resulted in improvement of the mechanical properties of the joint.

Jaiswal et al. [40] investigated the relationship between FSW parameters and the mechanical properties of an AA5083 joint. The tool pin geometries were tri-flute high-speed

steel, tapered threaded and tapered smooth tool. The rotational speeds for all the tool pins were set at 1000 rpm, 800 rpm and 600 rpm, with a steady traverse velocity of 50 mm/min. The tapered smooth and threaded tool had decent results but the best contribution to the mechanical properties was the tri-flute.

Saravankumer et al. [41] also researched the variable process parameters to be used on AA5083 via FSW. They tried traverse speeds of 40 mm/min for tool pin rotational speeds of 1220 rpm and 1400 rpm and 20 mm/min for rotational speeds 900 and 710 rpm. The tool pin geometries were circular threaded and smooth. The results showed that the circular threaded tool achieved a good weld via parameters of 1220 rpm and 40 mm/min, with tensile strength of 205.1 N/mm^2 and hardness of 86.7 VHN.

Another study of the variable process parameters to be used on AA5083 via FSW was conducted by Ravindar et al. [42]. The traverse speed varied from 100 mm/min to 60 mm/min, with tool pin rotational speeds between 1100 and 700 rpm and a tool tilt angle of 90º to 91º. The results of the investigation were that the parameters of tool tilt angle 91º, 1100 rpm and 100 mm/min achieved the best joint weld with yield strength of 184.539 N/mm^2 and tensile strength of 255.464 N/mm^2, with 8.28% elongation.

Chander et al. [43] researched the mechanical and microstructure properties of FSW AA5083. The workpiece process parameters were a tool rotational velocity of 1800, 1400, 1120 and 900rpm and a steady traverse pace of 40 mm/min. Tool pin geometries were conical and threaded taper tools. The maximum microhardness was attained using the threaded taper tool at 900 rpm, the minimum at 1800 rpm. The conical taper tool, on the other hand, attained a minimum microhardness at 1400 rpm, while the maximum microhardness was attained at 1800 rpm. The joint had small grains across the entire weld because of recrystallization.

2.4 Friction stir welding of AA6082 / AA5083 dissimilar materials

Joining two dissimilar workpiece materials presents a considerable challenge because of their differing physical properties and chemical compositions. The resultant material differences in factors such as thermal expansion, melting points, and thermal conductivity, can lead to difficulties in the joining process and subsequent product performance. Overcoming these disparities and working within the limits of the materials is essential to achieve successful bonding.

Kumar et al. [44] focused on FSW of AA5083 and AA6082 to investigate the influence of process parameters on the achievement of the best tensile properties. They examined the effects of tool offset, shoulder diameter, and tool tilt. The results revealed that ultimate tensile strength and yield strength were independent of the offset values. The optimal combination of parameters resulted in a tensile strength of 210 MPa, yield strength of 203 MPa, and elongation

of 12%. This was achieved with a tool tilt angle of 1°, shoulder diameter of 18 mm, and a tool offset of 0 mm.

Leitao et al. [45] studied the FSW of AA5083 and AA6082 using a 6 mm plate. They explored the behaviour of excessive temperature plasticity and its relation to weldability. The research indicated that AA5083 exhibited a reduced yield strength compared to AA6082, with the latter alloy demonstrating better fusion characteristics. A study by Msomi and Mbana [46] on FSWed AA1050/AA5083 focused on microstructural analysis of the welded joint. The mechanical properties of samples extracted from different points in the weld were of particular interest. The results showed variations in ultimate tensile strength at different points along the weld. The base metal of AA1050, in particular, demonstrated higher UTS values and a better-coarsened grain at the Heat-Affected Zone (HAZ) compared to AA5083.

Jain et al. [47] conducted a comparative investigation of FSW between dissimilar alloys AA6082/AA5083, aiming to assess the influence of various FSW parameters using the Taguchi method. The welding parameters tested included traverse speed, tool pin rotation speed, tool pin geometries, and shoulder diameters. The research found that UTS was primarily affected by three parameters: tool rotation speed, traverse speed, and shoulder diameter. Tool rotation speed had the most significant impact at 64.08%, followed by traverse speed at 29.55% and shoulder diameter at 5.67%. For elongation, the tool rotation speed also played a crucial role with 48.29% influence, followed by tool shoulder diameter at 36.71% and welding speed at 11.06%.

In their research on the FSW of AA6082/AA5083, Kumar et al. [48] aimed to optimise the process parameters. Their study made use of a constant traverse velocity of 20 mm/min and tool rotational velocities of 1400, 1000, and 710 rpm, along with square and circular tool pin shapes. The base metal's grain size was observed to be non-equiaxed, with a finer grain structure exhibited at the nugget zone. Tool rotational speed was found to be directly related to grain size, with higher rotational speeds resulting in smaller grains. AA6082 displayed lower hardness than AA5083 in the stir zone, and an increase in tool rotational speed led to a decrease in hardness values, unaffected by the tool pin shape.

2.5 Friction stir processing of AA6082

Da Silva et al. [49] explored the fatigue behaviour of AA6082 welds produced using metal inert gas (MIG) welding and compared it to the performance achieved through friction stir processing (FSP). The FSP technique was utilised to refine the microstructure and eliminate defects in the weld. The FSP parameters used were a tool rotation velocity of 1500 rpm, a traversing speed of 240 mm/min, and a tilt angle of 25°. The results indicated that while the hardness and mechanical properties of the MIG weld remained unaffected by FSP, its ductility and fatigue resistance were notably enhanced.

In a related study, Chanakyan et al. [50] investigated the effect of hexagonal tool profiles in FSP. They found that this modification led to a 95% improvement in hardness and Ultimate Tensile Strength (UTS) for AA6082 material. The tensile strength of the FSPed AA6082 increased with increments in the traverse velocity and rotational velocity of the tool up to certain optimised values, beyond which it started to decrease. The mechanical properties obtained through the selected welding parameters reflected improved UTS and HV (hardness values).

Jiang et al. [51] also conducted research on the application of FSP to AA6082 in order to enhance its mechanical properties and damping capacity. A tool with a concave shoulder of 10 mm diameter and a tapered, threaded pin of 3.7 mm length and 4 mm diameter was employed. The FSP parameters involved a tool rotation rate of 200 rpm and a constant traverse velocity of 50 mm/min. The results showed that FSP induced a significant refinement of micron-sized particles and a more uniform dispersion of particles within the aluminium matrix. In comparison to the base metal, the FSP-treated sample exhibited higher ductility and ultimate strength.

These studies all highlight the benefits of utilising FSP as a grain refinement technique for enhancing the mechanical properties, ductility, and fatigue resistance of AA6082 welded materials. The selection of specific parameters and tool profiles plays a crucial role in optimising the results of FSP, which has proved a valuable method for improving the overall performance of welded materials in various engineering applications.

2.6 Friction stir processing of AA5083

Pradeep et al. [52] conducted research on AA5083 aluminium alloy to explore the potential benefits of employing a multi-pass method through friction stir processing (FSP). The study involved setting specific process parameters, such as a tool pin diameter of 4 mm, tool pin length of 3 mm, traverse velocity of 24 mm/min, and tool rotational velocity of 1200 rpm. A cylindrical tool with a shoulder diameter of 24 mm applied a constant downforce of 8 kN on a 6 mm thick AA5083 plate. The findings revealed a high density of dislocations within the coarse grain structure of the AA5083.

In another investigation by Vignesh et al. [53], the FSP technique was employed to enhance the wear resistance of AA5083 aluminium alloy. The study aimed to identify the optimal process parameters to achieve the best results. These optimal parameters were determined to be a traverse velocity of 30 mm/min, tool rotational velocity of 1000 rpm, and shoulder diameter of 18 mm. The best wear resistance result obtained was 8860 N.m/kg. The experimental outcomes were in close agreement with the model predictions, which indicated a wear resistance of 8836 N.m/kg.

Hussein and Al-Shammari [54] carried out research on AA5083 joints using both friction stir welding (FSW) and friction stir processing (FSP) to assess the fracture behaviour and fatigue of the joints. The results indicated that the FSPed workpiece exhibited significant improvements compared to the FSWed workpiece when subjected to constant stress, demonstrating superior performance.

These studies provide valuable insights into the potential role of optimised FSP in enhancing the material properties of the AA5083 aluminium alloy – microstructure, wear resistance and mechanical behaviour – paving the way for further developments and applications in various industries. The comparison between FSWed and FSPed joints highlights the advantages of the latter process, particularly in terms of stress tolerance and performance.

2.7 Friction stir processing of AA6082 /AA5083 dissimilar materials

De Jesus et al. [55] conducted a study investigating the influence of friction stir processing (FSP) on the fatigue strength of MIG T welds in AA6082 and AA5083 aluminium alloys. They sought to understand how tool geometry affect the quality of the processed regions in the welds. Through FSP, the imperfections in the MIG welds were effectively removed, resulting in improved weld integrity.

In another study by Mabuwa and Msomi [56], a dissimilar joint between AA6082 and AA8011 aluminium alloys was subjected to friction stir processing. The main focus was on examining the fatigue behaviour of the joint and the impact of the workpiece material positioning during FSW. Two types of joints were created: AA6082/AA8011 and AA8011/AA6082. Numerous tests were conducted on the joints, with a significant finding emerging from analysis of the microstructure. The researchers observed that changing the position of the workpiece in the joint affected the grain sizes within the microstructure. Specifically, when the advancing side of AA6082 was used, the joint exhibited remarkable improvements in tensile strength, ductility, and fatigue strength compared to when AA8011 was on the advancing side. Additionally, the microstructure hardness was enhanced, exhibiting hardness of 78 HV for the AA6082 side compared to 68 HV for the AA8011.

These findings indicate that the proper positioning of workpiece materials during friction stir processing can significantly influence the mechanical properties and performance of dissimilar joints. The research sheds light on the importance of optimising FSP parameters and understanding the microstructural changes that occur during the process, and provides valuable information for the fabrication of high-quality welds in aluminium alloys. Further investigation in this area could lead to the development of tailored approaches to enhancing the fatigue resistance and overall mechanical behaviour of friction stir processed dissimilar joints.

2.8 Friction stir processing of AA6082/AA5083 dissimilar materials with reinforcement particles

Thangarsu et al. [57] conducted a study on FSP technique to blend AA6082/TiC aluminium Matrix Composites (AMCs) and analyse the effect of TiC particles. They used a tool rotational velocity of 1200 rpm with a vertical perpendicular force of 10 kN and a single pass at a traverse velocity of 60 mm/min. The test results showed that the addition of TiC particles improved the strength of the AA6082/TiC composite. The ultimate tensile strength increased by 222 MPa at 0% TiC content and reached 382 MPa at 24 vol%. The microhardness also improved from 62 HV at 0% TiC to 149 HV at 24 vol% TiC.

In another study, Thangarasu et al. [58] investigated the mechanical and wear properties of AA6082 composites reinforced with SiC, TiC, WC, Al2O3, and B4C particles through FSP. The TiC-reinforced workpiece showed the highest microhardness of 115 HV and the lowest wear rate compared to material reinforced with SiC, WC, Al2O3, and B4C particles. Thangarasu et al. [59] also studied the wear resistance of AA6082/TiC composite using the FSP technique and found that increasing the TiC content enhanced the wear resistance, reaching a minimum wear rate of 0.00303 mg/m at 22 vol% TiC.

Huang and Shen [60] conducted research on the mechanical properties of a Al 5083/Ti workpiece under air and water processing environments. The study revealed that finer recrystallised grains were found in the workpiece due to the cooling effect of water, resulting in improved yield and tensile strength. Kumar et al. [61] investigated the FSP of AA5083-B4C/SiC/TiC composite to study its wear and mechanical properties. The results showed that AA5083/B4C composite had the best wear rate of 18x10^-5 mm3/Nm. However, its microhardness and tensile strength, with values of 132.56 ± 2.52 HV and 349 MPa, respectively, were no better than those of the AA5083/SiC/TiC composite.

2.9 Summary

No literature was found on the formation of composites using AA5083/AA6082, indicating a gap in the research that needs to be addressed. This study focuses on FSP as an improvement technique for aluminium matrix composites (AMCs). Despite the different melting points of AA5083 and AA6082, they have shown compatibility with the FSW technique. For optimal mixing during the FSW process, it is recommended that the harder material be placed on the advancing side. Using a converted milling machine is a cost-effective method for conducting FSW, making it accessible to most researchers. Surprisingly, there is little to no reported research on the use of coal as a reinforcing agent in the post-weld processing of joints. This study aims to remedy this absence by focusing on the mechanical properties of friction stir processed AA5083/AA6082 dissimilar joints reinforced with coal. The joints will undergo

mechanical and metallurgical tests with and without coal reinforcement. The research thereby aims to contribute useful insight into the potential use of coal as a reinforcement material in friction stir processed dissimilar joints.

CHAPTER THREE

EXPERIMENTAL SET-UP AND PERFORMANCE

This chapter features discussion of the apparatus used in performing all the tests in the study. The friction stir welding technique used in producing welds later subjected to friction stir processing with and without reinforcing coal powder particles will be described. The conditions of welding and the tests performed on the processed welds are explained.

3.1 Set-up of the welding

The apparatus used in fabricating the welded joints comprised the following:

- GEKA cutting machine
- Circular saw
- Friction stir welding machine
- Lathe machine
- Hand drill machine

3.1.1 The GEKA Hydracrop machine

The Hydracrop machine was used to cut material using hand- and foot-powered techniques (see Figure 3.1.1). The model used was the GEKA Hydracrop machine HYD 110S, which is an efficient, affordable and easy-to-use machine utilised in metalworking and fabrication. It is capable of cutting, punching and bending metal sheets with precision and speed. It also has built-in safety features, making it safe and reliable to use. It has a gauging device to measure the size of the material, an upper and lower blade to cut the workpiece, and a shear table to rest the workpiece while it is being cut. The first step before using the Hydracrop is to mark the plates or sheets to be cut for easy alignment. Once the plates are aligned with the Hydracrop blade, the cutting blade is let down by pressing the foot pedal. The cut-off section falls off into the box provided.

Figure 3.1.1: GEKA Hydracrop machine.

3.1.2 Circular saw

A portable hand-held circular saw was used to cut down to size the pieces cut using the Hydracrop machine. Figure 3.1.2 (a) shows a Bosch professional GKS 140 model circular saw, which is a compact, robust, yet light-weight tool. A circular saw is used to cut through materials such as wood, plastic, or metal with a circular blade. It is a versatile tool that can be used for a variety of tasks, such as making straight cuts, bevel cuts, crosscuts, and mitre cuts. It is widely used in the construction industry and DIY projects. The circular saw blade for aluminium alloy material is presented in figure 3.1.1(b). The cutting fluid presented in figure 3.1.1(c) is used for lubricating the workpieces the during cutting process. The circular saw cutting process is explained below.

The initial step is to set up the circular saw. After the saw has been securely placed on a work surface, the appropriate blade for the job on hand is selected and properly attached to the saw's arbor. To ensure precision, the material intended for cutting is carefully measured and marked using a pencil or marker. Next, the saw is adjusted to achieve the desired cutting depth and angle, aligning it with the markings on the material. Adjustment is accomplished by modifying the blade's depth and the angle of the saw shoe or base plate. After the set-up is complete, the saw is switched on, causing the blade to rotate at a high speed. The saw is positioned over the marked line on the material and the blade is allowed to gently touch the surface. With slight pressure applied to the material to maintain its position, the operator pushes the saw forward along the marked line, ensuring a straight cut. Upon fully traversing the material, the operator turns off the saw and removes it from the work surface. Lastly, the

cut edge of the material is refined by removing any rough edges or splinters with sandpaper or a file.
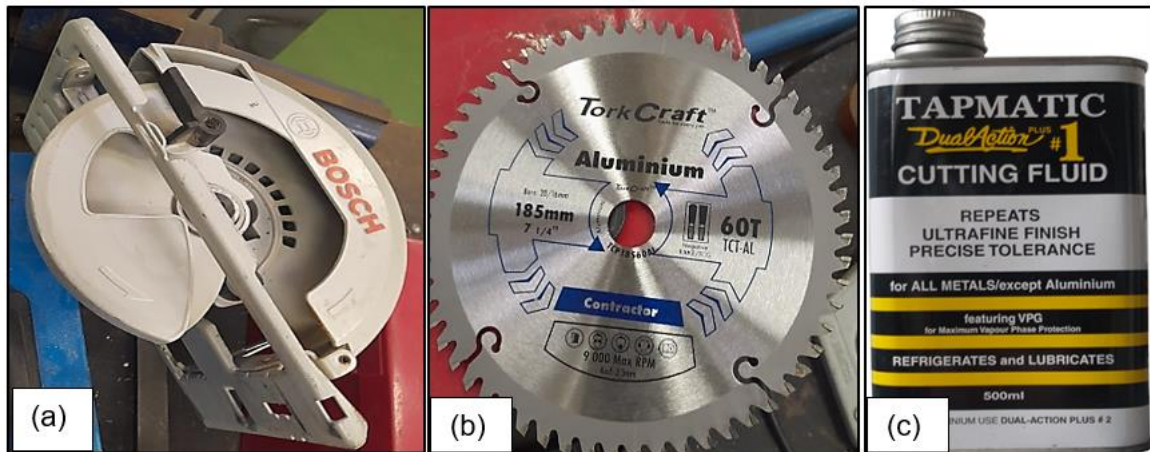
Figure 3.1.2: (a) circular saw, (b) circular saw blade, and (c) cutting fluid.

3.1.3 Friction stir welding machine

A friction stir welding machine was achieved by converting a conventional milling machine (see Figure 3.1.3). Lagun FU.1-LA is a universal milling machine designed to provide precision and accuracy in various machining operations. It has a spindle speed of up to 4000 rpm, a table size of 1200 x 300 mm, a trapezoidal thread spindle taper, and a range of other features including a digital read-out, rapid traverse, and adjustable backlash. It is suitable for a wide range of applications, from general milling to detailed and intricate machining. In performing the friction stir welding, two aluminium alloy plates are tightly clamped together on the reconfigured milling machine bed. Prior to FSW, the process parameters – like the rotational speed, welding speed and traverse speed – are determined and set. The rotating friction stir welding tool is plunged into the plates and kept stationary for a few seconds to allow the temperature to stabilise. The rotating tool is then released so that it travels along the edges of both plates that are being welded. The rotating tool travels from the start to the end of the plates resulting in the accomplishment of the weld. The tool is then retracted, leaving a small exit hole. The same machine and process are used for the friction stir processing technique.
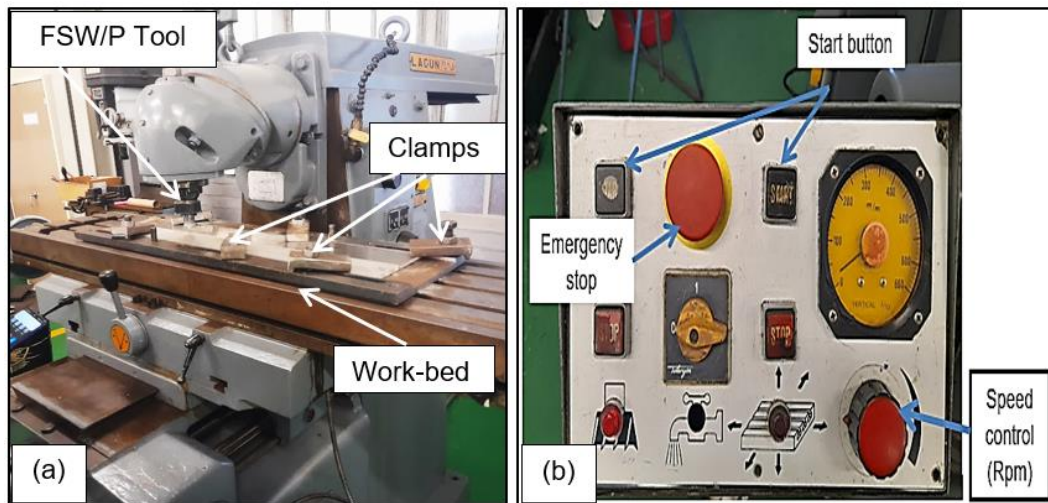
Figure 3.1.3: (a) Lagun FU. 1-LA milling machine, and (b) Control panel for friction stir welding machine.

3.1.4 Lathe machine

The lathe machine shown in figure 3.1.4 was used to manufacture the pin-less tool. The YUNNAN CY CY-L1640G lathe machine is a versatile tool for the precision machining of metal and other materials. It is used to shape and cut materials into desired shapes and sizes using a rotating cutting tool and a fixed material support. The cutting tool is typically controlled by a manual or automated mechanism while the material is supported on a workpiece holder. Lathe machines can be used to produce a variety of products, including screws and pins. The basic working principle of a lathe machine involves the rotation of a workpiece about its axis, while a cutting tool is applied to shape the workpiece to the desired form.

In the process of preparing a workpiece for use with the lathe machine to manufacture a tool, the first step is to select the appropriate material for the tool and cut it to the desired length. The workpiece is then securely clamped in the lathe chuck, which facilitates rotation during the machining process. Next, the cutting tool is mounted on the tool post, enabling movement along the lathe's carriage. The tool's positioning is crucial in achieving the desired shape and size for the workpiece. The angle and depth of the cut are determined by the tool's relative position to the rotating workpiece.

Once the workpiece and cutting tool are set up properly, the lathe machine is started. The workpiece rotates at a consistent speed, while the cutting tool is moved methodically along the workpiece, skilfully removing material to create the desired contours. Precise control of the cut's depth and direction is attained by adjusting the position and angle of the cutting tool. After achieving the initial shaping, the tool undergoes finishing touches. This entails executing a series of smaller cuts using a finer cutting tool, ensuring a smooth surface and finalising the tool's shape.

Once the shaping process is complete, the tool is removed from the lathe machine. At this point, additional finishing operations like polishing or heat treatment may be conducted to further refine the tool's characteristics and surface quality.
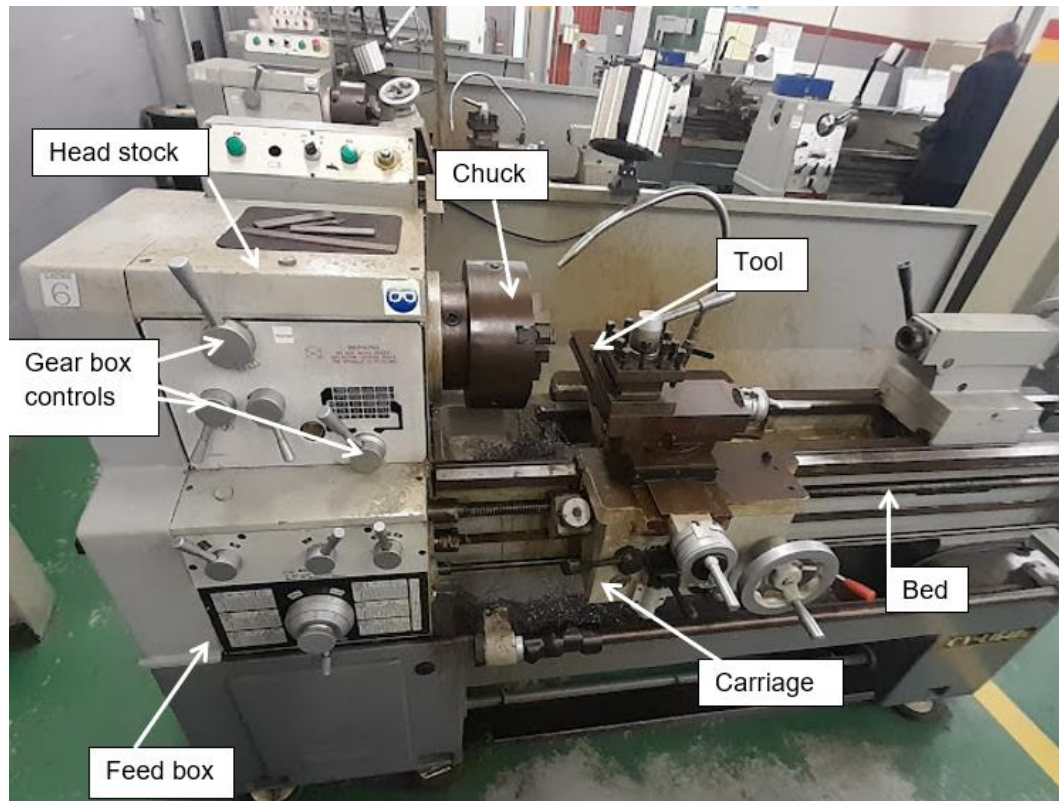
Figure 3.1.4: Lathe machine.

3.1.5 Hand drill machine

Figure 3.1.5 shows a portable hand drill, the Bosch Easy Drill 1200 model, which is used for drilling holes in various materials, including aluminium alloys. The process of drilling begins with the insertion of a drill bit suitable for the work to be performed. The step is to measure the area where the hole needs to be drilled and make markings to guide the process. The workpiece is then clamped in position to drill the desired hole.

Figure 3.1.5: Drill machine and drill bits.

3.2 Welding performance

The materials used in this study were samples of AA5083 and AA6082 with a thickness of 6 mm. The dissimilar materials were cut into pieces with the dimensions of 70 mm by 530 mm as depicted in Figure 3.2, using the Hydracrop machine. The dimensions were chosen based on the friction stir welding machine bed. Table 3.2(a) shows the chemical composition of the materials used and Table 3.2(b) the mechanical properties of the materials used.

Table 3.2(a): Chemical composition base material alloys 5083 and 6082 [5].

Spec: BS EN 573-3:2019	AA5083	AA6082
Chemical Element	**% Present**	
Manganese (Mn)	0.40 - 1.00	
Iron (Fe)	0.40 max	0.0 - 0.50
Copper (Cu)	0.10 max	
Magnesium (Mg)	4.00 - 4.90	0.60 - 1.20
Silicon (Si)	0.0 - 0.40	0.70 - 1.3
Zinc (Zn)	0.0 - 0.10	0.0 - 0.20
Chromium (Cr)	0.05 - 0.25	0.0 - 0.25
Titanium (Ti)	0.15 max	0.0 - 0.10
Other (Each)	0.0 - 0.05	
Others (Total)	0.0 - 0.15	
Aluminium (Al)	Balance	

Table 3.2(b): Mechanical properties of aluminium alloys 5083-H111 and 6082-T651 [5].

BS EN 485-2:2008 sheet 0.2 - 6.3mm thick		
Property	Value	
	AA5083-H111	AA6082-T651
Proof Stress	150 MPa	310 MPa
Tensile Strength: Ultimate (UTS), MPa	300 MPa	340 MPa
Shear Strength	175 MPa	210 MPa
Elastic (Young's, Tensile) Modulus	68 GPa	69 GPa
Elongation	23 %	11%
Hardness Vickers	75 HV	100 HV
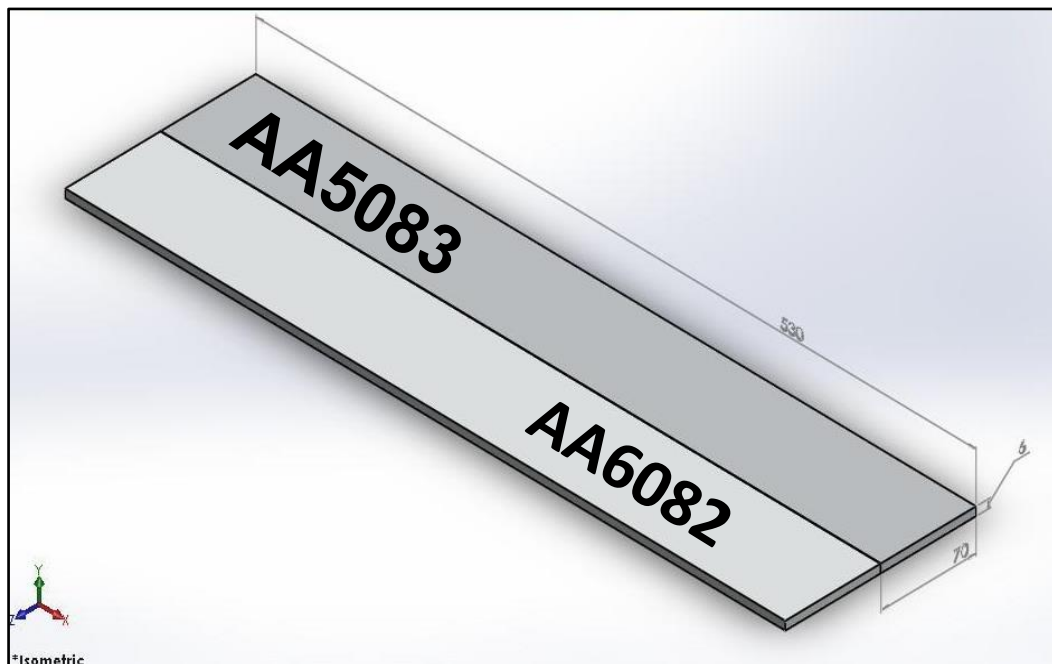
Figure 3.2: SolidWorks diagram of the plates dimensioned in mm.

3.2.1. Friction stir welding

Friction stir welding (FSW) was performed on the AA5083 and AA6082 6mm-thick plates. The plates were fixed to the FSW machine bed using bolts and clamps to avoid movement during the FSW process, as shown in Figure 3.2.1(a). Figure 3.2.1(b) shows the SolidWorks diagram of the tool used in the FSW process. The tool was made of high-carbon steel. It was a fixed type of tool, meaning that the probe was fixed and was suitable for this kind of study since the workpieces had a uniform thickness. The diameter of the tool shoulder was 20mm, and at the end of the shoulder was a tapered probe with a length of 5mm. Table 3.2.1 presents the FSW parameters utilised. The single-pass FSW method was used to manufacture the joints. No extraordinary treatment was applied before welding. Figures 3.2.1(c) and 3.2.1(d) show the FSW process of the AA5083/AA6082 and the resultant dissimilar FSW joint. The FSW

workpieces were joined at room temperature. It should be noted that during the FSW the aluminium alloy 5083-H111 was positioned on the advancing side and 6082-T651 on the retreating side. Three dissimilar combinations were produced: one was left unprocessed, and two were reserved for friction stir processing with and without reinforcement particles.
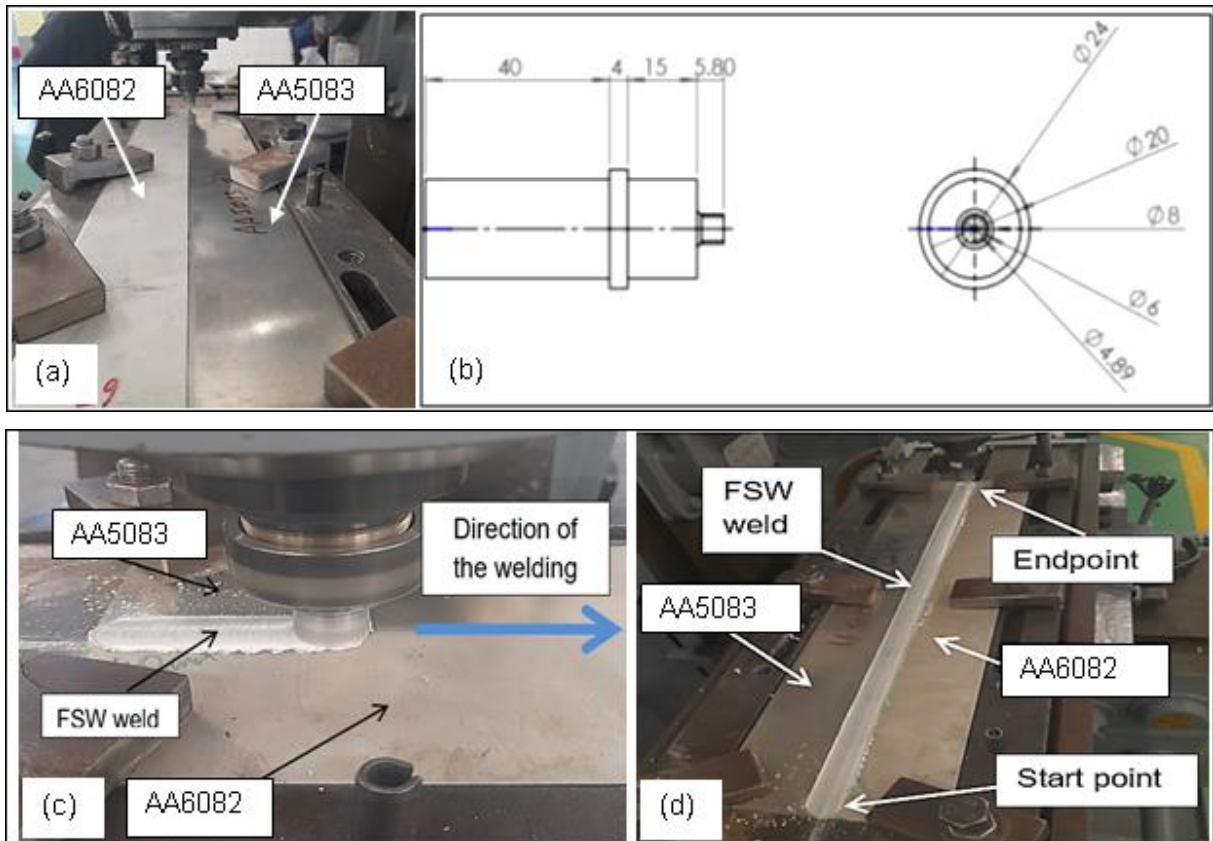
Figure 3.2.1: (a) FSW setup, (b) Solidworks diagram of the pin tool, (c) FSW process of the AA5083/AA6082, and (d) FSW AA5083/AA6082 weld.

Table 3.2.1: FSW parameters.

Rotational speed (rpm)	Welding speed (mm/min)	Vertical force (kN)	Traverse speed (mm/min)	Tilt angle
1400	30	15	40	2º

3.2.2 Friction stir processing

Friction stir processing was performed on the FSWed joint using the reconfigured milling machine. The parameters used to perform FSP were the same as those used for FSW (Table

3.2.1). Variation in transverse speeds, tool pin shape type and tool rotational velocity would have changed the mechanical properties of the welded joints. Keeping the parameters the same throughout guaranteed consistency across different workpieces, making sure that the outcomes were as accurate as possible. Additionally, using the same parameters enabled easier comparison and evaluation of workpiece performance over time and across different workpieces. If the parameters were constantly changing, it would have been difficult to determine whether changes in the performance/results were due to improvements in manufacturing or changes in the parameters [28, 29]. The performance of the FSP on the FSW welded joints is portrayed in figure 3.2.2(a), while figure 3.2.2(b) shows the produced FSP joint with a small plunge hole from the tool when it is unplugged from the plate.
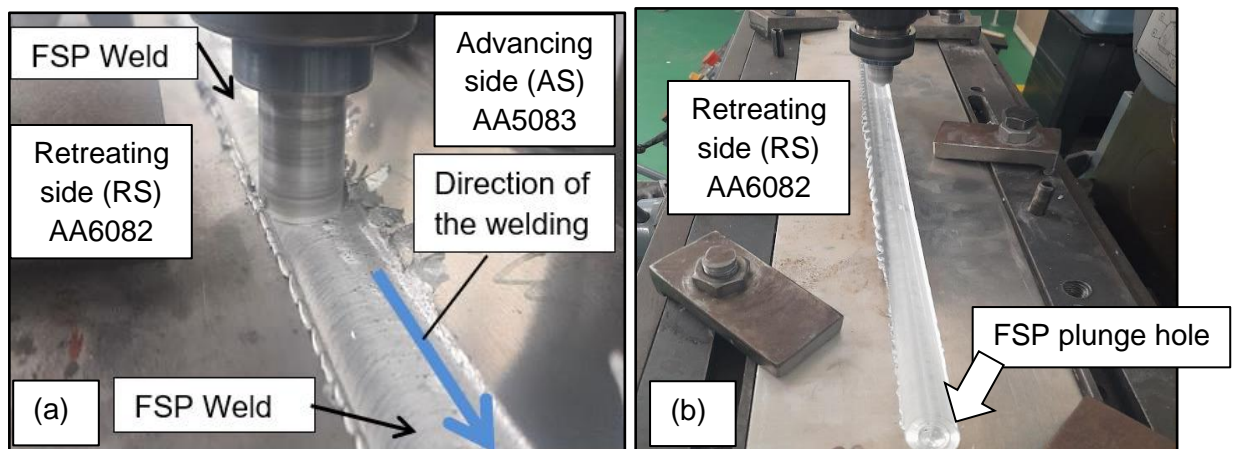
Figure 3.2.2: (a) FSP process without reinforced coal, and (b) Produced FSP joint.

3.2.3 Friction stir processing with reinforcement coal powder particles

Fine crushed organic braai coal was used as reinforcement particles on the previously welded FSW joint. Holes were drilled 2 mm in diameter and 5.8 mm in depth at an equal distance of 5 mm apart across the 530 mm FSW plate. These were filled with equal volumes of coal powder. Figure 3.2.3(a) shows the joint with drilled holes. The coal was crushed by hand in a granite pestle and mortar. The fine coal powder thus produced is shown in Figure 3.2.3(b). It was sent to SEM for analysis to determine the chemical composition. The blind holes were then covered through FSP with a pin-less tool as depicted in figures 3.2.3(c) and 3.2.3(d).
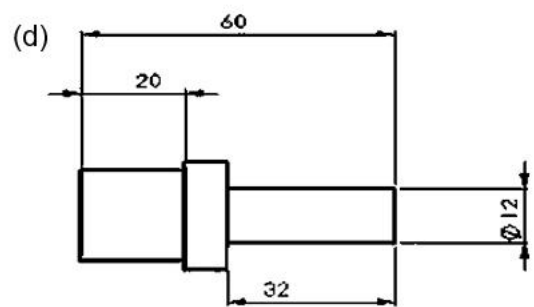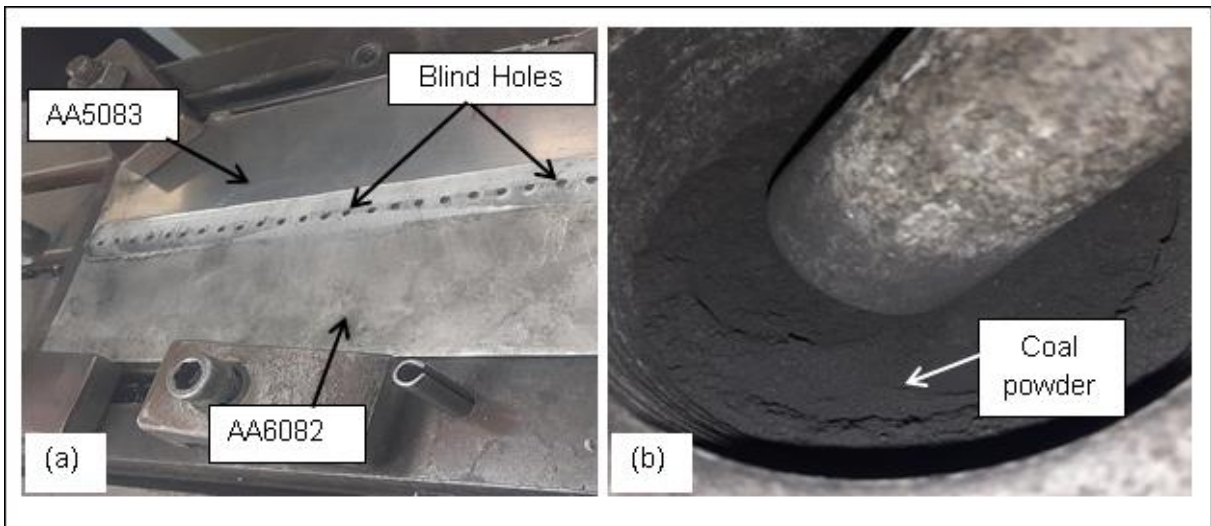
Figure 3.2.3: (a) Joint with drilled blind holes (b) Crushed coal powder (c) Pin-less tool (d) Solidworks of the pinless tool with dimensions in mm.

Figure 3.2.3(e) shows the FSP process of covering the holes reinforced with coal particles. This was done to avoid the coal particles from splashing. The weld produced by the pin-less tool produced large flash material on the edges of the joint. The tool with a pin was then used for a single-pass FSP process on the same joint along the line of the blind holes as depicted in Figure 3.2.3(f). Figure 3.2.3(g) shows the final joint produced with reinforced coal particles.
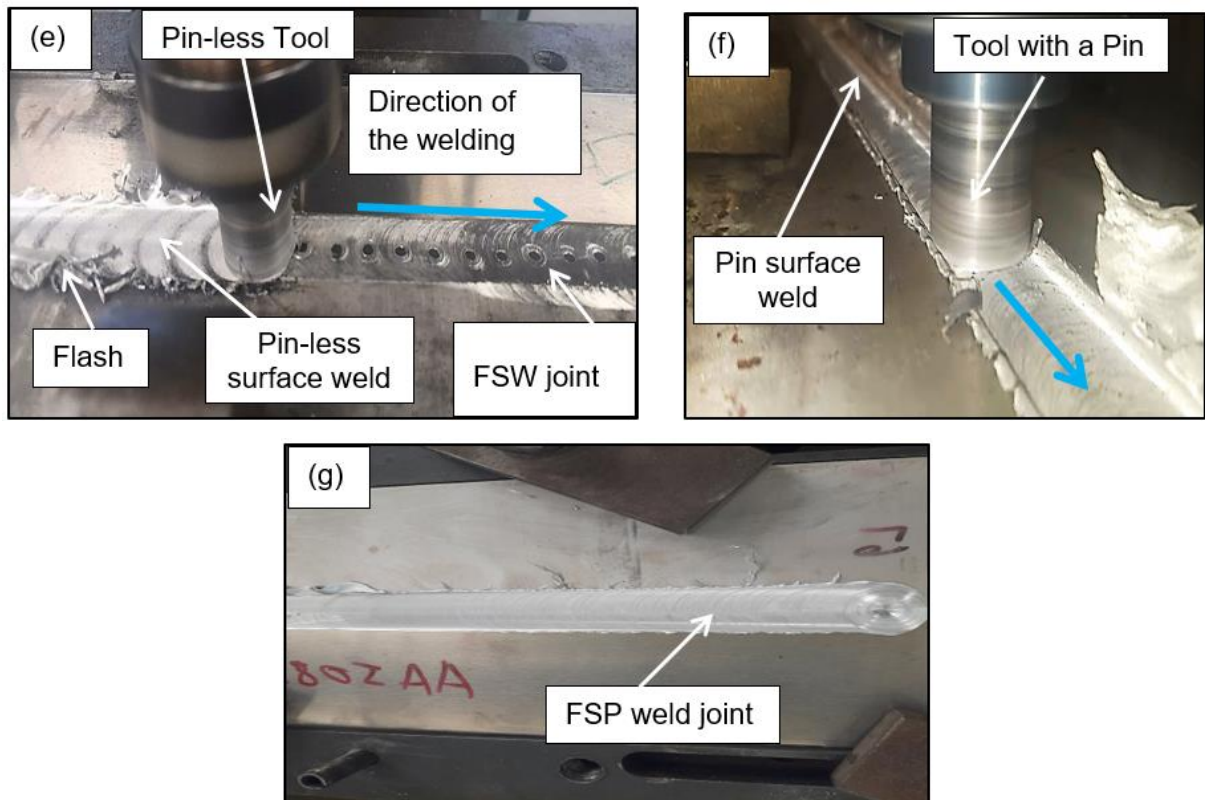
Figure 3.2.3: (e) FSP using a pinless tool (f) FSP using a tool with a pin, and (g) Final produced FSPed joint with reinforced coal particles.

3.3 Weldments analysis preparation

The following were the equipment and techniques used in analysing the weld joints obtained through the steps explained above in section 3.2:

- Water jet machine
- Mounting press machine – Struers LaboPress 3
- Polishing machine – Struers LaboPol 5
- Sonic clean machine.

3.3.1 Water jet machine

Water jet cutting is a method of cutting materials using a high-pressure jet of water often mixed with an abrasive substance. It is often used in the construction of machine parts and is preferred for materials that are sensitive to the high temperatures generated by other methods. The water jet cutting machine shown in Figure 3.3.1 is used in a variety of industries including mining and aerospace. The machine uses the principle of passing high-pressure water through a small nozzle to accelerate it to an extremely high speed by using a hydraulically powered piston to force the water through the nozzle. This high-speed water jet is focused on a thin beam of water and cut through the work piece placed in its path. The major benefit of water jet

cutting is that it does not leave a heat-affected zone, meaning it does not change the intrinsic properties of the material as it cuts through it. This implies that it is feasible to produce sharp corners, bevels, pierce holes, and shapes with minimal inner radii using a water jet cutting machine. Additionally, such a machine is capable of crafting intricate cuts in materials. With specialised software and 3D machining heads, complex shapes can be produced. An outside contractor performed the work of cutting out the sample parts for testing.

Figure 3.3.1: Water jet machine.

3.3.2 Mounting press machine - Struers Labopress 3

The Struers Labopress 3 machine shown in Figure 3.3.2 is used for mounting specimens in a hard epoxy resin. The mounting machine works by placing the specimen on the ram. A suitable resin is then poured into the cylinder through a funnel. The upper ram will be covered in with mould release agent on all its surfaces. The machine top is placed on the mounting cylinder and pressed down counter-clockwise. The ram is then lowered, and a heated platen comes into contact with the specimen. This heats the epoxy resin and causes it to harden. The specimen is then removed, and the hardened epoxy provides a secure and stable platform for the specimen to be held in place during the testing process. The Struers Labopress 3 features a digital pressure control system, which is designed to provide consistent pressure during the mounting process for an optimum result. The machine also features a temperature control system, which allows for precise and repeatable temperature settings for the platen.

Figure 3.3.2: Struers Labopress 3 machine.

3.3.3 Polishing machine - Struers Labopol 5

The Struers Labopol 5 Polishing machine depicted in Figure 3.3.3(a) grinds and polishes various kinds of metal. When placing the metal on the machine and choosing between the grinding or polishing disc, then set the speed at 50 to 500 rpm. The start button is then pressed to start the polishing process, which continues until the desired surface finish is achieved. The sample is then further polished by spraying the polishing or grinding agent onto the material and spinning it at the set speed. The set speed and grinding or polishing agent used will depend on the sample material being polished or ground. The Struers Labopol 5 is designed to make polishing and grinding samples easier and faster, as well as providing a consistent finish. It is also designed to be user-friendly, with an easy-to-use interface and simple operation. Figure 3.3.3(b-f) shows the polishing pads with appropriate polishing chemical agents.
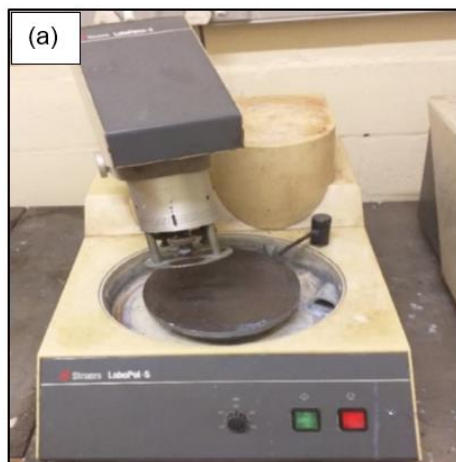
Figure 3.3.3: (a) The Struers LaboPol-5 polishing machine.
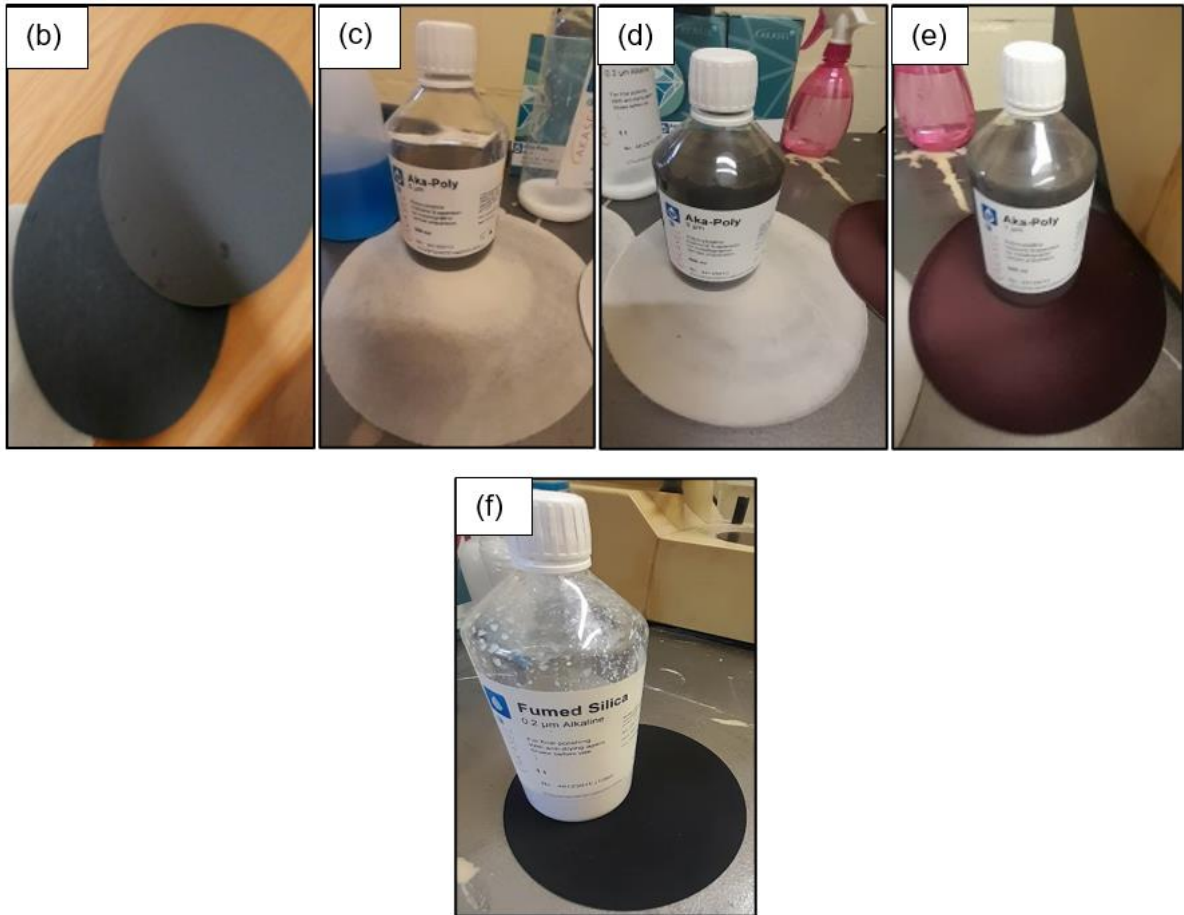
Figure 3.3.3: (b) Polishing paper grit P320 and grit P1200; (c) Aka-Poly 6μm polycrystalline diamond suspension with Aka-Moran-U polishing pad; (d) Aka-Poly 3μm with Aka-Daran polishing pad; (e) Aka-Poly 1 μm Aka-Napal polishing pad, and; (f) Fumed silica 0.2 μm with Aka-Chemal polishing pad.

3.3.4 SonicClean machine

The SonicClean machine shown in Figure 3.3.4 is a cleaning machine that uses a combination of sound waves and cleaning agents to remove dirt, dust, and other debris from surfaces. The sound waves penetrate the surface to loosen the particles, while the cleaning agents lift and remove the particles. The SonicClean machine is especially useful for cleaning delicate materials such as ceramic, glass, and jewellery. It is also used for cleaning industrial parts, such as bearings and gears. The SonicClean machine provides an efficient and cost-effective method of cleaning surfaces.

Figure 3.3.4: SonicClean machine.

3.4 Performance of specimen preparation

This section covers the planning and preparation of the specimens for all the tests conducted.

3.4.1 Tensile tests specimen preparation

The specimen dimensions (in mm) are illustrated in Figure 3.4.1(a). The dog bone-shaped specimen was drawn using the Solidworks design software, and then cut using the water jet machine. A sample of a completed tensile test specimen is presented in Figure 3.4.1(b). The ASTM E8 standard was used to design the specimen and its geometry [62].
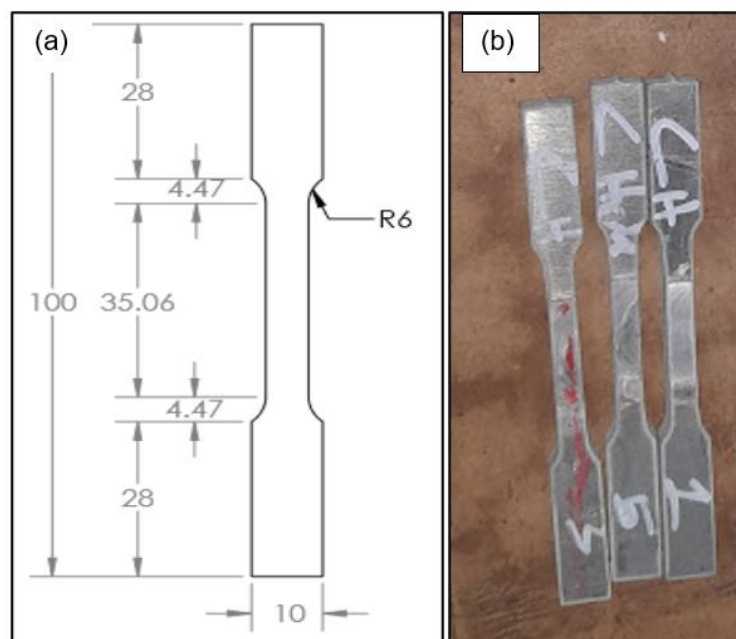
Figure 3.4.1: (a) Drawing of dog bone-shaped specimen (b) Sample dog bone cut-out.

3.4.2 Specimen preparations for a flexural test

The flexural tests specimen standard used was the ASTM E290 [63]. Figure 3.4.2 shows the flexural specimen dimensions of 20mm x 135mm x 6mm. The specimens were cut using the water jet machine. Finished samples of the specimens are presented in Figure 3.4.2(b).
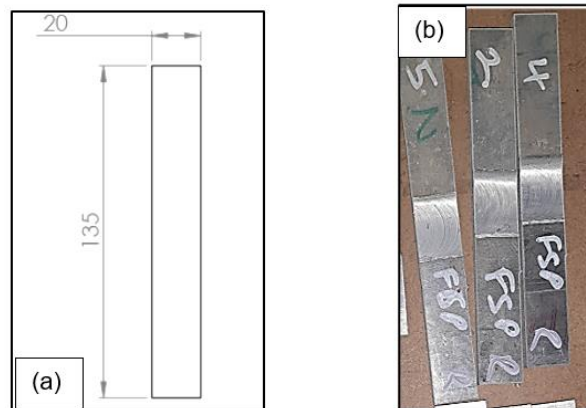
Figure 3.4.2: (a) drawing of flexural specimens, and (b) Cut specimen.

3.4.3 Microstructural tests specimen preparation

The microstructure specimen dimensions are illustrated in Figure 3.4.3(a). The water jet-cut specimens are shown in 3.4.3(b). The cut specimens were mounted in thermosetting plastic using the Struers Labopress 3 machine at a mounting temperature of 150ºC. The mounted specimen sample is shown in Figure 3.4.3(c). The mounted specimens were then prepared for microstructural analysis. The preparation involved the use of Struers laboPol 5. Various sandpapers were used to obtain the final product shown in Figure 3.4.3(d). The polished specimens were immersed in 0.5% hydrofluoric acid for 5 minutes. The specimen was then removed from the etchant and straightaway rinsed with water and alcohol. Alcohol was dried off the specimens using a hot hair dryer. The fully prepared (etched) specimens are shown in Figure 3.4.3(e).
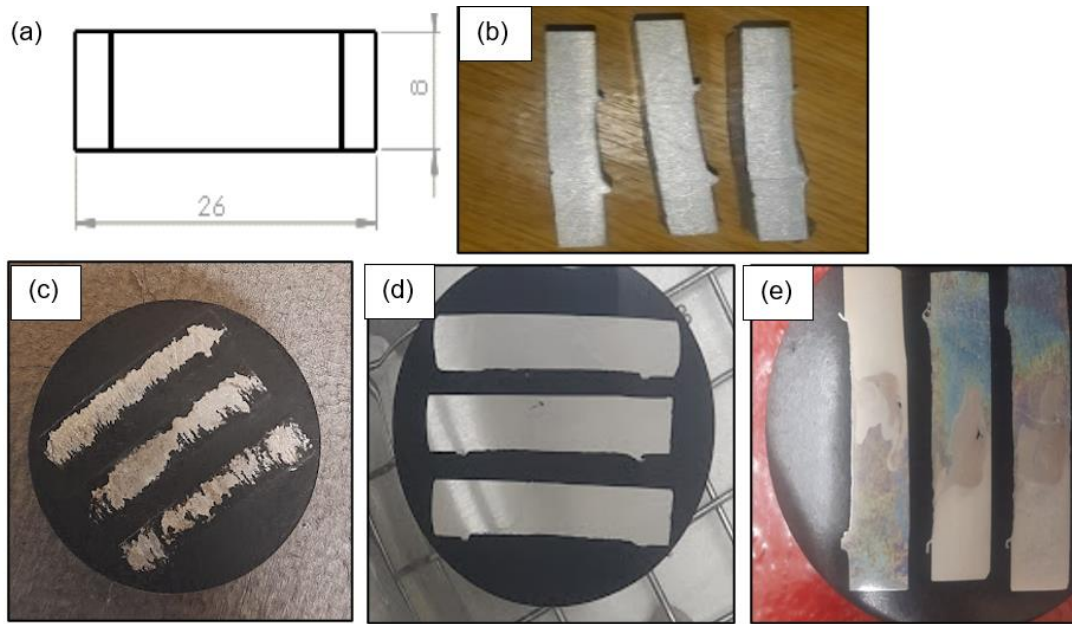
Figure 3.4.3: (a) Solidworks specimen with dimension in mm; (b) Water jet-cut specimens (side view); (c) Mounted specimens; (d) Polished specimens, and; (e) Etched specimen.

Table 3.4: Keller's reagent etchant.

Solution	Quantity
Distilled water ($H2O$)	95 ml
Hydrochloric acid (HCl)	1.5 ml
Hydrofluoric acid (HF)	1.0 ml
Nitric acid (HNO_3)	2.5 ml

3.4.4 Hardness tests specimens

The specimens used for hardness testing had the same dimensions as those used for microstructure testing (duplicates were made, one pair for hardness and one pair for microstructure testing). For the hardness test specimens, the same planning process was followed as for the microstructure specimens, but without etching (see Figure 3.4.4).

Figure 3.4.4: Specimens ready for the hardness test.

3.5 List of tests performed

It should be noted that analysis was performed on the processed joints and coal powder reinforcement joints with the purpose of comparing the differences. The following is the list of tests that were conducted:

- Tensile tests
- Bending tests
- Liquid penetrant test (LPT)
- Hardness tests
- Microstructural test
- SEM test

3.6 Mechanical tests

Specimens were cut out from the workpiece sample of the FSWed, FSPed and FSP+Coal plates for the purpose of bending tests, hardness tests, and tensile tests, as well as for microstructure. The specimens were cut from the welded and processed plates in three regions on each plate – start, middle, and end. Three specimens for each test were arranged.
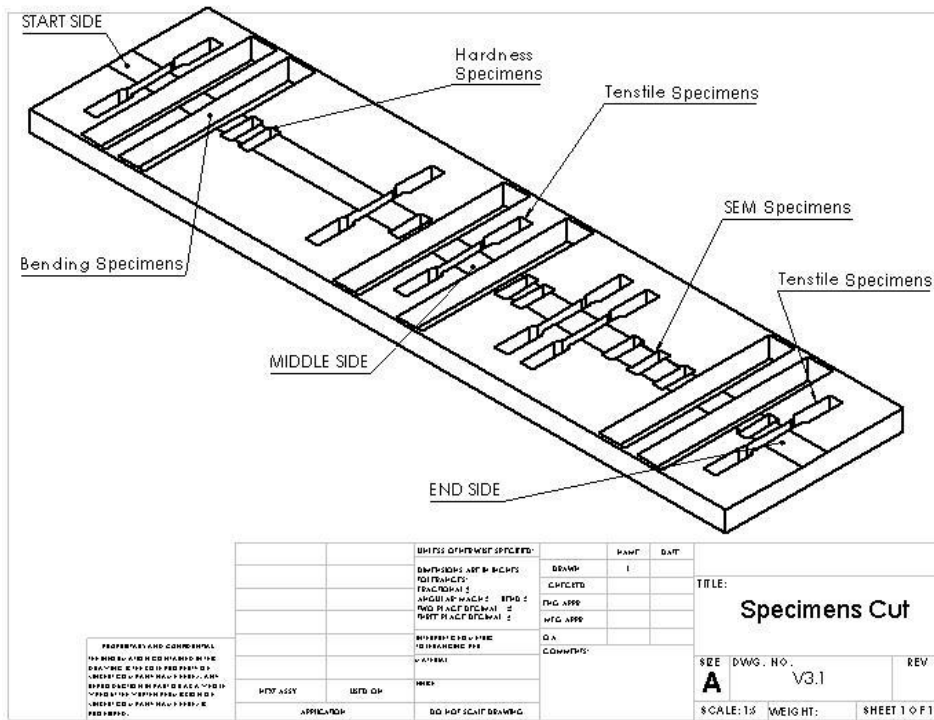
Figure 3.6: Specimens were cut from three regions.

3.6.1 Tensile test

The tensile testing was conducted in order to analyse the yield strength, % elongation, ultimate tensile strength, fracture strain and Young's modulus for FSWed, FSPed and FSP+Coal joints. The Hounsfield 25K tensile testing machine, depicted in Figure 3.6.1(a), uses computers to measure the strength and durability of various materials used in construction and product manufacturing. The tensile test parameters used to perform the tensile testing are presented in Table 3.6.1. This study used the ASTM E8 standard for the tension testing of metallic materials to measure the tensile strength of the samples.

Table 3.6.1: Tensile test parameters.

Speed (mm/min)	Extension range (mm)	Load range (kN)	Load cell (kN)
1	0-10	0-10	50
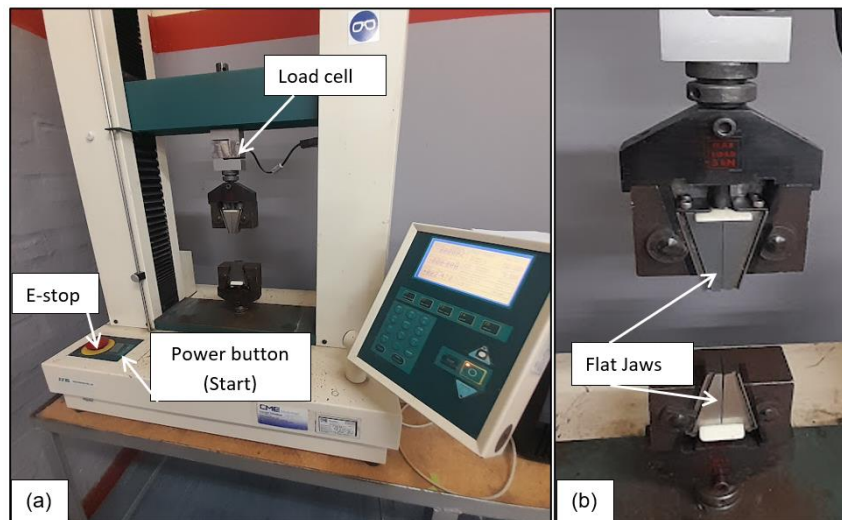
Figure 3.6.1: (a) Hounsfield 25K tensile testing machine (b) Flat jaws to clamp the specimens.

Prior to setting up the specimens in the machine, their dimensions were measured and recorded. The tensile testing process involves placing an object in the jaws of the machine and applying force to determine how it responds to stress and strain. Horizon software was used to log the data, which comprised the applied tensile load and extension. These were later used for the determination of stress and strain. The experiment thus measured the properties of a material by determining Young's modulus, fracture strain, ultimate tensile strength, yield strength, and percentage elongation. A graph of stress versus strain was also created from the data.

The ultimate tensile stress is a measure of the maximum amount of stress a material can tolerate before it breaks. It can be calculated using the formula: Ultimate Tensile Stress = Load Applied / Cross-sectional Area of the Material,

$$\sigma = \frac{F}{A}$$ …………………………………………………………………………………(1)

–where F is the maximum force, σ is the ultimate tensile stress, and A is the cross-sectional area.

The equation used to determine % elongation was:

$$\%E = \frac{Final\ Length - Original\ Length}{original\ Length} \times 100$$ …………………………………………………..…(2)

Elastic Young's modulus was determined using the formula:

$$\varepsilon = \frac{\sigma}{\delta}$$ …………………………………………………………………………………..(3)

–where σ is stress and ε is a strain and δ is deflection.

38

3.6.2 Flexural test

A Hounsfield testing machine with a three-point flexural fixture was used to perform the flexural test, as illustrated in Figure 3.6.2(a). The parameters for the flexural test were the same as for tensile testing. To perform the flexural test one needed first to measure the specimen. Then a centre mark line was drawn in the middle of the joint for alignment with the middle of the indenter. The specimen was placed on rolling supports and aligned with the centre mark line. A loading pin was dropped until it made contact with the top surface of the specimen as shown in Figure 3.6.2(b). The Hounsfield machine controls were zeroed before the start of the test, and the force exerted by the machine was recorded automatically using Horizon. Figure 3.6.2(c) features a close-up of the computer screen as the bending test was in process. The data thus produced shows the performance of a specimen from the start until it failed. The data was recorded using the same process as for the tensile testing. It should be noted that only one specimen was tested at a time.
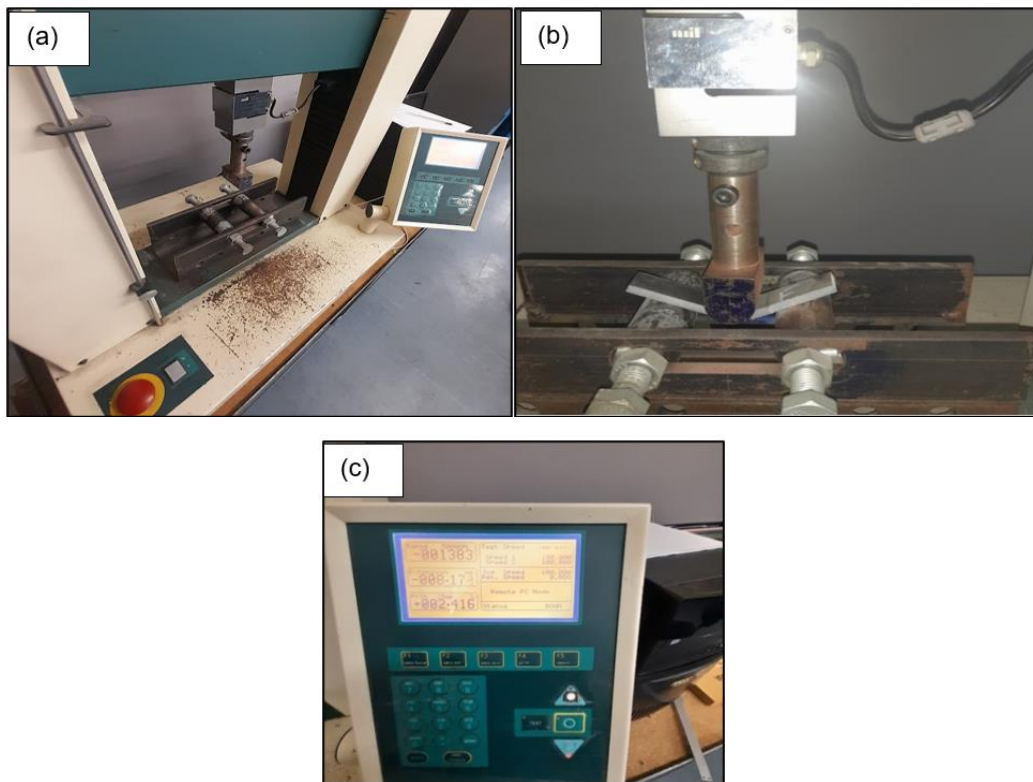
Figure 3.6.2: (a) Hounsfield machine with flexural apparatus; (b) Flexural testing (machine controls); (c) Close-up of the PC screen.

The formula used to decide the maximum stress was as follows:

$$\sigma = \frac{3FL}{2bd^2}$$

.... (4)

Where σ is that the maximum stress, d is the thickness, b is the width of the specimen, L is the length and F is the force. See Figure 3.6.2(d), below, for a diagram representing the flexural test.
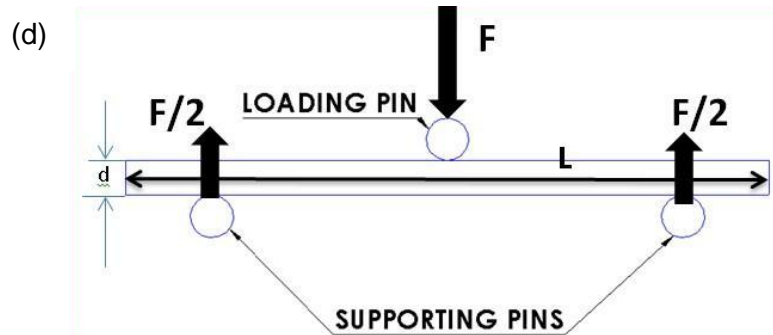
Figure 3.6.2: (d) Diagram of the flexural test.

3.6.3 Liquid penetrant testing (LPT)

Liquid penetrant testing (LPT) presented in Figure 3.6.3 is a non-destructive method of detecting surface-breaking defects in materials. It works by applying a liquid dye to the surface of the material, which penetrates any defects. A contrasting developer is then applied, which highlights the penetrated dye and renders the defects visible. LPT is a cost-effective method of testing and is used in many industries, including the automotive and aerospace, to ensure quality control of the products.

Figure 3.6.3: Liquid penetrant 3-step spray cans.

3.6.4 Hardness tester

Figure 3.6.4(a) shows the hardness testing machine used, the InnovaTest Falcon 500. The Falcon 500 is a testing system designed to help with Micro and Macro Vickers, Knoop, and Brinell assignments. It offers a wide range of test force configurations and integrated hardware options to meet the testing needs of a variety of industries. It has a motorised ball bearing Z-axis for accurate height movement and high speed autofocus, as well as a user interface with manual and automatic measurement. It also includes a high-resolution camera and an optional second camera. The hardness tests were performed to define the bulk hardness of the AA5083/AA6082 welded and processed joints, with and without the coal reinforcement. The test was performed using the Vickers hardness testing scale.
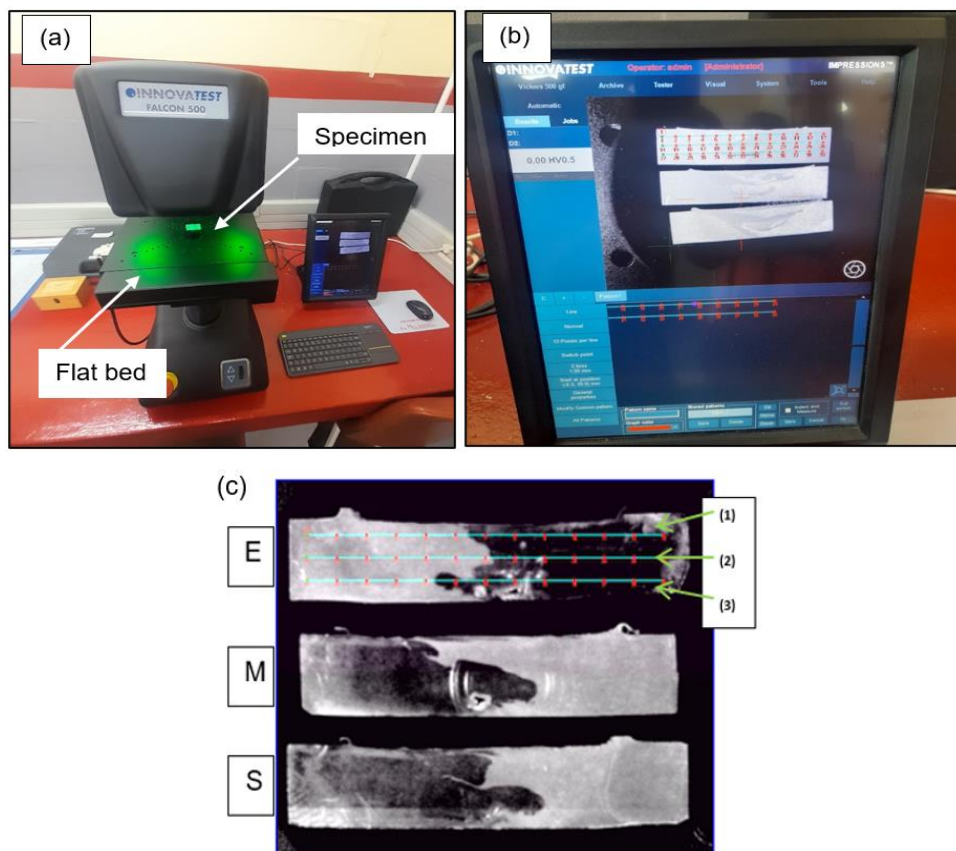
Figure 3.6.4: (a) InnovaTest FALCON 500 Hardness machine; (b) LCD screen of the camera, and; (c) Line depths used.

The ASTM E384-11 standard was used to perform the hardness testing [54]. The specimen was placed on the machine flat stand. The stand was then adjusted upwards until the indenter came into contact with the top surface of the specimen. The pattern settings were set as displayed in Figure 3.6.4(b), with 1 mm distance between the points. Three specimens were tested and indents were taken, as portrayed in Figure 3.6.4(c). The load was set at 0.3 kg. The 10x and 20x objectives were focused. A snapshot of the specimen was taken using the built-in camera of the machine prior to the start of the process. The reset button was pressed, then

the auto run button was pressed to start the process, and the machine began measuring as per the pattern. The data was logged using the Impressions software in the machine, which records automatically from start to finish.

3.6.5 Microstructural tests

The Motic AE2000MET is an Inverted Metallurgical microscope designed to inspect large metal or die-cast parts for failure analysis, material research or quality control. It has advanced infinity optics and anti-reflex coating for superior image quality. It comes with a polariser & analyser for cross polarisation. It can also be used with Moticam for advanced measurement, image processing and documentation reporting. Microstructure analysis was undertaken to investigate the grain sizes and grain structure of the welded and processed joints. The microstructural analysis was performed on the prepared specimen using the AE2000MET with Motic optical microscopy, as shown in Figure 3.6.5. The etched specimen was placed onto the specimen bed with welding joints facing upwards for examination. The specimens were first examined at 5×, 10×, 20×, and 50× to observe features in different microstructure regions. Magnification of 100× was used to observe finer features. The grains were measured following the ASTM E112-13 standard for the linear intercept method through the use of ImageJ software [65].
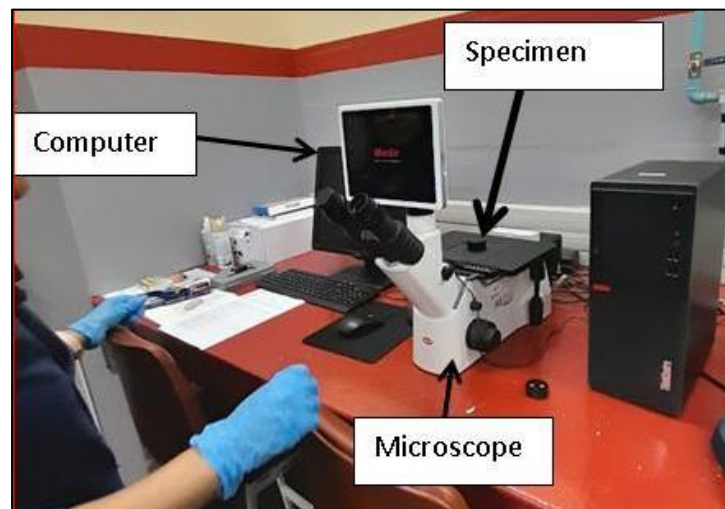
Figure 3.6.5: Motic AE2000MET microscope.

3.6.6 Scanning electron microscopy (SEM) tests

The Nova Nano-SEM 230 scanning electron microscope depicted in Figure 3.6.6(a-d) is a powerful tool for analysing various materials, including metals, nanoparticles, biological samples, and more. It features super large-area energy disperse spectroscopy and electron back-scatter diffraction, which allows for the observation of morphology, the detection of

elemental composition and distribution, and the analysis of structure and orientation. SEM tests were performed using the microstructure specimens and the tensile cut-off specimens. SEM tests for the post-tensile specimens were performed for identification of the nature of the fracture. It should be noted that the SEM test was outsourced to the University of Cape Town Engineering department. The results of all the tests performed are presented in the next chapter.
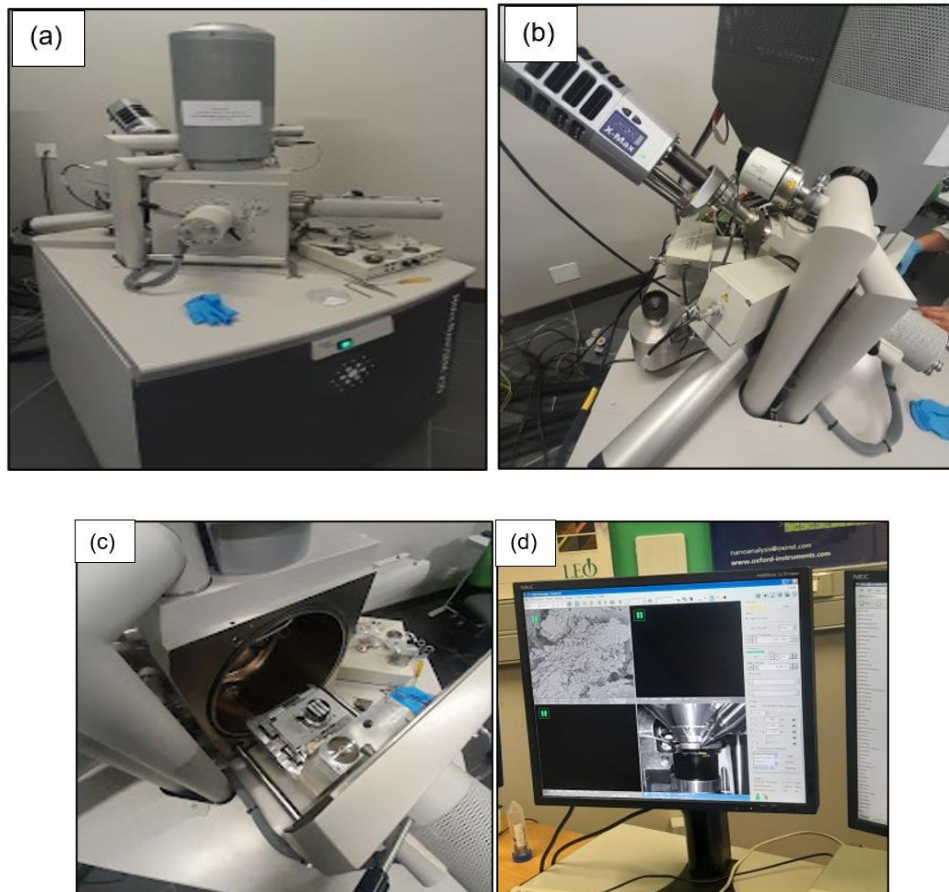
Figure 3.6.6: (a) SEM machine from the front; (b) SEM machine from the rear side; (c) Inside the SEM machine with a sample specimen mount; and (d) SEM machine PC screen.

CHAPTER FOUR

RESULTS AND DISCUSSION

This chapter provides a comprehensive discussion of the results obtained using the processes and methods outlined in Chapter Three. The results include the findings from the flexural test, the tensile test, hardness measurements, microstructure analysis, and scanning electron microscopy.

4.1 Macrostructure

Figure 4.1 presents the macrographs of the FSWed, FSPed, and FSP+Coal joints, which each reveal distinct characteristics. In the case of FSWed joints, the initial macrographs displayed small visible defects, the middle and end specimens exhibiting a tunnel defect, identified by a yellow circle in Figures 4.1(a-c). This tunnel defect can be attributed to insufficient heat and material flow during the early stages of joint formation [66-68]. Moreover, the combination of dissimilar alloys with different melting points led to a disparity in behaviour, with the AA6082 alloy melting and softening more rapidly than the higher-strength AA5083 alloy. Consequently, rapid heat dissipation and cold, hard welds formed in the immediate deformation zone, as evident in Figures 4.1(d-f) [69-71].

The FSPed samples also showed tunnel defects, for similar reasons. The FSP process involves processing dissimilar alloys, and the difference in melting points affects the material flow and joint integrity. Figures 4.1(d-f) provide visual evidence of these tunnel defects. Figures 4.1(g-i) showcase the behaviour of the FSP+Coal joint at different stages. The initial specimen (start) showed no defects, indicating a well-mixed region where the AA6082 alloy integrated smoothly with AA5083. However, as the processing continued, a tunnel defect appeared in the nugget zone (NZ) of the middle specimen, while the end specimen displayed a small defect in the same area.

For clarity, the microstructural zones in the macrographs are identified by red markings, with "1" representing the base metal (AA5083 and AA6082), "2" indicating the heat-affected zone, "3" denoting the thermo-mechanically affected zone, and "4" representing the NZ. These microstructural pictures help us to understand the different regions and their corresponding properties within the joints.
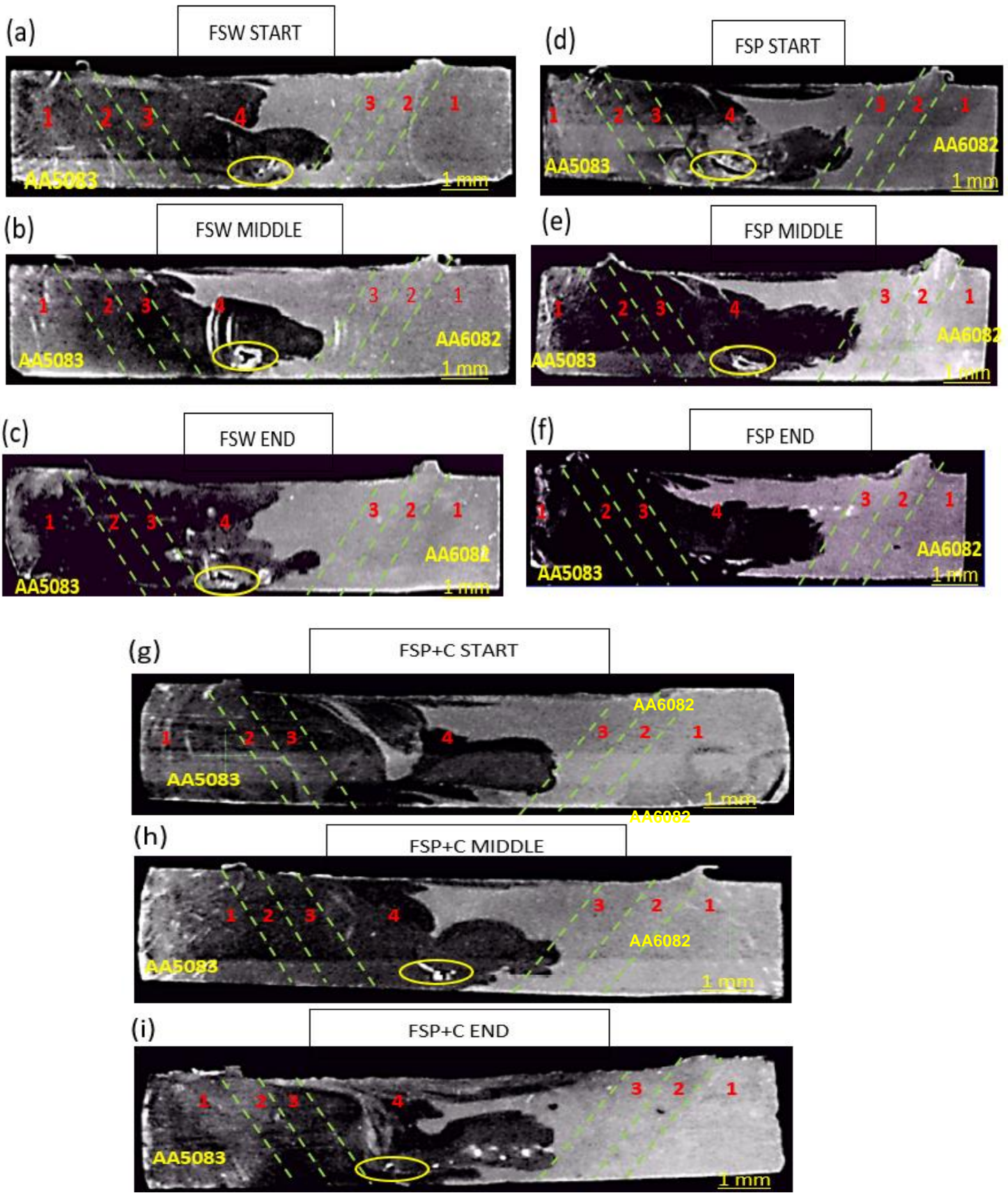
Figure 4.1: Macrographs: FSW joints: (a) Start, (b) Middle, and(c) End; FSP joints: (d) Start, (e) Middle, and (f) End; FSP+Coal joints:Macrographs: (g) Start, (h) Middle, and (i) End.

45

4.2 Microstructure

Metallographic tests were performed on transverse cross-sections of various welded samples to analyse their microstructure. Figure 4.2.1(a-b) displays the microstructures of the parent materials (PM). It can be observed that AA5083 shown in Figure 4.2.1(a) exhibited uniform and relatively coarse grain sizes along and across the rolling direction, ranging from 264 μm to 260 μm. In contrast, AA6082 in Figure 4.2.1(b) displayed an average grain size of 904 μm along the rolling direction and only 217 μm across the rolling direction, thus exhibiting columnar grains. Dark spots of intermetallic particles were also found in both AA6082 and AA5083 parent materials and the rest of the other samples, the dark spots particles of (Fe, Mn)3SiAl2. Notably, Figure 4.2.1 shows that significant microstructural changes occurred after FSW, FSP, and FSP+Coal processes, with the nugget zone consisting of equiaxed fine grains.

The micrographs presented in Figures 4.2.1(c-k) were specifically captured from the NZ of the FSWed, FSPed, and FSP+Coal welded joints at different specimen locations and positions. Table 4.2 presents the microstructure properties with respect to Figures 4.2.1(c-k), while grain distribution diagrams of the same specimens are depicted in Figure 4.2.2. In Figure 4.2.2 it shows a bar graph of the sample count for each welded section eg, AA6082 BM and AA5083 BM and also the "Start"," Middle" and "end" or FSW, FSP and FSP+C. this give a better understanding on the average grain sizes. Table 4.2 show the Mean grain size (μm) of all the welded joints and also the Standard deviation (μm). The FSWed joints displayed a fully recrystallised grain structure with distinct boundary layers, leading to a substantial reduction in pores in comparison to the PM. In contrast, the processed FSPed grain structure exhibited finer grains than the processed FSWed grain structure in Figure 4.2.1(c-e) vs. (f-h). This grain refinement in the FSPed specimens can be attributed to the intense plastic deformation of the metal caused by the rotating tool in the NZ, resulting in the breaking of all micro-constituents and partial recrystallisation [72-74]. Moreover, the grain refinement in FSP+Coal joints was slightly more pronounced than that in the other FSWed and FSPed specimens, as evident in Figure 4.2.1(i-k) and Table 4.2:

A summary of the average grain sizes is presented in Figure 4.2.3. From the figure, it is evident that the post-FSP grains were considerably more refined than they were in the FSWed joints for both conditions. The combination of high plastic deformation and localised heating in FSP creates a more intense and effective grain refinement process, leading to a finer and more homogeneous microstructure than is the case with FSW joints. The refined grain structure contributes to improved mechanical properties, including increased strength and ductility, making FSP an attractive option for enhancing the material's performance in various industrial applications [75-78].

(a) AA5083 Parent material — 20x 100μm

(b) AA6082 Parent material — 20x 100μm

(c) FSW NZ (S) — 20x 100μm

(d) FSW NZ (M) — 20x 100μm

(e) FSW AT NZ (E) — 20x 100μm

(f) FSP AT NZ (S) — 20x 100μm

(g) FSP at NZ (M) — 20x 100μm

(h) FSP at NZ (E) — 20x 100μm
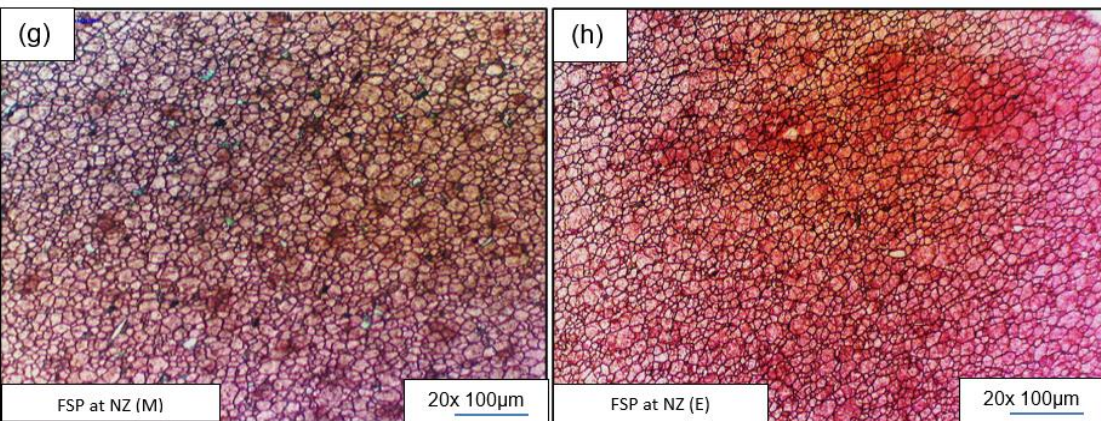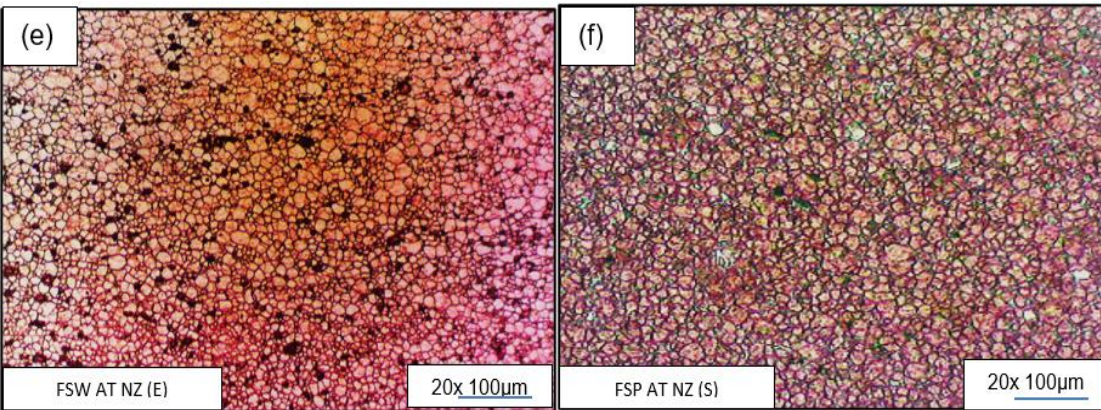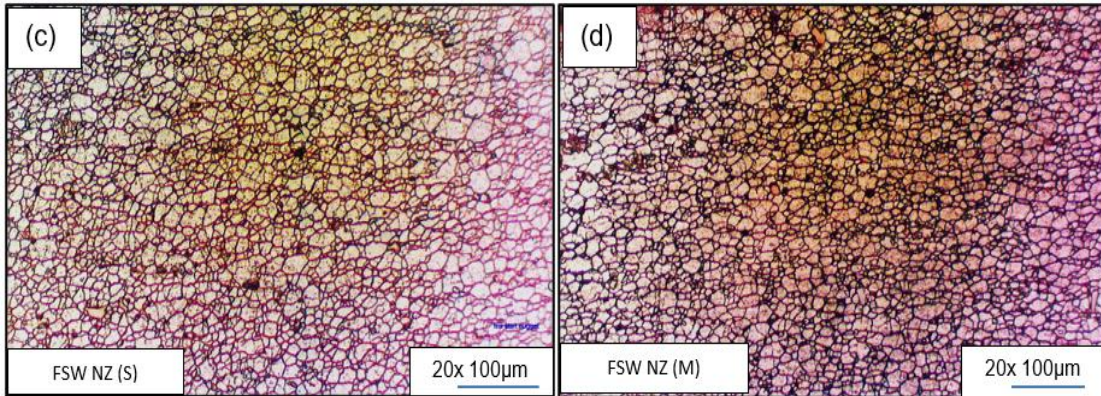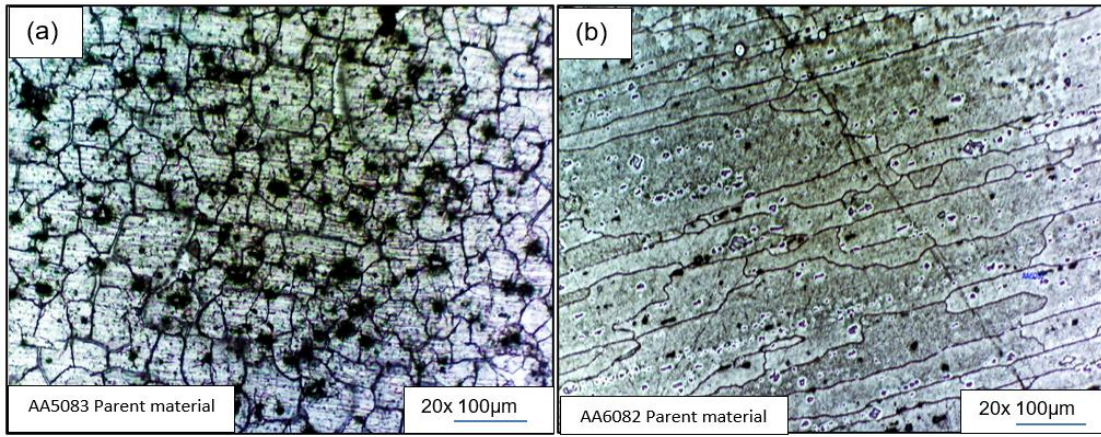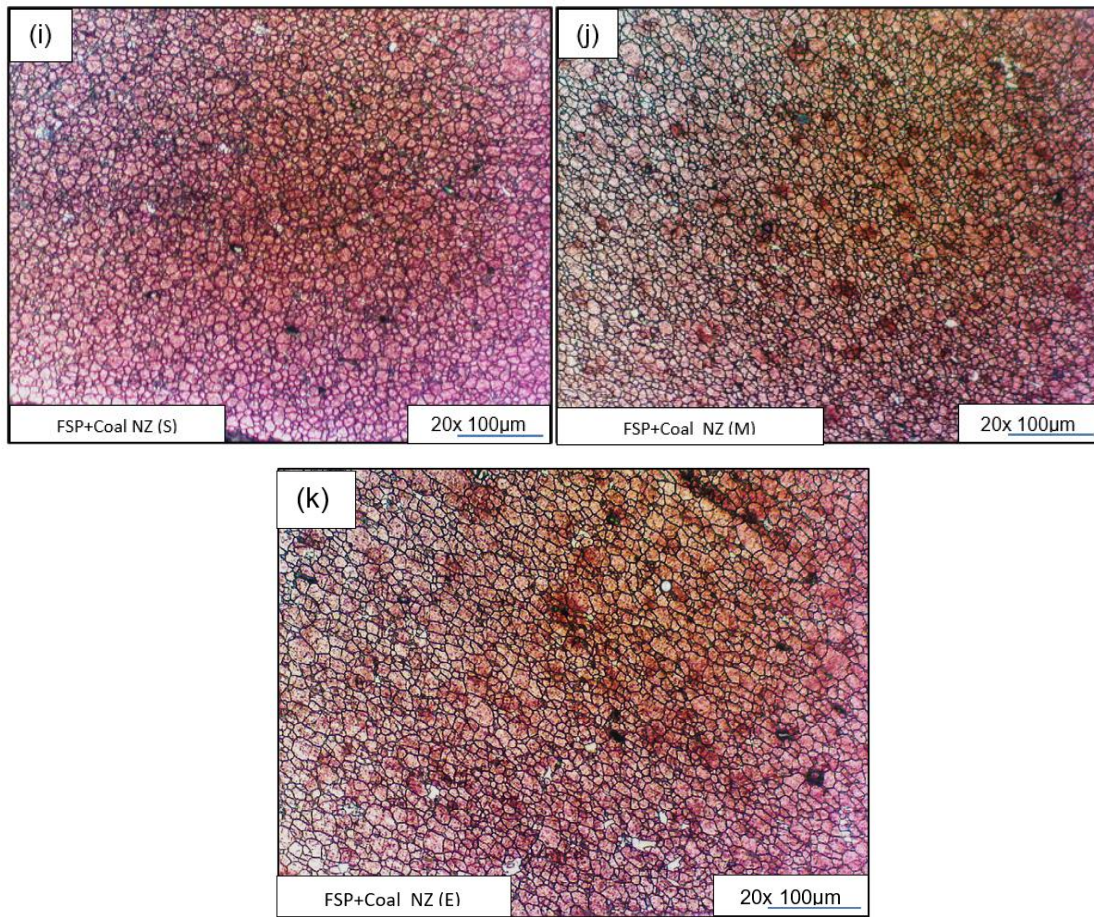
Figure 4.2.1: Optical micrographs at objective 20× and at 100 micros, Parent material: (a) AA5083, (b) AA6082; FSWed at NZ joints: (c) Start, (d) Middle, and (e) End; FSPed at NZ joints: (f) Start, (g) Middle, and (h) End; FSP+Coal at NZ joints: (i) Start, (j) Middle, and (k) End.

Table 4.2: Grain sizes and standard deviations for the SZ.

Welded joint	Mean grain size (µm)	Minimum grain size (µm)	Maximum grain size (µm)	Standard deviation (µm)
AA5083 parent material	302	114	530	94.6
AA6082 parent material	956	130.23	4603.4	982.54
FSW at NZ				
FSW (S)	21.48	10.88	20.52	4.89
FSW (M)	19.35	9.74	18.86	4.32
FSW (E)	18.26	12.19	18.12	3.77
FSP at NZ				
FSP (S)	10.81	3.23	11.25	2.42
FSP (M)	9.03	5.48	9.43	1.43
FSP (E)	9.04	3.11	9.08	2.63
FSP+Coal at NZ				

FSP+Coal (S)	9.55	5.34	9.52	1.62
FSP+Coal (M)	8.33	3.98	8.48	1.68
FSP+Coal (E)	8.34	5.15	8.49	1.265
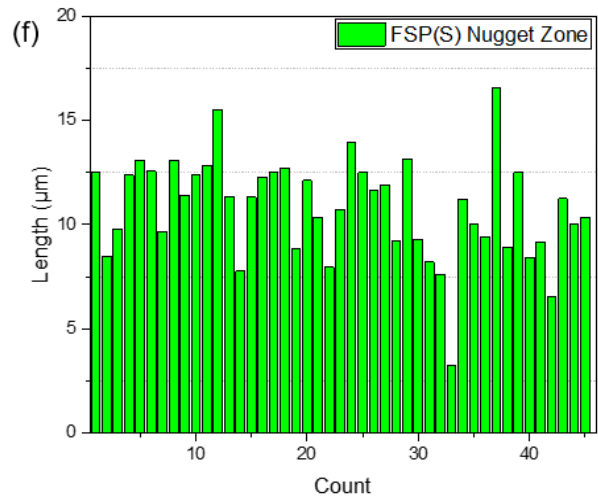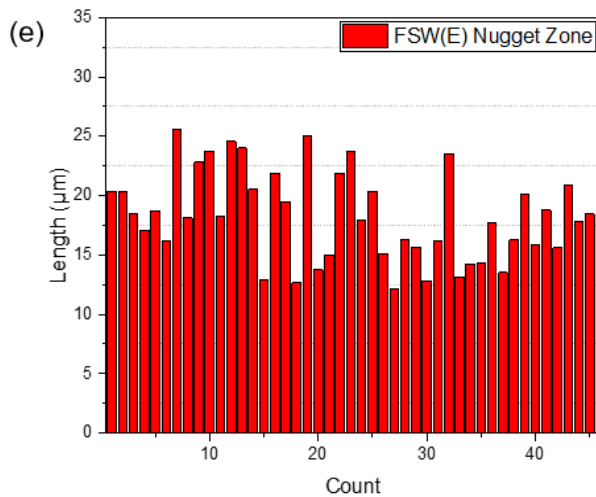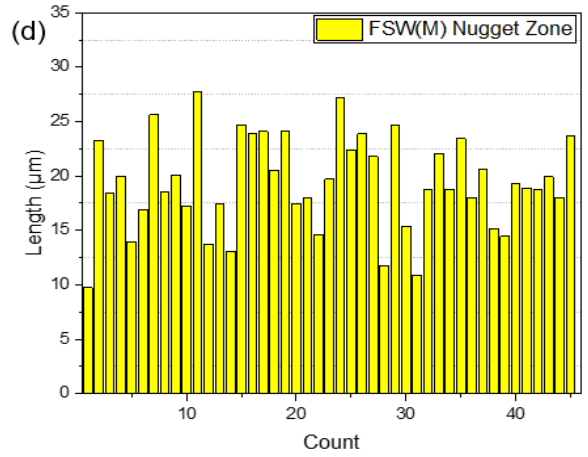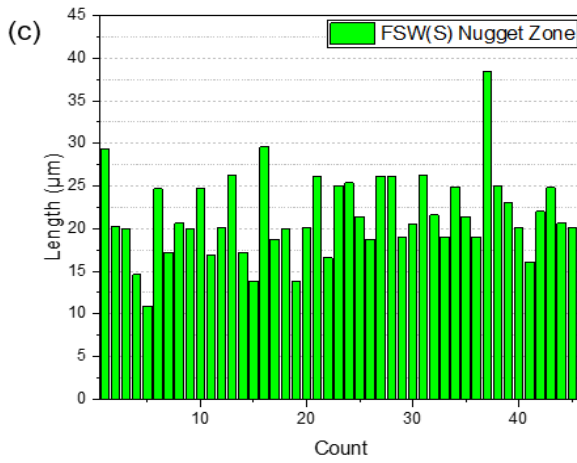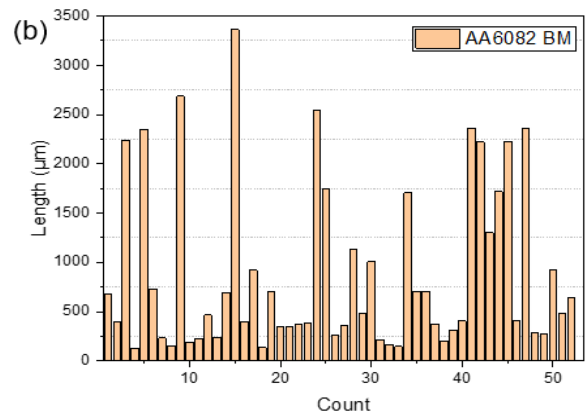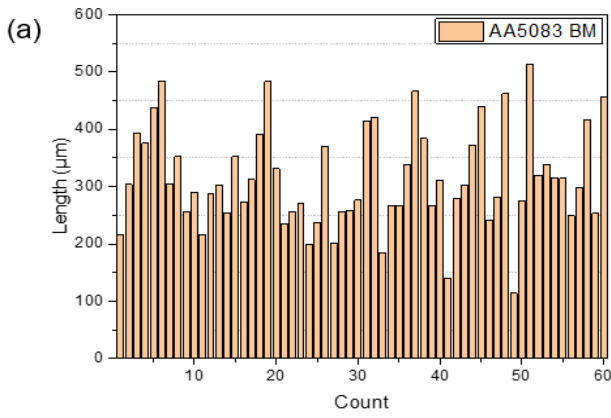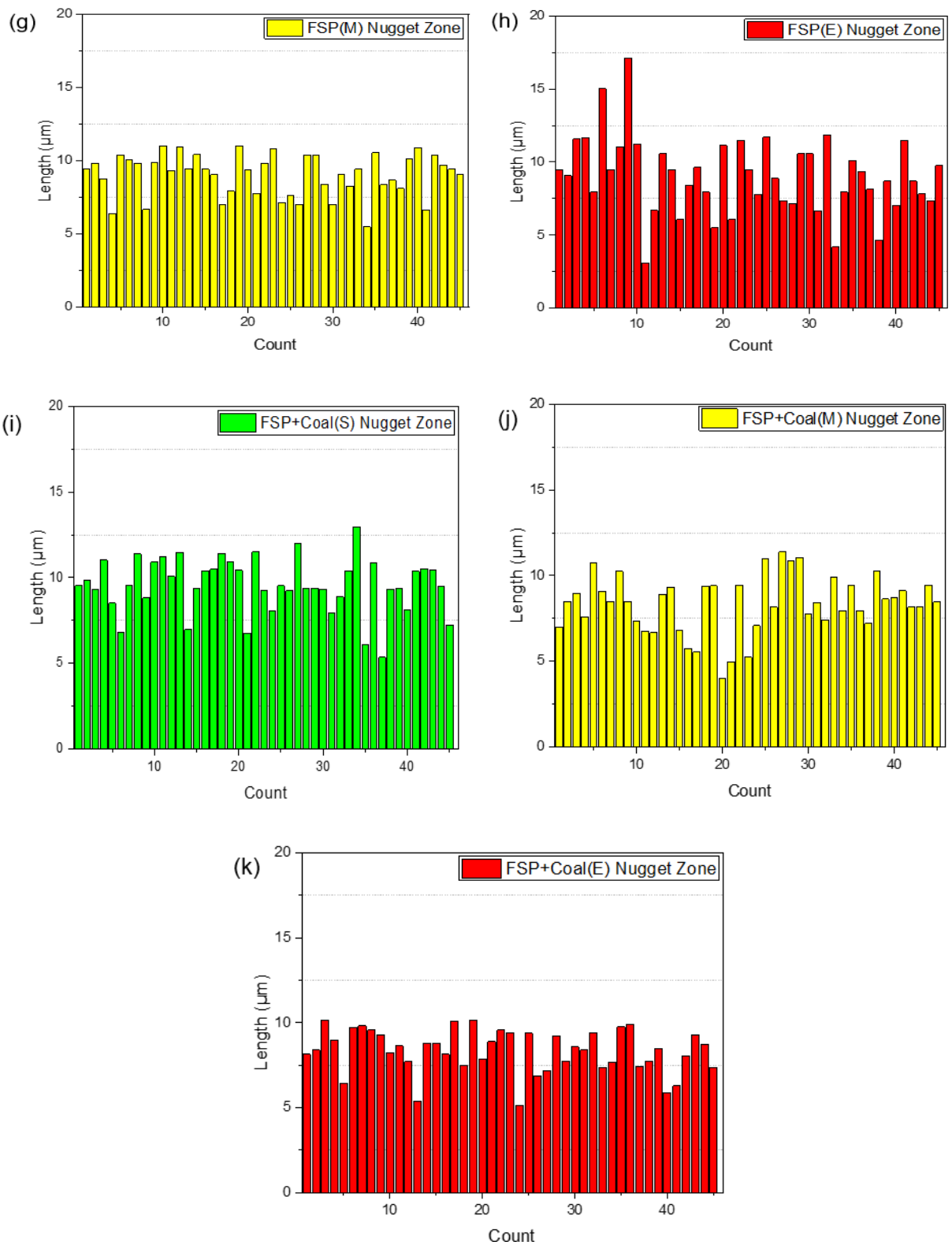
Figure 4.2.2: Grain distribution bar graphs grain size: (a) BM AA5083: (b) BM AA6082: FSW grains: (c) Start, (d) Middle, and (e) End; FSP grains: (f) Start, (g) Middle, and (h) End; FSP+Coal grains: (i) Start, (j) Middle, and (k) End.
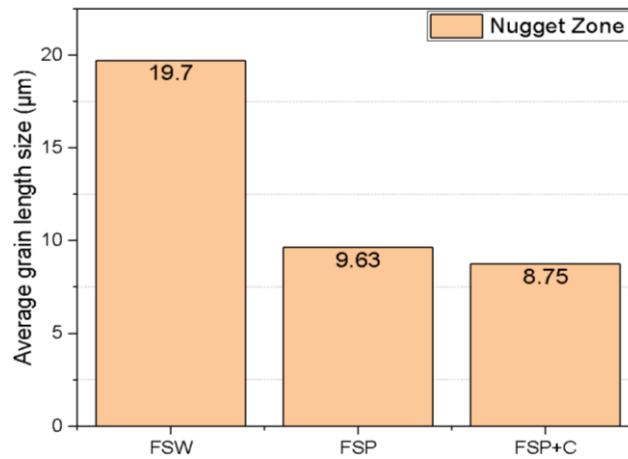
Figure 4.2.3: Average grain sizes.

4.3 Flexural tests results

Flexural testing was applied to both sides of the joint, i.e., the face and the root of each specimen. The face of the specimen is the surface that was in contact with the tool during welding, while the root is the surface that was in contact with the welding machine bed.

Liquid Penetrant Testing (LPT), a form of Non-Destructive Testing (NDT), was performed on the bent specimens to detect any potential defects on their surfaces after the flexural test. Figures 4.3.1 (a-c) illustrate the step-by-step process involved in LPT. As shown in Figure 4.3.1(a), it was crucial to verify the presence of cracks that might have developed during bending. The surfaces were carefully cleaned using Spanjaard Cleaner No: 1 Aerosol solvent cleaner and an absorbent cloth until no further contamination was visible on the cloth. After allowing the surfaces to dry for three minutes, they were treated with Penetrant No: 2, as demonstrated in Figure 4.3.1(b). A dwell time of 5 minutes was given for the penetrant to seep into any potential defects. Subsequently, Spanjaard Cleaner No: 1 Aerosol was used to remove the penetrant from the surfaces. In Figure 4.3.1(c), Spanjaard Developer No: 3 was applied to the surfaces, encouraging capillary action. This developer was left on for 10 minutes before cleaning to expose any defects that might have been present. Table 4.3.1 shows the joint identification of the FSWed, FSPed, and FSP+Coal flexural joints.
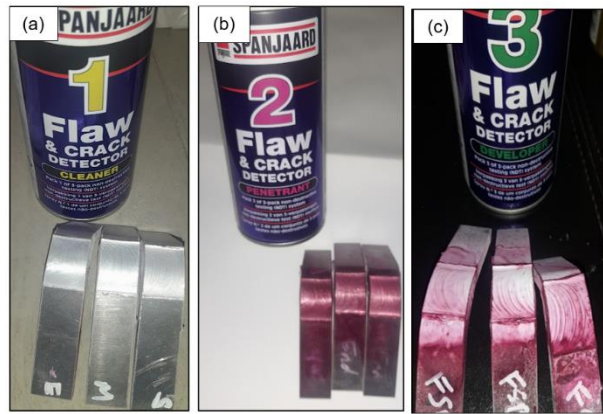
Figure 4.3.1(a-c): Liquid penetrant applied on face weld joints.

Table 4.3.1(a): FSW flexural joint identification.

Joint identification	Photographs of the bends at 1 mm magnification.	Defects and possible cause
FSW Root S		Root weld has a crack where AA5083's advancing side thermomechanical affected zone (TMAZ) of the weld. The crack is attributed to a thin layer that was not penetrated by the tool to avoid tool pin rubbing on the back plate.
FSW Root M		Root weld has a crack middle of the weld 90deg bend. The crack is attributed to a thin layer that was not penetrated by the tool to avoid tool pin rubbing on the back plate.
FSW Root E		Root weld has a crack middle of the weld. The crack is attributed to a thin layer that was not penetrated by the tool to avoid tool pin rubbing on the back plate.

Joint identification	Photographs of the bends at 1 mm magnification.	Defects and possible cause
FSW Face S	AA5083 AA6082 AA5083	Face weld: no defect observed where AA6082 was on the bending end of the weld.
FSW Face M	AA5083 AA6082	Face weld: no defect observed where AA6082 was on the bending end of the weld.
FSW Face E	AA5083 AA6082	Face weld: the only one that had a tiny defect – a crack at the edge of the TMAZ where AA6082 was on the bending end of the weld.

Table 4.3.1(b): FSP flexural joint identification.

Joint identification	Photographs of the bends at 1 mm magnification.	Defects and possible cause
FSP Root S	AA5083 AA6082	Root weld has a crack on the middle of the weld. Crack is attributed to a thin layer that was not penetrated by the tool to avoid tool pin rubbing on the back plate.
FSP Root M	AA5083 AA6082	Root weld has a partial thin hairline crack on the end of the weld. The bending was more on the AA6082 HAZ side. The crack is attributed to some portions of a thin layer that was not penetrated by the tool. Rubbing of the tool pin on the back plate is observable from the wavy patterns on the surface.

Joint identification	Photographs of the bends at 1 mm magnification.	Defects and possible cause
FSP Root E	AA5083 / AA6082	Root weld has a crack on the middle of the weld. The bending was more on the AA6082 HAZ side. The crack was on the TMAZ side, it is attributed to a thin layer that was not penetrated by the tool to avoid tool pin rubbing on the back plate.
FSP Face S	AA5083 / AA6082 / AA5083	Face weld: no defect observed where AA6082 is bending at the start of the weld.
FSP Face M	AA6082 / AA5083	Face weld: no defect observed where AA6082 is bending at the start of the weld.
FSP Face E	AA5083 / AA6082 / AA5083	Face welds: no defect observed where AA6082 is bending at the start of the weld.
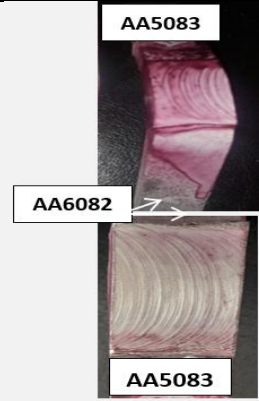
Table 4.3.1(c): FSP+Coal flexural joint identification.

Joint identification	Photographs of the bends at 1 mm magnification.	Defects and possible cause
FSP+Coal Root S	AA5083 / AA6082	Root weld has a crack on the middle of the weld. The crack is attributed to a thin layer that was not penetrated by the tool to avoid tool pin rubbing on the back plate.

FSP+Coal Root M			Root weld has a crack on the middle of the weld. The crack is attributed to a thin layer not penetrated by the tool to avoid tool pin rubbing on the back plate
FSP+Coal Root E			Root weld has a crack where AA5083 is on the advancing side (AS) of the weld. The crack is attributed to a thin layer not penetrated by the tool to avoid tool pin rubbing on the back plate.
FSP+Coal Face S			Material has lumpiness on the surface. Plastic deformation caused boundary grain dislocation. The weld is cracked half-way at the AA5083 weld-end TMAZ, which might be a defect caused by the coal powder not being mixed correctly.
FSP+Coal Face M			Material has lumpiness on the surface. Plastic deformation caused boundary grain dislocation. The weld is cracked half-way at the AA5083 weld-end TMAZ.
FSP+Coal Face E			Material has lumpiness on the surface. Plastic deformation caused boundary grain dislocation. The weld is cracked fully across the AA5083 weld-end TMAZ.

Figure 4.3.2(a-f) feature the specimens after the bending test. The FSW and FSP face weld specimens flexed towards the AA6082 side, which is the weaker strength alloy. This suggests that the FSW and FSP face weld joints had a stronger joint strength than the AA6082 base material. This phenomenon is consistent with previous findings in the literature [79]. No cracks were observed on the post-face specimens except for FSW E face weld, which had a small defect crack at the edge of the thermo-mechanically affected zone (TMAZ) where the AA6082

bending end of the weld was located. On the other hand, the root weld specimens all cracked near or in the middle of the root weld. FSP+Coal face weld specimens had cracks exclusively on the AA5083 TMAZ side, which could be attributed to the presence of coal powder dominating the joint.
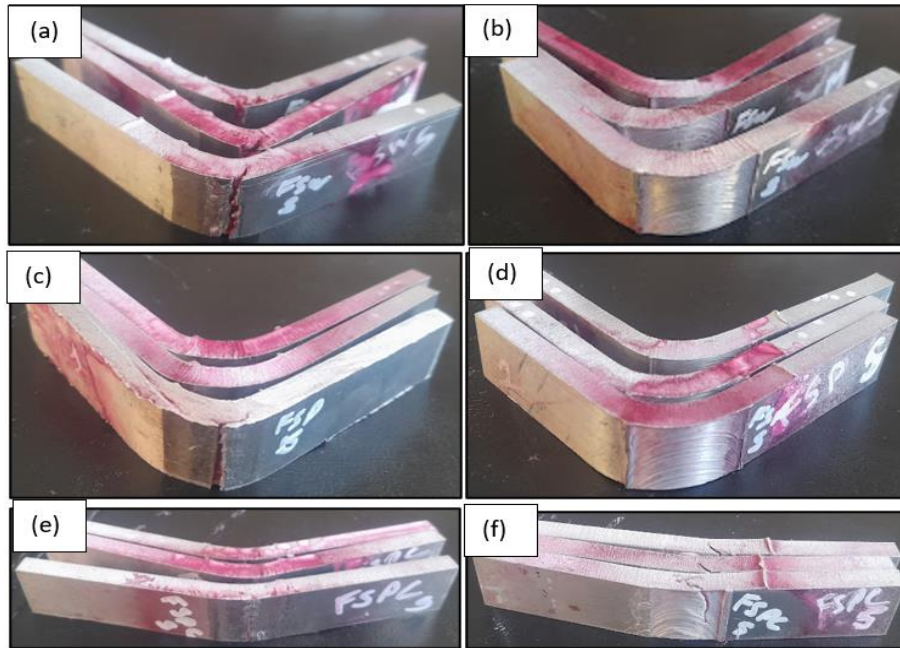
Figure 4.3.2(a-f): displays the specimens after the flexural test. (a)FSW Root, (b) FSW Face, (c) FSP Root, (d) FSP Face, (e) FSP+Coal Root, (f) FSP+Coal Face.

Figure 4.3.3(a, c, e) and Figure 4.3.3(b, d, f) present the results of the flexural tests conducted on the root and face of the FSWed, FSPed, and FSP+Coal joints. A corresponding summary of the flexural result is presented in Table 4.3.2. It is essential to emphasise that all specimens were bent until failure, which explains the projectile shape evident in the graphs. The root flexural test outcomes indicate that the FSWed specimens failed at a maximum strain of 12.67% with a flexural stress of 571MPa. Similarly, the FSPed root specimens failed at a maximum strain of 12.9% and a flexural stress of 581 MPa, while the FSP+Coal root specimens failed at a maximum strain of 6.2% with a flexural stress of 422 MPa. The face flexural test revealed different results: the FSWed specimens failed at a maximum strain of 12.7% with a flexural stress of 535 MPa. In contrast, the FSP specimens failed at a maximum strain of 10.81% with a flexural stress of 545.6 MPa, and the FSP+Coal specimens failed at a maximum strain of 3% with a flexural stress of 222 MPa. The six graphs clearly highlight the distinctions between the face and root flexural tests for the FSWed, FSPed, and FSP+Coal specimens.

The data therefore shows that the flexural strength of the friction stir welded (FSWed) joint is higher than that of the friction stir processed (FSPed) and friction stir processed

reinforced with coal (FSP+Coa)l joints. Several factors contribute to this difference, including the microstructure and defects. In the case of FSP+Coal joints, the distribution of coal particles within the joint might not have been uniform, resulting in variations in mechanical properties. Non-uniform reinforcement distribution can result in localised weak points, reducing the overall bending strength [80-83].
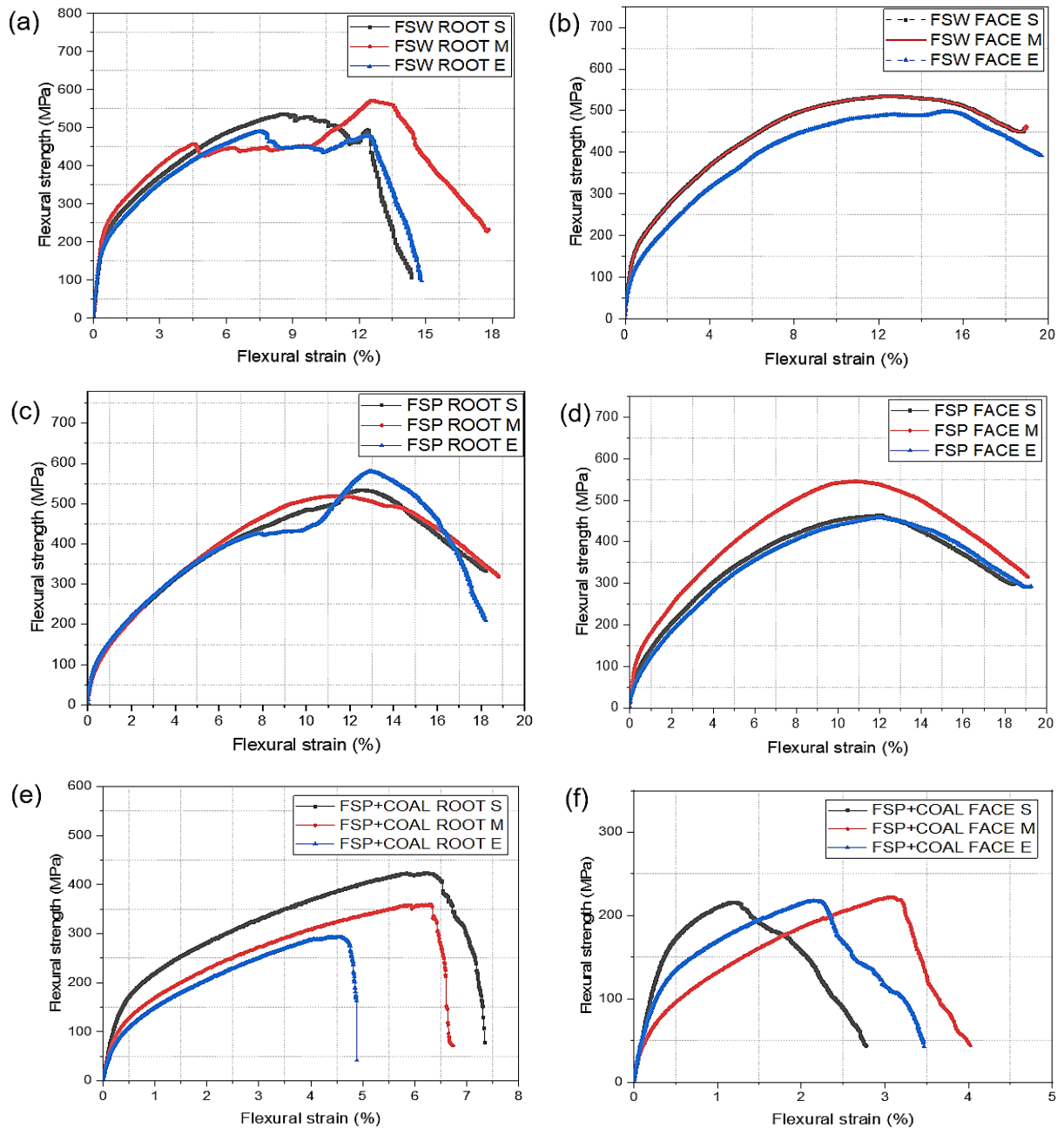
Figure 4.3.3: Flexural stress-strain curves: (a) FSWed joints AA6082/AA5083; (b) FSP joints AA68082/AA5083; (c) FSP+Coal AA6082/AA5083 joints.

Table 4.3.2: Root and Face flexural results.

Sample	Maximum Force	Fracture Point	Flexural Stress (MPa)	Post specimen
		Face		
FSW S	1902N, at 17.2mm	1640N, at 25.6mm	534.94	No defect
FSW M	1901N, at 17mm	1815N, at 26.3mm	534.97	No defect
FSW E	1772N, at 20.4mm	1393N, at 26.6mm	498.38	Defect tiny crack on edge of weld
FSP S	1648N, at 16.2mm	1072N, at 25.1mm	463.5	No defect
FSP M	1940N, at 14.7mm	1122N, at 25.8mm	545.63	No defect
FSP E	1632N, at 16.2mm	1042N, at 26mm	459	No defect
FSP+Coal S	768N, at 1.66mm	155N, at 3.75mm	216	Cracked
FSP+Coal M	790N, at 4.17mm	157N, at 5.43mm	222.19	Cracked
FSP+Coal E	775N, at 2.9mm	153N, at 4.68mm	217.97	Cracked
		Root		
FSW S	1903N, at 11.5mm	380N, at 19.4m	535.22	Cracked
FSW M	2030N, at 16.9mm	825N, at 24.1mm	518.34	Cracked
FSW E	1745N, at 10.3mm	348N, at 20mm	490.78	Cracked
FSP S	1897N, at 16.8mm	1180N, at 24.6mm	533.53	Cracked
FSP M	1845N, at 15mm	1130N, at 25.4mm	518.91	Tiny hairline crack
FSP E	2066N, at 17.5mm	742N, at 24.6mm	581.06	Cracked
FSP+Coal S	1503N, at 7.9mm	275N, at 9.92mm	422.72	Cracked
FSP+Coal M	1277N, at 8.47mm	255N, at 9.1mm	359.16	Cracked
FSP+Coal E	1042N, at 6.16mm	147N, at 6.6mm	293	Cracked

4.4 Tensile properties

This section presents the results obtained from the tensile testing machine using the same specimen format as described in Section 4.1. The data collected was used to determine the ultimate tensile stress (UTS) and percentage elongation of the specimens, which were calculated using equations (1) and (2), respectively.

Figure 4.4.1 displays the processed specimens of three different joint types, FSWed, FSPed and FSP+Coal. These specimens were subjected to a tensile test to evaluate their mechanical properties and behaviour under tension. In the case of FSWed and FSPed specimens, the failures were observed outside the welded area, specifically in the HAZ of the AA6082 side. This fracture pattern indicates a seamless joint, with the joint itself remaining intact during the test [58]. Additionally, both FSWed and FSPed joints exhibited stronger characteristics than the base material, AA6082. The HAZ, however, demonstrated the weakest

strength when compared to both the nugget zone (NZ) and the AA6082 side of the specimen [59, 49], which is a common phenomenon when dissimilar materials are joined together.

Notably, all the specimens joined using FSW and FSP methods fractured at the HAZ, highlighting that the tensile strength of the NZ was superior to that of the AA6082 alloy [79-80]. That is, the NZ, being the region where the materials are effectively mixed during the joining process, displayed greater resistance to fracture. On the other hand, the FSP+Coal joint exhibited a different failure pattern. The failure occurred within the welding zone area, close to the AA5083 side of the specimen, which appeared brittle in nature. The type of failure observed at the TMAZ indicated a lack of elongation or ductility, signifying a brittle failure [84-85].

This brittle failure in the FSP+Coal joint implies that the coal powder material significantly influenced the joint, leading to failure within the welded area where the coal powder was incorporated as shown in Figure 4.4.1(c). The location of the failure varied between specimens, occurring where the coal powder was present. One notable example is Specimen E, which displayed incomplete fusion between the coal powder and the alloy, potentially contributing to the brittle nature of the joint. Overall, the FSWed and FSPed joints demonstrated seamless characteristics and superior strength compared to the base material, whereas the FSP+Coal joint exhibited brittle failure, influenced significantly by the presence and fusion of the coal powder.
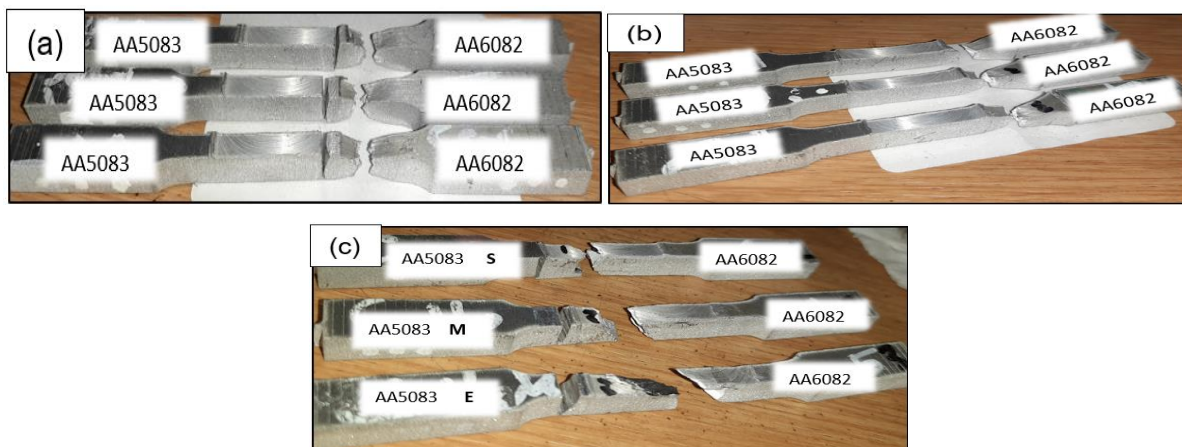
Figure 4.4.1: Post-tensile specimens (a) FSW (b) FSP and (c) FSP+Coal.

In Figure 4.4.2, the tensile stress-strain curves of three different types of joints are presented, namely, those formed through FSW, FSP, and FSP+Coal. The corresponding tensile properties are summarised in Table 4.4.2 according to the data presented in Figure 37. The FSWed joints displayed the highest UTS of 145.9 MPa, occurring at a tensile strain rate of 9.43%. On the other hand, the lowest UTS for FSWed joints was 93.43 MPa, observed at a lower tensile strain rate of 7.02%. Moving to the FSPed joints, they exhibited a maximum UTS of 170.9 MPa at a corresponding tensile strain rate of 9.13%. The minimum UTS for FSPed joints was 126 MPa, occurring at a slightly higher tensile rate of 7.38%.

For the FSP+Coal joints shown in Figure 4.4.2(c), the maximum UTS obtained was 142 MPa, with a corresponding tensile strain rate of 9.28%. The minimum UTS for these joints was 104.06 MPa, observed at a lower tensile rate of 4.63%. The data presented in Figure 4.4.2 and Table 4.4 provide valuable insights into the mechanical behaviour of the joints formed through different processes. The application of FSP on the FSWed joint improved the UTS of the joint. This behaviour is attributed to the grain refinement, homogenisation, residual stress redistribution, precipitation and dispersion, texture modification and the reduction of defects [86-88].

Comparing the FSPed joints with FSP+Coal, the FSPed exhibited the highest UTS while the FSP+Coal joints showed the lowest UTS values. Coal, being less mechanically robust than the base materials, seems not to provide the same level of strength as witnessed in the original FSPed or FSWed joints [87-89]. The integration of coal reinforcement led to voids (as discussed in Section 4.1), inclusions, and possibly weaker bonding at the interface between the reinforcement and the base material, resulting in a reduction in overall joint strength. Thus, that the FSP+Coal joints exhibited lower UTS values than the other joints is not a startling result.
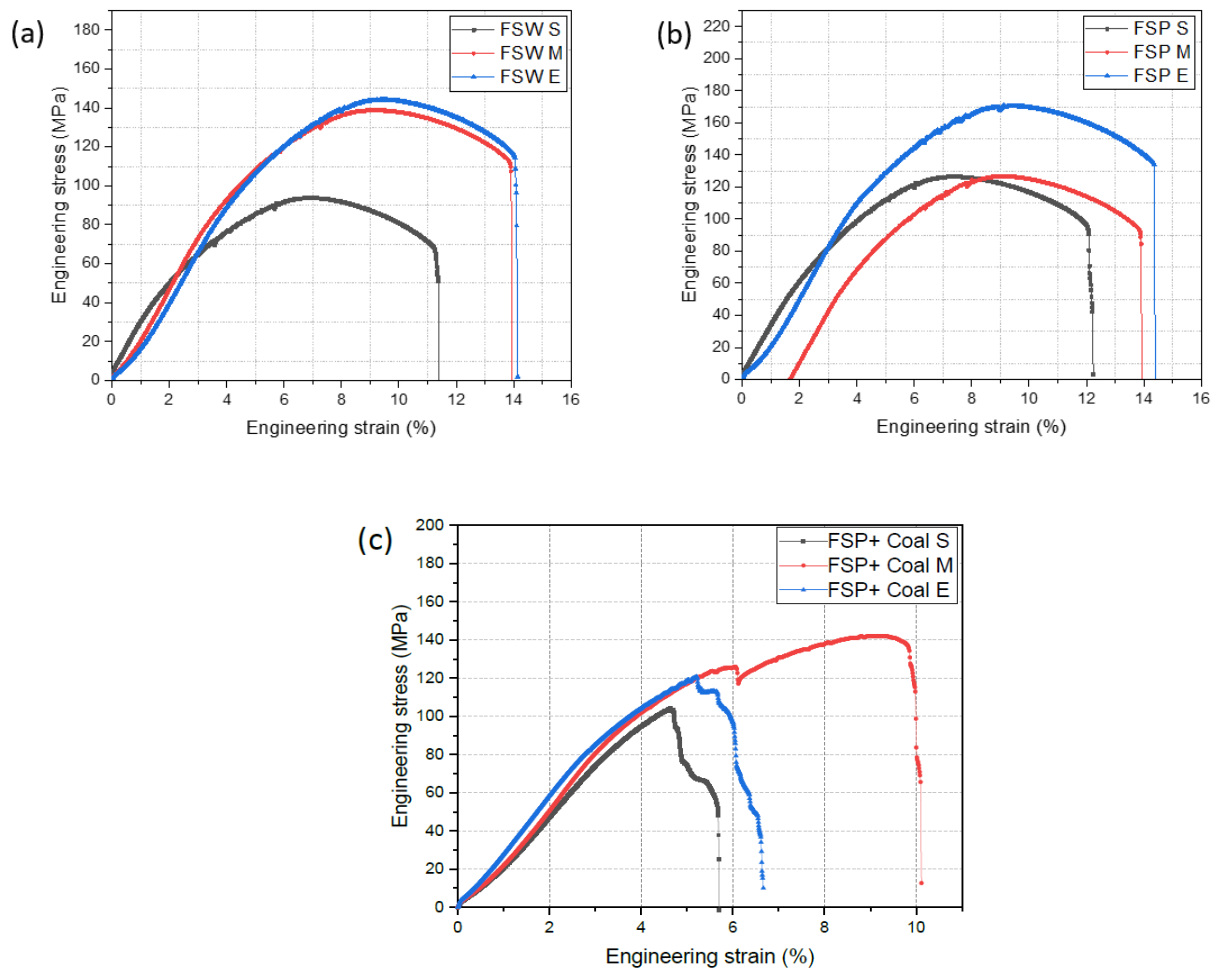
Table 4.4: Summarized tensile properties.

Sample	Ultimate Tensile Stress (MPa)	Tensile strain at UTS (%)	Tensile strain at break point (%)	Position of fracture
FSW S	93.43	7.02	11.3	HAZ/AA5083
FSW M	136.6	9.28	13.9	HAZ/AA6082
FSW E	145.9	9.43	14.1	HAZ AA6082
FSP S	126	7.38	12.2	HAZ/ AA6082
FSP M	126.66	9.14	13.9	HAZ/ AA6082
FSP E	170.9	9.13	14.36	HAZ/ AA6082
FSP+Coal S	104.06	4.63	5.68	TMAZ/ AA5083
FSP+Coal M	142	9.28	10.09	TMAZ/ AA5083
FSP+Coal E	120.63	5.21	6.65	NZ

4.5 Microhardness

Figure 4.5 illustrates the Vickers hardness profiles of the welded joints produced through FSW, FSP and FSP+Coal. Additionally, the nugget zone (NZ) hardness bar charts for these joints are presented. One of the key findings is that AA5083-H111 consistently exhibited higher hardness values than AA6082-T651 in all the tests conducted. This was due to the AA5083-H111 and AA6082-T651 being two different aluminium alloys with distinct compositions. Differences in alloy compositions can lead to variations in their respective mechanical properties, including hardness [90-92]. Also, the "-H111" and "-T651" designations represent different heat treatment conditions. AA5083-H111 is strain-hardened, also known as cold-worked and annealed, to achieve its specific hardness and mechanical properties [93]. In contrast, AA6082-T651 is heat-treated and artificially aged (solution heat-treated and then aged), which results in its hardness characteristics [94-97].

The FSWed, FSPed, and FSP+Coal joints displayed notably greater hardness than AA6082-T651 at the nugget zone, with an average value of 55-75 HV observed throughout the weld positions in FSW depicted in Figure 4.5(a-c). However, moving away from the nugget zone towards AA6082-T651, the hardness values decreased across all the welded joints. Interestingly, the tool shoulder and tool pin positions on the AA5083-H111 edges showed

minimal difference compared to the nugget zones, particularly at the start and middle weld positions. Moreover, at the end of the weld, greater hardness values were observed on the tool shoulder edges than in the nugget zone.

On the AA6082-T651 side, the regions near the tool pin and tool shoulder positions registered relatively lower hardness values than other regions. In contrast, the nugget zone exhibited a significant increase in hardness values along the entire length of the welded joint, surpassing the hardness of the AA6082-T651 HAZ side. This increase in hardness is attributed to the fine grain size generated by the FSW process and the work-hardening effect induced during welding, as previously noted [47]. It is important to remember that the AA6082-T651 alloy is precipitate-hardened, and its properties can be greatly affected by temperatures above 200°C [91-94]. Consequently, the data suggests that the temperature has affected the AA6082 alloy, particularly in the HAZ, in comparison to the AA6082-T651 base material.

Figure 4.5(d-f) presents the results in respect of the FSP joints without reinforcement. Notably, FSP S achieved a maximum hardness of 90 HV at the NZ, while the maximum hardness at the TMAZ was 85 HV, decreasing to 54 HV towards the start of the AA6082-T651 base metal. This observation indicates that the processed joints offer greater resistance to deformation. The hardness behaviour of FSP aligns with that of wrought 5XXX series aluminium alloys, where little change in hardness is observed between the nugget zone and the base material [98-101]. This finding is consistent with the FSW and FSP tensile and flexural strength results presented in Sections 4.3.1 and 4.4.1, suggesting grain size refinement at the processed joint. However, it is important to note that the tensile failure point and flexural face point were on the AA6082-T651 side.

This section next delves into the results of the hardness tests conducted on the FSP+Coal welded joints, as depicted in Figure 4.5(g-i). Interestingly, for all three positions (S, M, and E), the hardness values of AA5083-H111 at the tool shoulder edges exhibited minimal difference from those at the nugget zones. The maximum hardness value in the nugget zone was 84 HV. Additionally, all three welded depth lines were closely grouped together as they progressed from AA5083-H111 through the nugget zone to the AA6082-T651 side, in contrast to the FSW and FSP depth lines. To give a clear presentation of the stir zones of the joints discussed, Figure 4.5(j) provides bar charts to illustrate all the NZ hardness values.

This comprehensive examination of the Vickers hardness profiles of various welded joints sheds light on the differences in hardness values among FSW, FSP, and FSP+Coal joints when these are compared to the base materials AA5083-H111 and AA6082-T651. The results emphasise the significance of joint processing techniques in influencing hardness values, grain size, and mechanical properties.
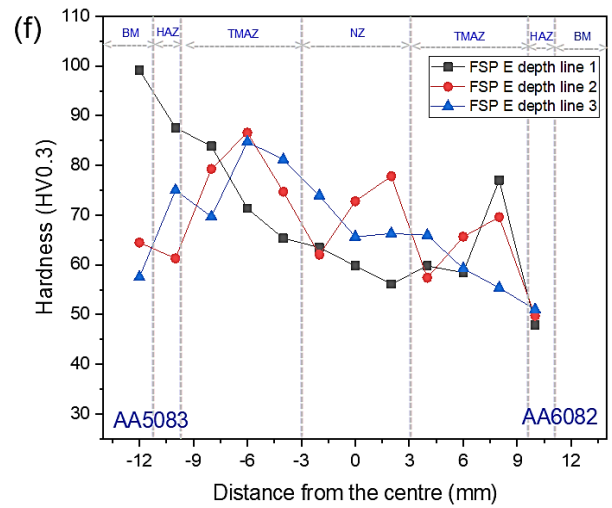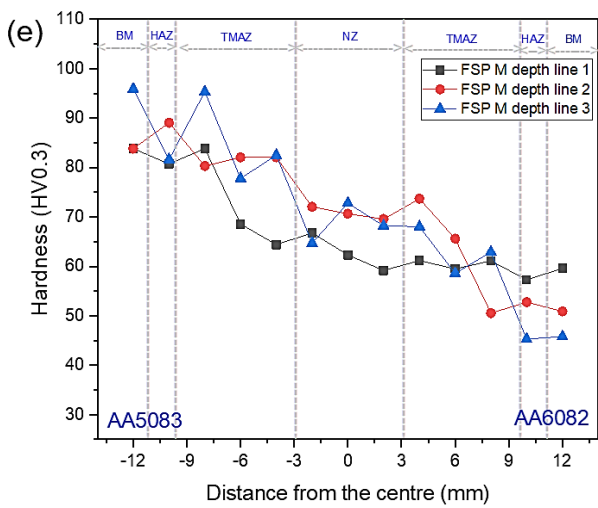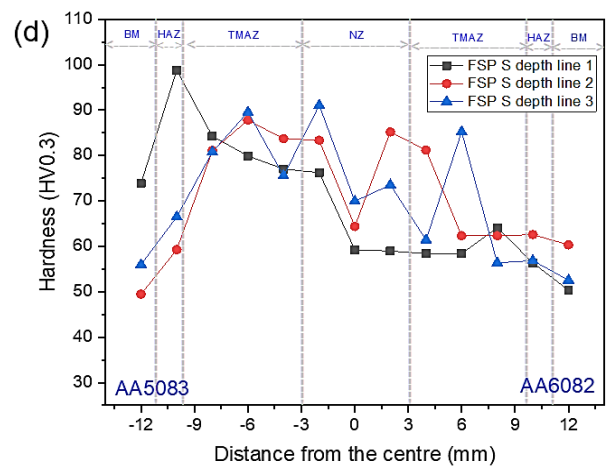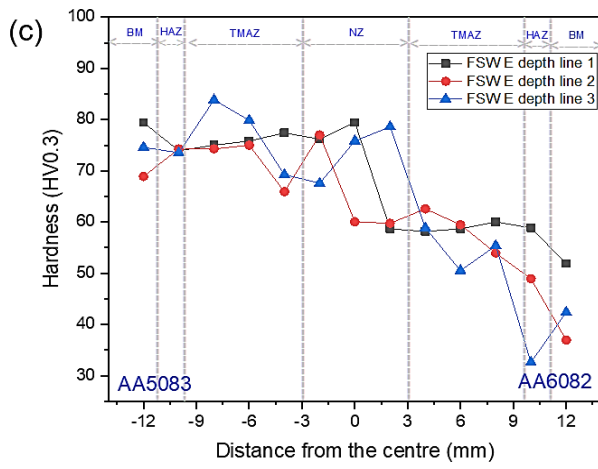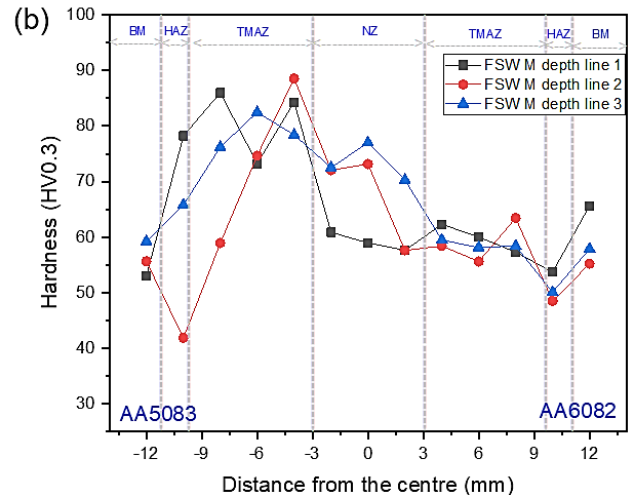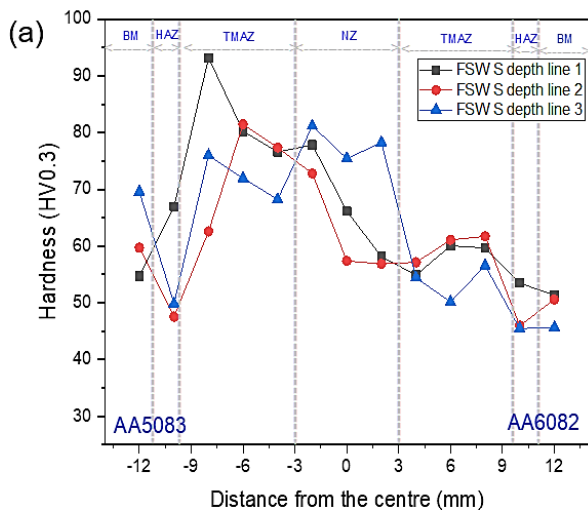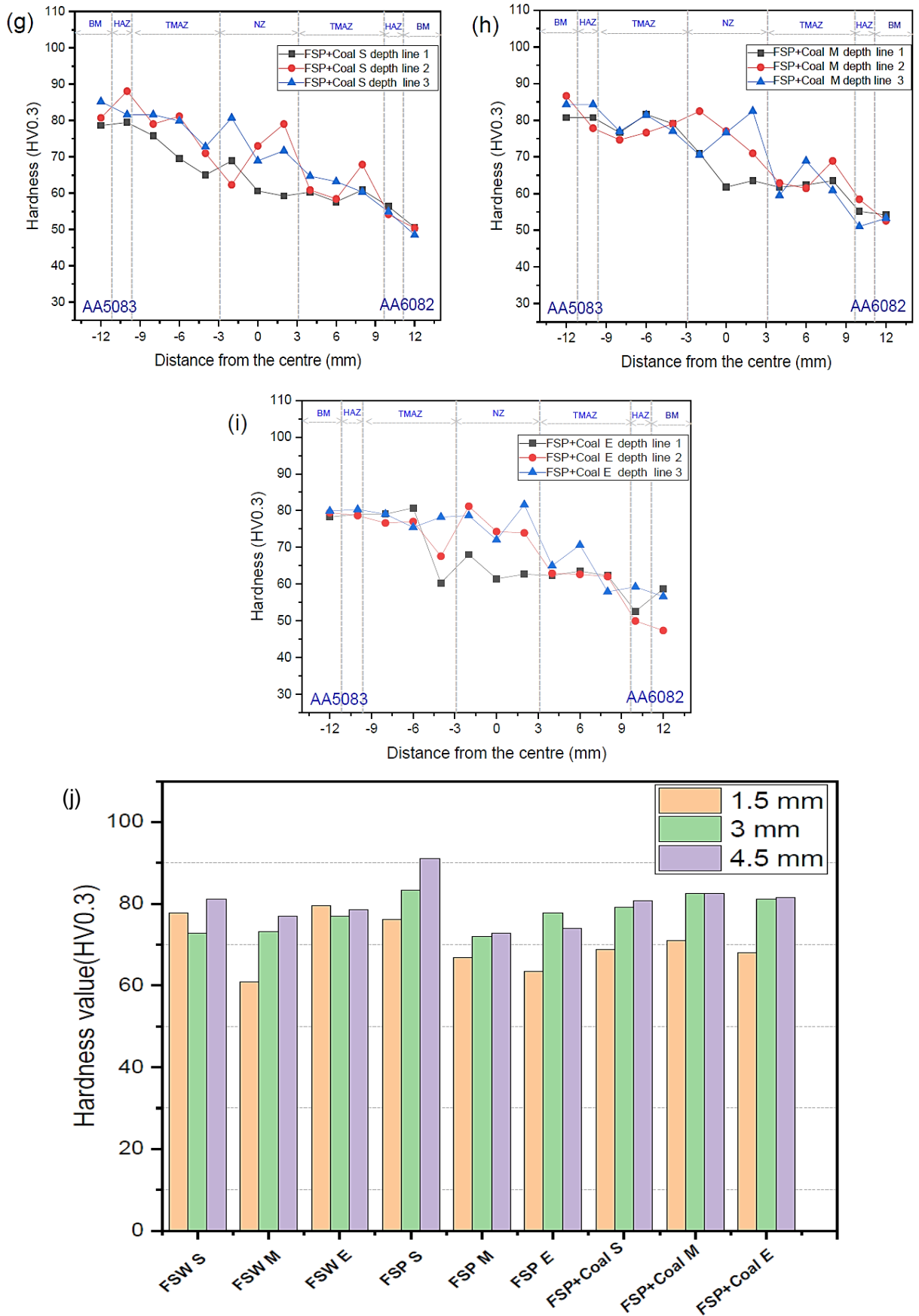
Figure 4.5: Hardness profiles; (a)FSW S, (b) FSW M, (c) FSW E, (d)FSP S, (e) FSP M , (f) FSP E, (g) FSP+Coal S, (h) FSP+Coal M, (i) FSP+Coal E, and (j) NZ Hardness bar charts.

4.6 Fracture surface analysis

Figure 4.6 illustrates the fracture surface morphology of the FSWed, FSPed, and FSP+Coal joints, providing insights into their respective failure mechanisms. The fractures exhibited a distinctive ductile nature, evident from the abundant presence of circular dimples with varying sizes [48, 59, 102-104]. Tensile specimen analysis further confirmed the predominant ductile failure mode of the joints. Worthy of note was the location of fractures: FSWed and FSPed joints displayed fractures primarily on the AA5083-H111 side, while the FSP+Coal joint exhibited failure on the AA6082-T651 side. This indicates a variation in failure behaviour resulting from different welding methods and reinforcement strategies [105-108]. The ductility of the joints was manifested through characteristic features discernible on the fracture surfaces. Micro-voids, indicating localised material deformation, were identified, underscoring the ductile nature of the fractures [108-110]. Additionally, the presence of dimples of varying sizes further substantiated the ductile failure mode, as these dimples typically form due to plastic deformation and material flow during fracture [111-112].

Furthermore, transgranular cleavage facets were observed, signifying a type of brittle fracture within the material's grains. This suggests that although the fractures were predominantly ductile, some localised areas experienced brittle failure, possibly due to variations in microstructural properties [103, 113-114]. The fracture surface also displayed grain boundaries, which could have played a role in causing the fracture behaviour. These boundaries may act as preferential paths for crack propagation, impacting the overall fracture resistance of the joints [105, 115]. Figure 4.6 highlights specific elements of the ductile characteristics, offering valuable insights into the failure mechanisms. Inclusion particles, indicated by the green arrow, were observable on the fracture surface, potentially contributing to stress concentrations and influencing crack initiation and propagation.

Intergranular fractures, denoted by the yellow markers, suggested that some fractures occurred along grain boundaries, further reinforcing the complex nature of the failure mechanisms involved. The presence of transgranular cleavage facets, represented by the red arrow, pointed to localised brittle fracture regions within the grains. These facets may be associated with regions of higher stress or variations in material properties [101, 116]. Micro-dimples, identified by the red circle, provide evidence of localised plastic deformation and indicate the presence of ductile behaviour during the fracture process. Lastly, micro-voids, marked by the blue arrow, were observed as small voids or cavities within the fracture surface, further underlining the ductile characteristics of the fractures.
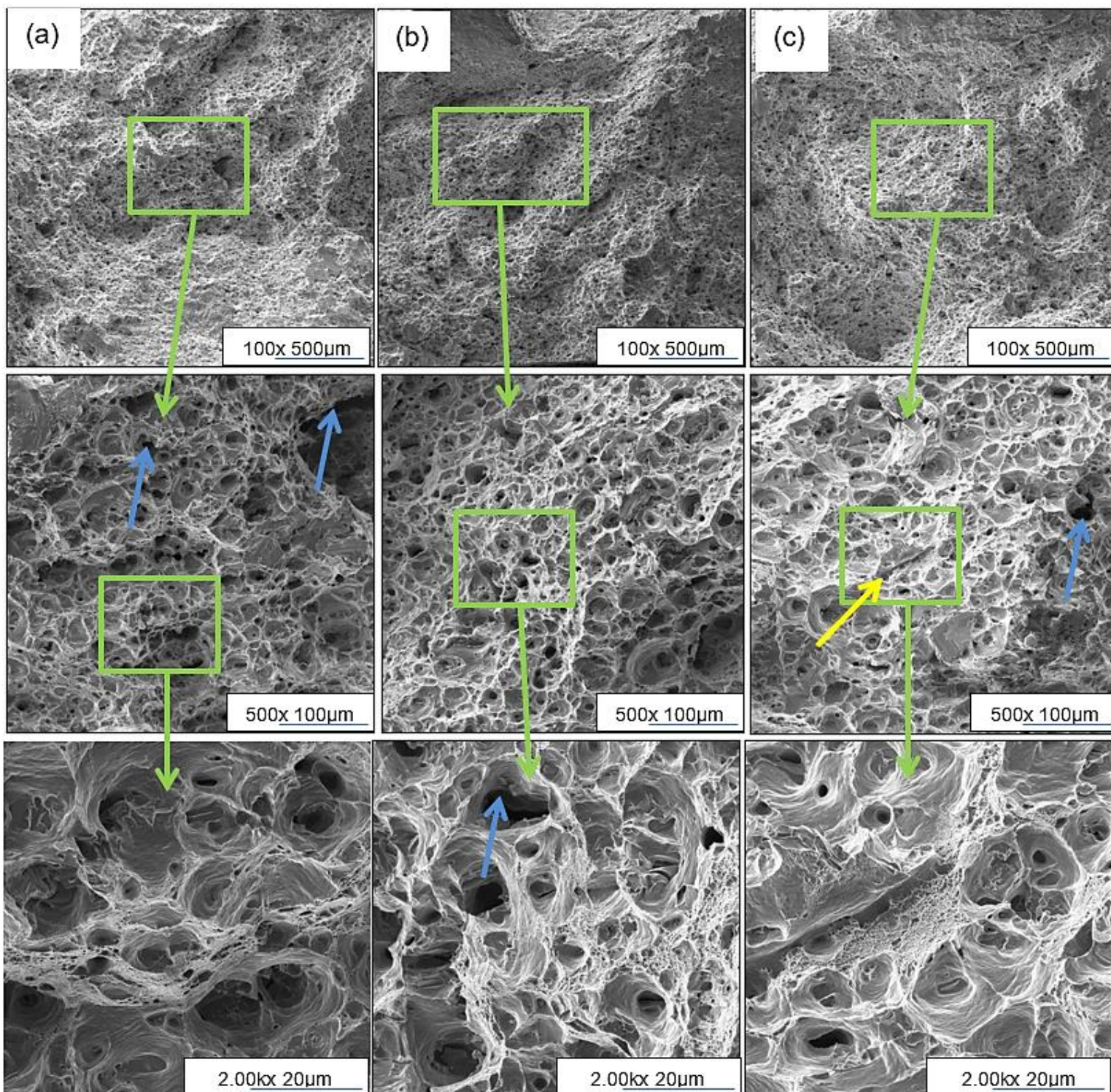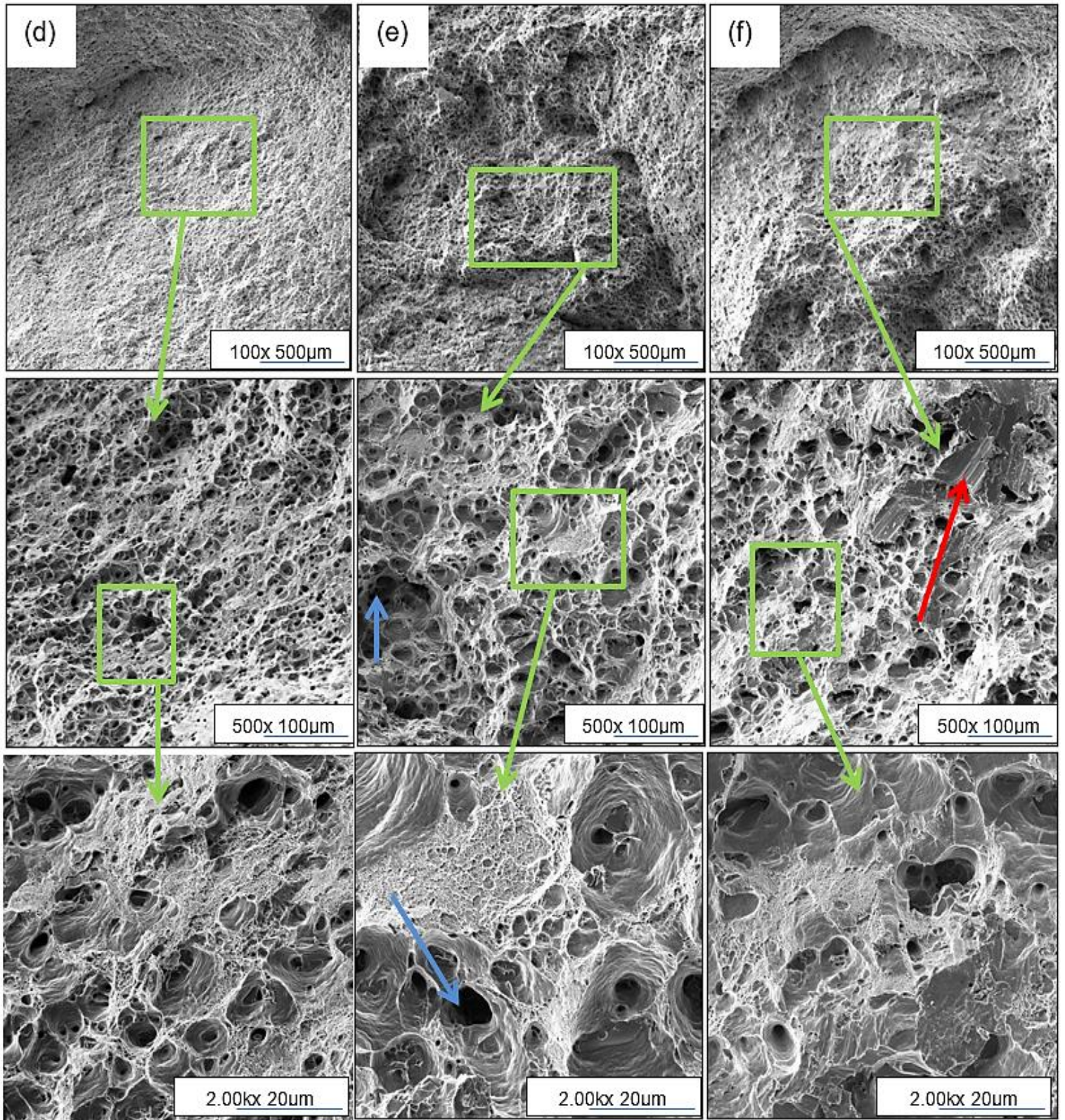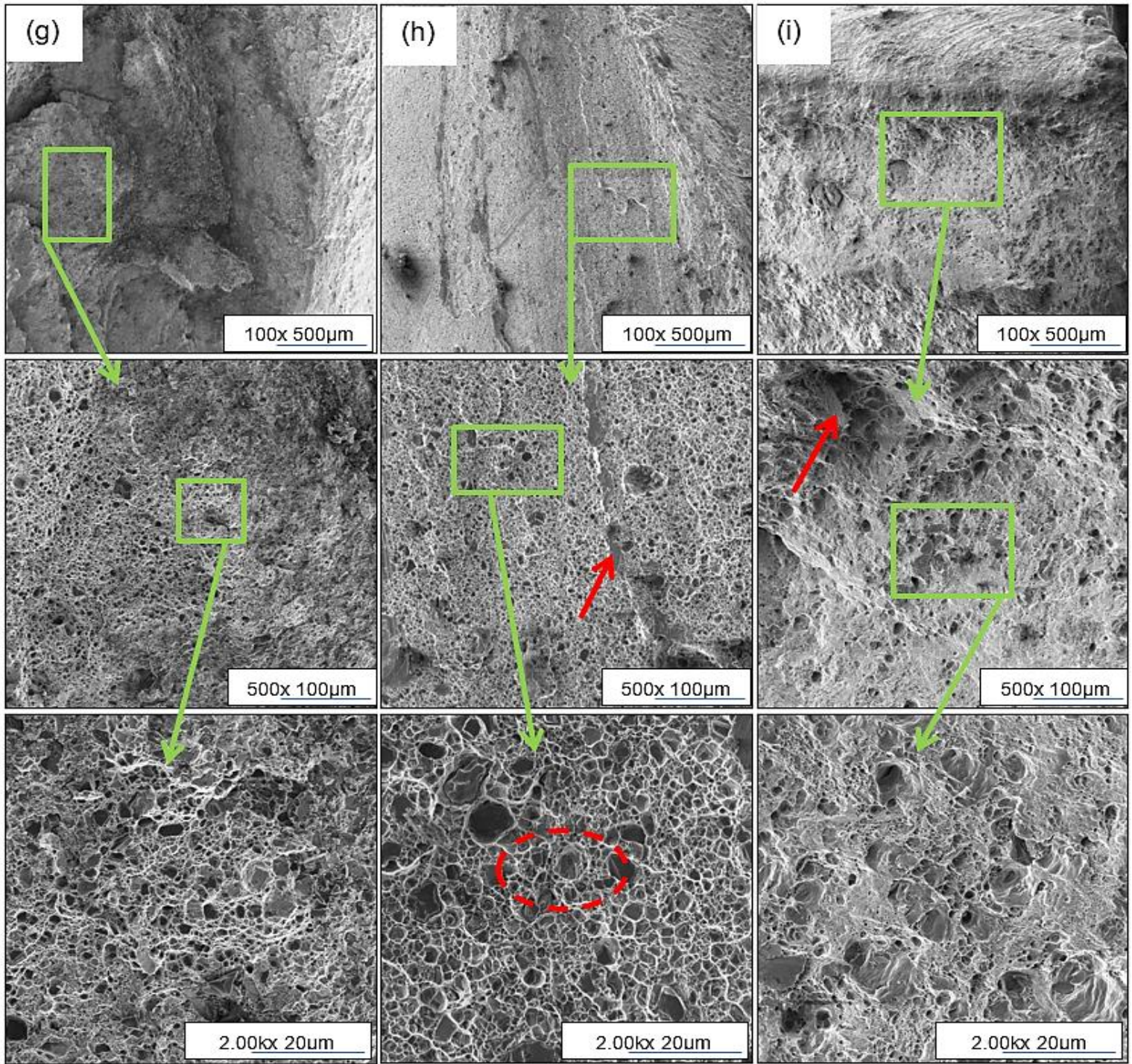
Figure 4.6: Fracture surface morphologies: FSW joints AA5083: (a) start (b) middle (c) end; FSP joints AA5083: (d) start (e) middle (f) end; FSP+Coal joints AA6082: (g) start (h) middle (i) end.

CHAPTER FIVE

CONCLUSIONS AND RECOMMENDATIONS

5.1 Conclusions

The aim of this research was to characterise the mechanical properties of friction stir processed AA5083/AA6082 dissimilar joints reinforced with coal. Metallographic and mechanical tests were performed on the joints produced and subjected to analysis. From the results of the analysis, the following conclusions were drawn:

The average mean grain size in the FSWed joints was 19.7 µm. This was significantly lower at 9.63 µm in the FSPed joints. Interestingly, the FSP+Coal method, which involved partial reinforcement with coal powder, resulted in an even more substantial mean grain refinement of 8.75 µm. This refinement was attributed to the introduction of coal particles that acted as nucleation sites during the processing, facilitating a more uniform distribution of fine grains throughout the microstructure. The resulting grain refinement has significant implications for the mechanical properties and performance of the processed material, making it an important consideration for engineering applications.

The results from the flexural tests showed that the root specimens produced by FSW failed at a maximum strain of 12.67% and flexural stress of 571 MPa. The root specimens created using FSP failed at a slightly higher maximum strain of 12.9% and a higher flexural stress of 581 MPa. In contrast, the root specimens manufactured through FSP+Coal failed at a lower maximum strain of 6.2% and a reduced flexural stress of 422 MPa. The face specimens obtained through FSW failed at a maximum strain of 12.7% and a flexural stress of 535 MPa. The face specimens formed by FSP experienced failure at a lower maximum strain of 10.81% but exhibited a higher flexural stress of 545.6 MPa. Lastly, the face specimens produced through FSP+Coal failed at a significantly lower maximum strain of 3% and a much lower flexural stress of 222 MPa.

The flexural results indicated that FSPed root specimens exhibited a slight improvement in both maximum strain and flexural stress over FSWed root specimens. This behaviour is associated with factors such as the grain refinement, thermomechanical processing, and potentially optimised particle distribution in FSPed joints. The inclusion of coal particles during FSP resulted in a significant reduction in both maximum strain and flexural stress values for both root and face specimens. It is important to consider these findings when choosing the appropriate welding method and reinforcement strategy for engineering applications, as they directly impact the mechanical properties and performance of the welded components. The significant reduction in both maximum strain and flexural stress in FSP+Coal specimens was linked to factors such as inhomogeneous particle distribution, weak particle-matrix interfaces, and suboptimal processing parameters.

The tensile properties of the joints were evaluated for FSWed, FSPed and FSP+Coal. For the FSWed joints, the maximum UTS achieved was 145.9 MPa at a tensile strain rate of 9.43%, while the minimum UTS observed was 93.43 MPa at a tensile rate of 7.02%. In the FSPed joints, the maximum UTS obtained was 170.9 MPa at a tensile strain rate of 9.13%, and the minimum UTS recorded was 126 MPa at a tensile strain rate of 7.38%. On the other hand, the FSP+Coal joints exhibited a maximum UTS of 142 MPa at a tensile strain rate of 9.28%, while the minimum UTS was 104.06 MPa at a tensile rate of 4.63%. Notably, the introduction of coal particle reinforcement led to a reduction in the UTS compared to FSWed and FSPed joints, indicating a trade-off between the presence of coal particles and tensile properties. It is worth noting that the FSP+Coal method had a positive impact on the properties of the AA6082-T651 material, despite the reduction in UTS. On the other hand, both FSWed and FSPed samples experienced fracture at the AA5083-H111 side, indicating different failure characteristics for the welding methods used.

In the hardness test results, the FSP+Coal joints achieved the highest hardness value of 70.74 HV at the nugget zone. The FSP joints recorded a hardness of 67.72 HV at the nugget zone, while the FSW joints had a slightly lower value of 64.64 HV at the nugget zone. The differences in the hardness of the joints can be attributed to the absence of the additional strengthening and grain refining effects observed in the FSP+Coal joints. The additional strengthening and grain refining effects observed in the FSP+Coal joints are a result of the dispersion strengthening mechanism, improved grain refinement, enhanced thermomechanical processing, and the strengthening of the particle-matrix interface. These effects collectively contribute to the superior mechanical properties and increased hardness of the FSP+Coal joints compared to standard FSP and FSW joints without coal particle reinforcement. Near the tool pin and tool shoulder positions on the AA6082-T651 side, the hardness values were relatively lower compared to other positions. However, in the nugget zone, there was a significant increase in hardness values along the entire length of the welded joint, which surpassed the hardness of the AA6082-T651 HAZ side.

The fracture surface morphology analysis revealed a prominent ductile failure mechanism in the FSWed, FSPed, and FSP+Coal joints. The distinct features observed on the fracture surfaces provided valuable information about the localised deformation and fracture behaviour within the joints. The specific elements of the ductile characteristics, including inclusion particles, intergranular fractures, transgranular cleavage facets, micro-dimples and micro-voids, collectively contribute to a comprehensive understanding of the fracture processes involved in these welding joints.

In summary, the introduction of coal particles during FSP resulted in a refined microstructure, superior mechanical properties, and increased hardness at the nugget zone in comparison to FSW and standard FSP joints. However, the choice of reinforcement strategy should take into account the specific requirements of the application, as the presence of coal

particles may lead to trade-offs in certain mechanical properties. Overall, the findings provided valuable insights into how to optimise the FSP process for dissimilar joints while highlighting the potential benefits of using coal as a reinforcement for FSP joints in materials processing, welding, and engineering applications. Leveraging the knowledge gained can result in enhancement of the performance and reliability of welded joints, leading to improved products and technologies.

5.2 Recommendations

Based on the results obtained from the study, the following recommendations can be made:

- Further Investigation of Reinforcement Strategies: While the introduction of coal particles as a reinforcement in Friction Stir Processing (FSP+Coal) showed promising results, future studies can explore other reinforcement materials or techniques. Investigating different types of particles, such as ceramic or metal reinforcements, should produce insights into their effects on microstructure and mechanical properties.

- Optimal Particle Distribution: The observed reduction in ultimate tensile stress (UTS) and flexural stress in FSP+Coal specimens suggests that optimising the distribution of coal particles within the material matrix is crucial. Future research should focus on improving the homogeneity of particle dispersion to achieve more consistent and enhanced mechanical properties.

- Particle-Matrix Interface Improvement: Strengthening the bond between coal particles and the matrix material is essential for efficient load transfer and reinforcement. Future studies can explore surface treatments or chemical modifications to enhance the particle-matrix interface, leading to better mechanical performance.

- Impact of Particle Size and Content: Investigating the impact of different particle sizes and content levels on the mechanical properties of FSP joints can provide valuable information for tailoring reinforcement strategies. This will help to determine the optimal particle size and content for achieving desired microstructural and mechanical improvements.

- Evaluation of Fatigue and Fracture Behaviour: Future studies should explore the fatigue and fracture behaviour of FSP+Coal joints to assess their long-term durability and performance under cyclic loading conditions. This will assist in determining the suitability of FSP+Coal joints for critical applications in industries such as aerospace and transportation.

- Comparison with Other Welding Methods: To provide a comprehensive assessment of the FSP+Coal method, future studies might compare its mechanical properties and

microstructure with other advanced welding techniques, such as laser welding, electron beam welding, or friction stir spot welding.

- Real-World Applications: Evaluating the performance of FSP+Coal joints in real-world engineering applications can offer useful insights into the practical benefits and challenges of using coal particle reinforcement. Field trials and performance testing in relevant industries will furnish valuable feedback for further improvement and optimisation.
- Environmental Impact Assessment: Future studies should also include an environmental impact assessment to understand any potential environmental issues associated with the use of coal particles as a reinforcement strategy.

By addressing these recommendations, future research can achieve a deeper understanding of the FSP+Coal method and its potential for enhancing the mechanical properties of dissimilar aluminium alloy joints, leading to the development of more advanced and reliable welding techniques in various engineering applications.

REFERENCES

1. Cevik, E., Sun, Y. and Ahlatci, H. 2012. Effect of peak-aged heat treatment on corrosion behavior of the AA6063 alloy containing Al 3 Ti. *Arch. Metall. Mater., 57:* 469-477.

2. Rambabu, P.P.N.K.V., Prasad, N.E., Kutumbarao, V.V. and Wanhill, R.J.H. 2017. Aluminium alloys for aerospace applications. *Aero. Mater. Mat. Technol.*, 29-52.

3. Poznak, A., Freiberg, D. and Sanders, P. 2018. Automotive wrought aluminium alloys. In Fundamentals of Aluminium Metallurgy (pp. 333-386). Woodhead Publishing.

4. Polmear, I., John, D.S., Nie, J.F., Qian, M. 2021. Light Alloys: Metallurgy of the Light Metals, 2017 Academic Press Elsevier, Butterworth- Heinemann [15 August 2021].

5 Aalco - Ferrous and Non-Ferrous Metals Stockist (2020). Aluminium Alloys - Aluminium 6082 Properties, Fabrication and Applications. AZoM. https://www.azom.com [15 August 2021].

6. Liechty, B.C., Webb, B.W. 2008. Flow field characterization of friction stir processing using a particle-grid method. *J. Mater. Process. Technol., 208(1–3):* 431-443.

7. Lim, D.K., Shibayanagi, T., Gerlich, A.P., 2009. Synthesis of multi-walled CNT reinforced aluminium alloy composite via friction stir processing. *Mat. Sci. Eng. A 507:* 194–199.

8. Mishra, R.S., Mahoney, M.W., McFadden, S.X., Mara, N.A., Mukherjee, A.K., 1999. High strain rate superplasticity in a friction stir processed 7075 Al alloy. *Scripta Mater. 42:* 163–168.

9. Ralls, A.M., Kasar, A.K. and Menezes, P.L., 2021. Friction stir processing on the tribological, corrosion, and erosion properties of steel: A review. *J. Manuf. Mater. Process., 5(3):* 97.

10. Saravanan, R., Rao, M.S.S., Malyadri, T., Sunkara, N. 2020. Profile Optimization in Tool tip for FSW Process—A Numerical Investigation. In: Narasimham G., Babu A., Reddy S., Dhanasekaran R. (eds) Recent Trends in Mechanical Engineering. Lecture Notes in Mechanical Engineering. Springer, Singapore.

11. Sivaraman, P., Nithyanandhan, T., Karthick, M., Kirivasan, S.M., Rajarajan, S. and Sundar, M.S. 2021. Analysis of tensile strength of AA 2014 and AA 7075 dissimilar metals using friction stir welding. *Mater. Today: Proc., 37:* 187-192.

12. Kalashnikova, T.A., Chumaevskii, A.V., Rubtsov, V.E., Ivanov, A.N., Alibatyro, A.A. and Kalashnikov, K.N., 2017, December. Structural evolution of multiple friction stir processed AA2024. In AIP Conference Proceedings (Vol. 1909(1): 020077). AIP Publishing LLC.

13. Sharma, A., Sharma, V.M., Mewar, S., Pal, S.K., Paul, J. 2018. Friction stir processing of Al6061-SiC-graphite hybrid surface composites. *Mater. Manuf. Process., 33(7):* 795-804.

14. Costa, M.I., Verdera, D., Vieira, M.T., Rodrigues, D.M. 2014. Surface enhancement of cold work tool steels by friction stir processing with a pinless tool. *Appl. Surf. Sci.,* 296: 214–220.

15. Mahmoud, E.R.I., Al-qozaim, A.M.A. 2016. Fabrication of In-Situ Al–Cu intermetallics on aluminum surface by friction stir processing. *Arab J. Sci. Eng., 41:* 1757–1769.

16. Ikumapayi, O.M. 2020. Surface Composites and Functionalisation: Enhancement of Aluminium Alloy 7075-T651 via Friction Stir Processing. Johannesburg: University of Johannesburg. http://hdl.handle.net/10210/443819 [3 August 2021].

17. Wang, W., Shi, Q.Y., Liu, P., Li, H.K., Li, T. 2009. A novel way to produce bulk SiCp reinforced aluminium metal matrix composites by friction stir processing. *J. Mater. Process. Technol.,* 209(4): 2099-2103.

18. Fernandez, G.J., Murr, L.E. 2004. Characterization of tool wear and weld optimization in the friction-stir welding of cast aluminum 359+20% SiC metal-matrix composite. *Mater. Charact.* 52: 65–75.

19. Uzun, H. 2007. Friction stir welding of SiC particulate reinforced AA2124 aluminium alloy matrix composite. *Mater. Des. 28:* 1440–1446.

20. Feng, A., Xiao, B., Ma, Z.Y. 2008. Effect of microstructural evolution on mechanical properties of friction stir welded AA2009/SiCp composite. *Compos. Sci. Technol. 68:* 2141–2148.

21. Dinaharan, I., Sathiskumar, R., Murugan, N. 2016. Effect of ceramic particulate type on microstructure and properties of copper matrix composites synthesized by friction stir processing. *J. Mater. Res. Technol. 5,* 302–316.

22. Sharma, A., Sharma, V.M., Mewar, S., Pal, S.K., Paul, J. 2017. Friction stir processing of Al6061-SiC-graphite hybrid surface composites. *Mater. Manuf. Process.,*1–9.

23. Periyasamy, P., Mohan, B., Balasubramanian, V. 2012. Effect of heat input on mechanical and metallurgical properties of friction stir welded AA6061-10% SiCp MMCs. *J. Mater. Eng. Perform., 21(11):* 2417-2428.

24. Khojastehnezhad, V.M., Pourasl, H.H. 2018. Microstructural characterization and mechanical properties of aluminum 6061-T6 plates welded with copper insert plate (Al/Cu/Al) using friction stir welding. *Trans. Nonferrous Met. Soc. China, 28(3):* 415-426.

25. Arab, S.M., Karimi, S., Jahromi, S.A.J., Javadpour, S., Zebarjad, S.M. 2015. Fabrication of novel fiber reinforced aluminum composites by friction stir processing. *Mater. Sci. Eng. A, 632:* 50-57.

26. Abbasi, M., Abdollahzadeh, A., Omidvar, H., Bagheri, B., Rezaei, M. 2016. Incorporation of SiC particles in FS welded zone of AZ31 Mg alloy to improve the mechanical properties and corrosion resistance. *Int. J. Mater. Res., 107(6):* 566-572.

27. Mehdi, H. and Mishra, R.S. 2020. Investigation of mechanical properties and heat transfer of welded joint of AA6061 and AA7075 using TIG+ FSP welding approach. *J. Adv. Join. Process.,* 1:100003.

28. Rana, H.G., Badheka, V.J., Kumar, A. 2016. Fabrication of Al7075/B4C surface composite by novel friction stir processing (FSP) and investigation on wear properties. *Procedia Technol., 23:* 519-528.

29. Kurt, A., Uygur, I. and Cete, E. 2011. Surface modification of aluminium by friction stir processing. *J. mater. Process. Technol., 211(3):* 313-317.

30. Sharma, A., Sharma, V.M., Mewar, S., Pal, S.K., Paul, J. 2018. Friction stir processing of Al6061-SiC-graphite hybrid surface composites. *Mater. Manuf. Process., 33(7):* pp.795-804.

31. Palanivel, R., Dinaharan, I., Laubscher, R.F. Davim, J.P. 2016. Influence of boron nitride nanoparticles on microstructure and wear behavior of AA6082/TiB2 hybrid aluminium composites synthesized by friction stir processing. *Mater. Des., 106*: 195-204.

32. Selvakumar, S., Dinaharan, I., Palanivel, R., Babu, B.G., 2017. Characterization of molybdenum particles reinforced Al6082 aluminum matrix composites with improved ductility produced using friction stir processing. Mater. *Charact., 125:* 13-22.

33. Selvakumar, S., Dinaharan, I., Palanivel, R., Babu, B.G., 2017. Development of stainless steel particulate reinforced AA6082 aluminum matrix composites with enhanced ductility using friction stir processing. *Mater. Sci. Eng. A, 685:* 317-326.

34. Da Silva, J., Costa, J.M., Loureiro, A., Ferreira, J.M., 2013. Fatigue behaviour of AA6082-T6 MIG welded butt joints improved by friction stir processing. *Mater. Des. 51:* 315-322.

35. Ramesh, A., Indira, M., Rani, A.P. 2016. Influence of tool design on the mechanical properties in friction stir welding of AA6082-T6 aluminum alloy. *IJSER, 7(6):* 168-172.

36. Valate, A., Raut, A., Salunke, S., Thombare, S., Umbarkar, A.M. 2016. Investigation of variation in tensile strength of FSW butt joints of Al 6082-T6 aluminum with Welding Speed and Tool Pin Profiles. *IRJET, 3(6):* 537–542.

37. Srinivasulu, P., Rao, G.K.M., Gupta, M.S. 2015. Evaluation of Bending Strength of Friction Stir Welded Aa 6082 Aluminum Alloy Butt Joints. *IJARSE, 8354(4):* 1262–1270.

38. Krzysztof, M., Kurtyka, P. 2015. Microstructure and properties of 6082 aluminium alloy friction stir welded with different parameters of welding. 1-8.

39. Devaraju, A., et al., Study of mechanical properties microstructures and in similar and dissimilar friction stir welding of AA5083. [ICIEMS2014].

40. Jaiswal, D., Kumar, R., Singh, R., Pandey, S., Prasad, R. 2014. Influence of cooling media on mechanical properties of friction stir welded 1060 aluminium alloy, no 4, 54–57.

41. Saravanakumar, R., Krishna, K., Rajasekaran, T., Siranjeevi, S. 2018. Investigations on friction stir welding of AA5083-H32 marine grade aluminium alloy by the effect of varying the process parameters. *IOP Conf. Ser.: Mater. Sci. Eng., 402:* 012187.

42. Ravindar, B., Gururaj, K. 2015. Effects of Friction Stir Welding Parameters on Butt Joint Properties of Aluminium Alloy 5083. *Int. J. Innov. Res. Technol. Sci. Eng., 4(7):* 6531–6537.

43. Chander, S.M., Satish Kumar, P., Devaraju, A. 2018. Influence of tool rotational speed and pin profile on mechanical and microstructural characterization of friction stir welded 5083 aluminium alloy. *Mater. Today: Proc., 5(2):* 3518–3523.

44. Kumar, A.H.M., Venkata Ramana, V. 2020. Influence of tool parameters on the tensile properties of friction stir welded aluminium 5083 and 6082 alloys. *Mater. Today: Proc., 27:* 951–957.

45. Leitão, C., Louro, R., Rodrigues, D.M. 2012. Analysis of high temperature plastic behaviour and its relation with weldability in friction stir welding for aluminium alloys AA5083-H111 and AA6082-T6. *Mater. Des., 37:* 402–409.

46. Msomi, V., Mbana, N. Mechanical properties of friction stir welded AA1050H14 and AA5083-H111 joint: sampling aspect, *Met., 10(2),* **2020**, 214.

47. Jain, S., Sharma, N., Gupta, R. 2017. Dissimilar alloys (AA6082/AA5083) joining by FSW and parametric optimization using Taguchi, grey relational and weight method. *Eng. Solid Mech.,* 6(1): 51–66.

48. Kumar, Y., Kumar, A., Rajyalakshmi. 2014. Optimization of process parameters during Friction Stir Welding of Aluminium 5083 & 6082 Alloys. *IJCET, 4(6):* 4144–4152.

49. da Silva, J., Costa, J.M., Loureiro, A., Ferreira, J.M. 2013. Fatigue behaviour of AA6082-T6 MIG welded butt joints improved by friction stir processing. *Mater. Des., 51:* 315-322

50. Chanakyan, C., Sivasankar, S., Meignanamoorthy, M., Ravichandran, M., Muralidharan, T. 2020. Experimental investigation on influence of process parameter on friction stir processing of AA6082 using response surface methodology. *Mater. Today: Proc., 21:* 231-236.

51. Jiang, H.J., Liu, C.Y., Zhang, B., Xue, P., Ma, Z.Y., Luo, K., Ma, M.Z., Liu, R.P. 2017. Simultaneously improving mechanical properties and damping capacity of Al-Mg-Si alloy through friction stir processing. *Mater. Charact., 131:* 425-430.

52. Pradeep, S., Jain, V.K.S., Muthukumaran, S., Kumar, R. 2021. Microstructure and texture evolution during multi-pass friction stir processed AA5083. *Mater. Letters, 288:* 129382.

53. Vignesh, R.V., Padmanaban, R. 2018. Influence of friction stir processing parameters on the wear resistance of aluminium alloy AA5083. *Mater. Today: Proc., 5(2):* 7437-7446.

54. Hussein, W., Al-Shammari, M.A. 2018. Fatigue and fracture behaviours of FSW and FSP Joints of AA5083-H111aluminium alloy. *IOP Conf. Ser.: Mater. Sci. Eng., 52(43):* 454012055.

55. Jesus, J.S., Costa, J.M., Loureiro, A., Ferreira, J.M. 2017. Fatigue strength improvement of GMAW T-welds in AA 5083 by friction-stir processing. *Int. J. Fatigue, 97:* 124-134.

56. Mabuwa, S., Msomi, V. 2021. The effect of FSP conditions towards microstructure and mechanical properties of the AA6082/AA8011 TIG-welded joint. *Mater. Res. Express, 8(6):* 066514.

57. Thangarasu, A., Murugan, N., Dinaharan, I., Vijay, S.J. 2015. Synthesis and characterization of titanium carbide particulate reinforced AA6082 aluminium alloy composites via friction stir processing. *Arch. Civ. Mech. Eng., 15(2):* 324-334.

58. Thangarasu, A., Murugan, N., Dinaharan, I., Vijay, S.J. 2014. Influence of transverse speed on microstructural and mechanical properties of AA 6082-TiC surface composite fabricated by Friction Stir Processing. *Procedia Material Science, 5:* 2115-2121.

59. Thangarasu, A., Murugan, N., Dinaharan, I. 2014. Production and wear characterization of AA6082 -TiC surface composites by friction stir processing. *Procedia Eng., 97:* 590-597.

60. Huang, G., Shen, Y. 2017. The effects of processing environments on the microstructure and mechanical properties of the Ti/5083Al composites produced by friction stir processing. *J. Manuf. Process., 30*: 361-373.

61. Kumar, V., Jain, S., Muhammed, P.M., Muthukumaran, S., Babu, S.P.K. 2018. Microstructure, mechanical and sliding wear behavior of AA5083-B4C/SiC/TiC surface composites fabricated using friction stir processing. *Trans. Indian Inst. Met., 71(6):* 1519-1529.

62. ASTM International Standard Test Methods for Tension Testing of Metallic Materials (ASTM E8M-04). 2004; pp. 1–24. Available online: https://www.astm.org/Standards/E8M.htm (accessed on 28 June 2023).

63. ASTM E290-20, Standard Test Methods for Bend Testing of Material for Ductility, PA, 2020, Available online: www.astm.org/doi/10.1520/E0290-20. (Accessed 28 June 2023).

64. ASTM International Standard Test Method for Microindentation Hardness of Materials (ASTM E384-11). 2011; pp. 1–24. Available online: https://www.astm.org/Standards/E384.htm (accessed on 28 June 2023).

65. ASTM International Standard Test Methods for Determining Average Grain Size (ASTM E112-12). 2012; pp. 1–27. Available online: https://www.astm.org/Standards/E112.htm (accessed on 28 June 2023).

66. Sathari, N.A.A., Razali, A.R., Ishak, M., Shah, L.H. 2015. Mechanical strength of dissimilar AA7075 and AA6061 aluminum alloys using friction stir welding. *Int. J. Automot. Mech. Eng.,* 11(1): 2180-1606.

67. Msomi, V., Mbana, N. 2020. Mechanical properties of friction stir welded AA1050-H14 and AA5083-H111 Joint: Sampling aspect. *Met., 10(2):* 214.

68. Cavaliere, P., Panella, F. 2008. Effect of tool position on the fatigue properties of dissimilar 2024-7075 sheets joined by friction stir welding. *J. Mater. Process. Technol., 206:* 249–255.

69. Kopyściański, M., Węglowska, A., Pietras, A., Hamilton, C., Dymek, S. Friction stir welding of dissimilar aluminum alloys. *Key Eng. Mater., 682*, **2016**, 31–7.

70. Kumar-Singh, S., Tiwaria, R.M., kumara, A., Kumar, S., Murtaza, Q., Kumar, S. 2018. Mechanical properties and microstructure of Al-5083 by TIG. *Mater. Today: Proc. 5:* 819–822.

71. Sorger, G., Sarikka, T., Vilaça, P., Santos T.G. 2018. Effect of processing temperatures on the properties of a high-strength steel welded by FSW. *Weld. World, 62:* 1173–1185.

72. Baral, S.K., Thawre, M.M., Sunil, B.R., Dumpala, R. 2023. A review on developing high-performance ZE41 magnesium alloy by using bulk deformation and surface modification methods. *J. Magnes. Alloy, 11(3):* 776-800.

73. Mazaheri, Y., Jalilvand, M.M., Heidarpour, A., Jahani, A.R. 2020. Tribological behavior of AZ31/ZrO2 surface nanocomposites developed by friction stir processing. *Tribol. Int., 143:* 106062.

74. Ahmed, H.M., Ahmed, H.A.M., Hefni, M., Moustafa, E.B. 2021. Effect of Grain Refinement on the Dynamic, Mechanical Properties, and Corrosion Behaviour of Al-Mg Alloy. *Met., 11(11):* 1825.

75. Heidarzadeh, A., Javidani, M., Mofarrehi, M., Motalleb-Nejad, P., Mohammadzadeh, R., Jafarian, H., Chen, X.G. 2023. Grain Structure formation and texture modification through multi-pass friction stir processing in AlSi10Mg alloy produced by laser powder bed fusion. *Mater.,16(3):* 944.

76. Alaneme, K.K., Okotete, E.A., Fajemisin, A.V., Bodunrin, O.M. 2019. Applicability of metallic reinforcements for mechanical performance enhancement in metal matrix composites: a review. *Arab J. Basic Appl. Sci., 26(1):* 311-330.

77. Bryła, K. 2020. Microstructure and mechanical characterisation of ECAP-ed ZE41A alloy. *Mater. Sci. Eng. A, 772:* 138750.

78. Khalafe, W.H., Sheng, E.L., Bin Isa, M.R., Omran, A.B., Shamsudin, S.B. 2022. The effect of friction stir welding parameters on the weldability of aluminum alloys with similar and dissimilar metals: Review. *Met., 12(12):* 2099.

79. Zoalfakar, S.H., Mohamed, M.A., Abdel Hamid, M., Megahed, A.A. 2022. Effect of friction stir processing parameters on producing AA6061/ tungsten carbide nanocomposite. *Proceedings of the Institution of Mechanical Engineers, Part E: Journal of Process Mechanical Engineering. 236(2):* 653-667.

80. Dudzik, K., Czechowsk,i M. 2023. The Cracking of Al-Mg Alloys Welded by MIG and FSW under Slow Strain Rating. *Mater.,16(7):* 2643.

81. Singh, T. 2023. Nanoparticles reinforced joints produced using friction stir welding: a review. *Eng. Res. Express 5:* 022001.

82. Raja, S., Muhamad, M.R., Jamaludin, M.F., Yusof, F. 2020. A review on nanomaterials reinforcement in friction stir welding. J. Mater. Res. Technol., 9(6): 16459-16487.

83. Moradi, M.M., Aval, H.J., Jamaati, R. 2017. Effect of pre and post-welding heat treatment in SiC-fortified dissimilar AA6061-AA2024 FSW butt joint. *J. Manuf. Process., 30:* 97–105.

84. Shalok, B., Nilesh, D.G., Kaushik, M.P. 2020. A review on manufacturing the surface composites by friction stir processing. *Mater. Manuf. Process., 36:* 135–70.

85. Abioye, T.E., Zuhailawati, H., Anasyida, A.S., Yahaya, S.A., Dhindaw, B.K. 2019, Investigation of the microstructure, mechanical and wear properties of AA6061-T6 friction stir weldments with different particulate reinforcements addition. *J. Mater. Res. Technol., 8:* 3917–28.

86. Ma, Z.Y., Feng, A.H., Chen, D.L., Shen, J. 2017. Recent advances in friction stir welding/processing of aluminum alloys: microstructural evolution and mechanical properties. *Crit. Rev. Solid State Mater. Sci.,* 1–65.

87. Saeidi, M., Givi, M.K.B., Faraji, G. 2016. Study on ultrafine-grained aluminum matrix nanocomposite joint fabricated by friction stir welding. *Indian J. Eng. Mater. Sci. 23:* 152–8.

88. Yan, Z., Zheng, J., Zhu, J., Zhang, Z., Wang, Q., Xue, Y. 2020. High ductility with a homogeneous microstructure of a Mg–Al–Zn alloy prepared by cyclic expansion extrusion with an asymmetrical extrusion cavity. *Met., 10(8):* 1102.

89. Yang, J., Bu, K., Zhou, Y., Song, K., Huang, T., Peng, X., Liu, H., Du, Y. 2023. Microstructure, residual stress, and mechanical properties evolution of a Cu–Fe–P alloy under different conditions. *J. Mater. Res. Technol., 24:* 7896-7909.

90. Zhao, W., Liu, R., Yan, J., Wang, X., Zhang, H., Wang, W. 2022. Overall optimization in microstructure and mechanical properties of 5 wt% SiC/7075Al composites by high-frequency electric pulse assisted treatment. *J. Mater. Res. Technol., 21:* 2156-2167.

91. Speight, J.G., 8 - Assessing fuels for gasification: analytical and quality control techniques for coal, Editor(s): Rafael Luque, James G. Speight, In Woodhead Publishing Series in Energy, Gasification for Synthetic Fuel Production, Woodhead Publishing, 2015, 175-198.

92. Esterle, J.S., Chapter 3 - Mining and Beneficiation, Editor(s): Suárez-Ruiz, I., Crelling, J.C., Applied Coal Petrology, Elsevier, 2008, 61-83.

93. Dragatogiannis, D.A., Koumoulos, E.P., Kartsonakis, I.A., Pantelis, D.I., Karakizis P.N., Charitidis, C.A. 2016. Dissimilar friction stir welding between 5083 and 6082 Al alloys reinforced with TiC nanoparticles. *Mater. Manuf. Process., 31(16):* 2101-2114.

94. Di Bella, G., Favaloro, F., Borsellino, C. 2023. Effect of process parameters on friction stir welded joints between dissimilar aluminum alloys: A review. *Met., 2023; 13(7):* 1176.

95. Mabuwa, S., Msomi, V. 2020. Review on friction stir processed TIG and friction stir welded dissimilar alloy joints. *Met., 10(1):* 142.

96. Abnar, B., Gashtiazar, S., Javidani. M. 2023. Friction stir welding of non-heat treatable Al Alloys: Challenges and improvements opportunities. *Crystals,13(4): 576.*

97. Wiechmann, P., Panwitt, H., Heyer, H., Reich, M., Sander, M., Kessler, O. 2018. Combined calorimetry, thermo-mechanical analysis and tensile test on welded EN AW-6082 joints. *Mater., 11(8):* 1396.

98. Fröck, H., Milkereit, B., Wiechmann, P., Springer, A., Sander, M., Kessler, O., Reich, M. 2018. Influence of solution-annealing parameters on the continuous cooling precipitation of aluminum alloy 6082. *Met., 8(4):* 265

99. Sameer, M.D., Birru, A.K. 2019. Mechanical and metallurgical properties of friction stir welded dissimilar joints of AZ91 magnesium alloy and AA 6082-T6 aluminium alloy. *J. Mag. Alloys, 7(2):* 264-271.

100. Ravikumar, S., Seshagiri-Rao, V., Pranesh, R.V. 2014. Effect of welding parameters on macro and microstructure of friction stir welded butt joints between AA7075-T651 and AA6061-T651alloys. *Proc. Mater. Sci., 5:* 1725–35.

101. Verma, S., Gupta, M., Misra, J.P. 2016. Friction stir welding of aerospace materials: A state of art review, Chapter 13 in DAAAM International Scientific Book, 135-150, B. Katalinic (Ed.). Published by DAAAM. International, ISBN 978-3-902734- 09-9, ISSN 1726-9687, Vienna, Austria.

102. Derazkola, H.A., Eyvazian, A., Simchi, A. 2020. Submerged friction stir welding of dissimilar joints between an Al-Mg alloy and low carbon steel: thermo-mechanical modelling, microstructural features, and mechanical properties. *Manuf. Process., 50:* 68–79.

103. Huang, G., Wu, J., Hou, W., Shen, Y. 2018. Microstructure, mechanical properties and strengthening mechanism of titanium particle reinforced aluminum matrix composites produced by submerged friction stir processing. *Mater. Sci. Eng. A, 734:* 353–363.

104. Ramaiyan, S., Santhanam, S.K.V., Muthuguru, P. 2018. Effect of scroll pin profile and tool rotational speed on mechanical properties of submerged friction stir processed AZ31B magnesium alloy. *Mater. Res., 21(3):* e20170769.

105. Li, L., Liu, H., Gu, N., Xiao, X., Dai, S., Liu, J., Yi, D. 2022. Improving strength and ductility of Ti-4Al-0.005B titanium alloy through tailoring equiaxed and lamellar microstructure during thermal mechanical process. *J. Mater. Res. Technol., 20:* 3158-3172.

106. Subramani, V., Jayavel, B., Sengottuvelu, R., Lazar, P.J.L. 2019. Assessment of microstructure and mechanical properties of stir zone seam of friction stir welded magnesium AZ31B through Nano-SiC. *Mater., 12(1044)*: 1-19.

107. Prosgolitis, C.G., Lambrakos, S., Zervaki, A.D. 2018. Phase-field modelling of nugget zone for a AZ31-Mg-Alloy friction stir weld. *J. Mater. Eng. Perform. 2(10):* 5102–5113.

108. Lv, J., Zheng, J.H., Yardley, V.A., Shi, Z., Lin, J. 2020. A Review of microstructural evolution and modelling of aluminium alloys under hot forming conditions. *Met., 10(11)*: 1516.

109. Yan, Y., Li, H., Zhang, J., Kong, N. 2019. The effect of initial annealing microstructures on the forming characteristics of Ti-4Al-2V titanium alloy. *Met., 9(5):* 576 -589.

110. Sharma, D.K., Patel, V. Badheka, V., Mehta, K., Upadhyay, G. 2020. Different reinforcement strategies of hybrid surface composite AA6061/(B4C+MoS2) produced by friction stir processing. *Materialwiss.Werkstofftech., 51:* 1493–15.

111. Zhao, H.J., Wang, B.Y., Liu, G., Yang, L., Xiao, W.C. 2015. Effect of vacuum annealing on microstructure and mechanical properties of TA15 titanium alloy sheets. *Trans. Nonferr. Met. Soc. China*, *25(6):* 1881–1888.

112. Konovalenko, I., Maruschak, P., Brezinová, J., Brezina, J. 2019. Morphological characteristics of dimples of ductile fracture of VT23M titanium alloy and identification of dimples on fractograms of different scale. *Mater.,*12(13): 2051.

113. Paidar, M., Vignesh, R.V., Khorram, A., Ojo O.O., Rasoulpouraghdam, A., Pustokhina, I. 2020. Dissimilar modified friction stir clinching of AA2024-AA6061 aluminum alloys: Effects of materials positioning. J. Mater. Res. Technol., 9(3): 6037-6047.

114. Morozova, I., Obrosov, A., Naumov, A., Królicka, A., Golubev, I., Bokov, D.O., Doynov, N., Weiß, S., Michailov, V. 2021. Impact of impulses on microstructural evolution and mechanical performance of al-mg-si alloy joined by impulse friction stir welding. *Mater., 14(2):* 347.

115. Chitturi, V., Pedapati, S.R., Awang, M. 2020. Investigation of Weld Zone and Fracture Surface of Friction Stir Lap Welded 5052 Aluminum Alloy and 304 Stainless Steel Joints. Coatings, 10(11): 1062.

116. Magrinho, J.P., Silva, M.B., Martins, P.A.F. 2023. Experimental determination of the fracture forming limits in metal forming. *Discov Mechanical Engineering 2,* 7 (2023): 1-19.